ELECTROSYNTHESIS AND CHARACTERIZATION OF MAIN GROUP AND TRANSITION METAL OXIDES

by

TU NGOC NGUYEN

B.S., University of California, Berkeley
(December 1988)

Submitted to the Department of Chemistry
in Partial Fulfillment of the Requirements
for the Degree of

DOCTOR OF PHILOSOPHY

at the

MASSACHUSETTS INSTITUTE OF TECHNOLOGY

May 1994

© Massachusetts Institute of Technology, 1994
All rights reserved

Signature of Author_____
Department of Chemistry
May 6, 1994

Certified by_____
Hans-Conrad zur Loye
Thesis Supervisor

Accepted by_____
Glenn A. Berchtold
Chairman, Departmental Committee on Graduate Students

Science
MASS. INST. TECH.
JUN 21 1994
LIBRARIES

This doctoral thesis has been examined by a Committee of the Department of Chemistry as follows:

Professor Dietmar Seyferth_____
Chairman

Professor Hans-Conrad zur Loye_____
Thesis Supervisor

Professor Alan Davison_____

ELECTROSYNTHESIS AND CHARACTERIZATION OF MAIN GROUP AND TRANSITION METAL OXIDES

by

Tu Ngoc Nguyen

Submitted to the Department of Chemistry, May 6, 1994,

in partial fulfillment of the requirements

for the Degree of Doctor of Philosophy in Chemistry

ABSTRACT

Chapter 1: General Introduction

A brief review of solid state synthetic techniques is given. The research discussed in this thesis is introduced.

Chapter 2: Electrosynthesis of Highly Oxidized Transition Metal and Main Group Oxides in Molten Hydroxides

The development of electrosynthesis in molten hydroxides of oxides containing high valent transition metals and main group metals is described. Electrosynthesis is shown to be a viable route to such materials, including, $KBiO_3$, $NaNiO_2$, Na_xCoO_2, $Sr_{1.75}CuO_{5.13}$, $NaBa_2Cu_3O_5$, Ca_4PtO_6, and Sr_3NiPtO_6. Experimental are discussed. The ionic conductivity of $KBiO_3$ was determined to be 10^{-5} S/cm at 300 °C, about 3 orders of magnitude lower than the conducitivity of the analogous $NaSbO_3 \cdot 1/6NaF$. The low conductivity of $KBiO_3$ was explained by the high size ratio of K^+ to Bi^{5+} compared to Na^+ and Sb^{5+}, the low mobility of K^+ compared to that of Na^+, and the role of the K^+ ion in stalilizing the Bi-O framework structure.

Chapter 3: Structural and Magnetic Characterization of the One-Dimensional Oxides, Sr_3MPtO_6, M = Co, Ni, Cu, Zn

The synthesis and characterization of a family of one-dimensional oxides, Sr_3MPtO_6, M = Co, Ni, Cu, Zn, is described. The structure was determined using Rietveld analysis of powder X-ray and neutron diffraction data. Sr_3MPtO_6 contains infinite chains composed of alternating, face-sharing PtO_6 octahedra and MO_6 trigonal prisms. Sr_3ZnPtO_6 is diamagnetic. Sr_3CuPtO_6 displays well-behaved linear chain Heisenberg antiferromagnetism, with $|J|/k = 26.1$ K and $g = 2.21$. Sr_3NiPtO_6, a $S = 1$ system, shows an onset of low-dimensional antiferromagnetism at ~25 K, with no long-

range ordering as determined by powder neutron diffraction. Sr_3CoPtO_6 displays unprecedented random spin paramagnetism with spin disorder along the chains. The magnetic coupling in this material is between ferromagnetically-ordered chain segments to give an averaged total singlet ground state.

Chapter 4: Structural and Magnetic Characterization of the One-Dimensional Oxides, Sr_3MIrO_6, M = Ni, Cu, Zn

A family of one-dimensional oxides, Sr_3MIrO_6, M = Ni, Cu, Zn, analogous to the platinum-containing oxides discussed in Chapter 4, has been structurally and magnetically characterized. The structure was determined using Rietveld analysis of powder X-ray and neutron diffraction data and found to be isostructural to Sr_3NiPtO_6. Sr_3ZnIrO_6, a S = 1/2 system, displays antiferromagnetic behavior that could be fitted an alternating chain model. Sr_3CuIrO_6 shows ferromagnetic behavior with a saturation magnetization of ~0.6 μ_B/mol . Finally, Sr_3NiIrO_6 exhibits complex magnetic behavior indicative of intrachain ferromagnetism and interchain antiferromagnetism to give a singlet ground state at low temperatures.

Chapter 5: Designing A One-Dimensional Random Spin System: Characterization of the Solid Solution $Sr_3CuPt_{1-x}Ir_xO_6$ ($0 \leq x \leq 1$)

The solid solution $Sr_3CuPt_{1-x}Ir_xO_6$ ($0 \leq x \leq 1$) was prepared and characterized to study random spin paramagnetism. The solid solution exhibited magnetic behavior in agreement with the theoretically predicted random spin paramagnetic behavior. One composition in particular, $Sr_3CuPt_{0.5}Ir_{0.5}O_6$, shows the expected magnetic and high temperature heat capacity characteristics of random spin paramagnetism.

Thesis Supervisor: Dr. Hans-Conrad zur Loye

Title: Paul M. Cook Career Development Professor of Chemistry

TABLE OF CONTENTS

List of Figures

Chapter 2

Chapter 3

Chapter 4

Chapter 5

List of Tables

Chapter 2

Chapter 3

Chapter 4

List of Schemes

Chapter 2

Chapter 3

Chapter 4

To my parents, for their endless love and support

Acknowledgements

Thanks to my advisor, Hanno zur Loye, for his support, enthusiasm, and motivation--especially on projects that I did not want to do. He has always allowed me great freedom and independence in pursuing science that I find interesting. Also, this thesis is much better because of his careful proofreading and suggestions.

I would not be in graduate school without the encouragement and support of Professor Angy Stacy and my undergraduate experiences in her lab. She has my sincerest thanks and respect.

Thanks to all the great minds I had the priviledge of collaborating with: Professor Patrick Lee and Dr. Manfred Sigrist for valuable and insightful discussions on magnetism, Dr. Art Ramirez for the heat capacity measurements, and Professor Michel Verdaguer and Dr. Thierry Jolicoeur for modelling some magnetic data and helpful suggestions on magnetism.

Thanks to all the people who were very generous with their time in helping me: Brendan Bellew and Christian Farrar for the EPR measurements, Pam Blakeslee for the conductivity measurements, Judy Stallick for the neutron measurements, and Ed McNiff for the high field magnetic measurements.

I can't think of a wackier or more fun group to work with. Thanks to the zur Loye group for all their help, especially Dan for time devoted to solving structures. Thanks to Mike for getting me started on the electrochemistry and XPS and for being a great friend.

I have made dear and close friends while at MIT, and I know that without their friendships I probably never would have finished graduate school. Thanks to Ted, Francis, Cindy, Jamie, Mathai, John, James, and Jennifer. You guys made it fun and bearable. Special thanks to the new element --*all* puns intended-- in my life, Demi.

Finally, and most importantly, thanks to my family: Ba, Me, Anh Cuong, and Chau. Things were always better knowing that I always have a home with unconditional love and support. This work is dedicated to you.

Chapter 1

General Introduction

Introduction

The synthesis and characterization of oxides containing highly oxidized transition metals or main group metals was the goal of this research project, which was motivated by the discovery of many novel and interesting magnetic and electronic properties exhibited by such materials. These properties include complex magnetic behavior, such as metamagnetism[1] and order-disorder phase transitions, as well as useful electronic phenomena, such as superconductivity and metal-insulator transitions.[2] In trying to make such materials, our research has focused on the development of a new synthetic approach, namely, electrosynthesis in molten hydroxides. In addition, we have initiated a study aimed at performing systematic substitution reactions in order to understand the composition-magnetic property relationship in a new one-dimensional bimetallic system, $Sr_3MM'O_6$ where M = Pt and Ir, and M' = Co, Ni, Cu, and Zn. Through detailed studies such as this, ultimately one may be able to design materials rationally with predictable magnetic properties.

The discovery by Bednorz and Muller[3] in 1986 of high temperature superconductivity in doped lanthanum cuprate, in which copper has a formal oxidation state of greater than two, has created renewed interests in solid state materials, especially oxides. Following their breakthrough, there was a surge in reports of new oxides containing high-valent copper, which were prepared in attempts to discover superconductors with even higher critical temperatures. This sudden interest in oxides not only produced superconductors with higher T_c's but it created interests in high valent transition metal and main group oxides in general. As a result, new structures were being discovered and a number of interesting properties, theretofore unknown, were observed. The discovery of novel properties is dependent on the synthesis of new materials with unprecedented structures.[4,5] To find new materials with unique structures, different synthetic techniques are necessary. However, essentially all of the aforementioned oxides were prepared by standard high temperature solid state reactions.

The solid state reaction is undoubtedly a useful route to solid state materials, however this method contains a number of intrinsic limitations. Reactions in the solid state require diffusion of ions through solid-solid interfaces to obtain the final homogeneous product. Thus, temperatures often exceeding 800 °C are required and reaction times are often on the order of days to weeks. Typically, to insure product homogeneity, it is necessary to interrupt the reaction repeatedly during heating and to grind the sample, which can often introduce impurities into the sample. Also, the high temperatures and long reaction times of solid state reactions often lead to the most thermodynamically stable materials.

To overcome the thermodynamic limitations of solid state reactions, a number of other synthetic approaches have been developed. Physical methods such as laser ablation[6-8], vacuum evaporation, and cathode sputtering[9,10] have been used successfully to prepare a host of materials otherwise unobtainable. Similar to these methods, chemical vapor deposition has also been used quite successfully to prepare unique materials.[11] The goal of these methods is to produce bulk material "layer by layer" or by starting with simple structural moieties.

Another approach to synthesizing non-thermodynamic solid state materials has been to employ chemical methods that are effective at lower temperatures, that is, less than 800 °C. One such approach is the precursor method.[12] By dissolving appropriate metal precursors at temperatures as low as room temperature, it is possible to obtain a homogeneous mixture that contains reactants intimately mixed on the molecular level. Thus, the interdiffusion distance is decreased and the subsequent decomposition and solid state reaction can occur at lower temperatures which can lead to metastable materials. Several other methods do not require a second, higher temperature step at all. Known as chimie douce, or soft chemistry, this method takes advantage of known chemistry, such as intercalation, ion exchange, redox, hydrolysis, etc., to prepare unique, crystalline materials at reaction temperatures typically lower than 100-200 °C.[13] This method and

the ones described above are effective ways of preparing metastable, polycrystalline solid state materials by lowering or virtually eliminating the diffusion barrier.

Effective methods for preparing single crystals of solid state materials are hydrothermal synthesis[12] and the flux method[14]. Hydrothermal synthesis utilizes supercritical water as the reaction solvent to crystallize a product from the dissolved reactants. The use of water as the solvent often leads to a final product that is hydrated. A flux, however, is by definition a high temperature, non-aqueous solution. Flux synthesis employs the same principle for reaction as aqueous and organic solvent crystallizations, and large single crystals can be obtained. The reactants are dissolved in the flux (typically a molten salt) and precipitation of the product is achieved by changing the solubility of the constituents in the flux. Changing the solubility can be achieved by slowly cooling the reaction mixture (1-10 °C/hr) or by heating isothermally at a high temperature to evaporate the flux, provided that it has a sufficiently high vapor pressure. Thus, the reaction driving force in flux synthesis is a temperature gradient.

Flux synthesis has several advantages over solid state reactions. The reaction mechanism is no longer based on solid-solid interdiffusion, since the reactants are dissolved ions in the flux and can diffuse and react more readily. This change decreases the need for expensive high temperature processing for extended times. Furthermore, the appropriate use of a low melting flux can result in reactions that occur in a single step at lower temperatures. Kinetic or low temperature phases may be isolated directly.[15] Impurities and inhomogeneities associated with solid state reactions due to imperfect mixings and failure of a reaction to go to completion are eliminated or at least minimized. (Inhomogeneities due to unequal precipitation rates in the precursor method are also eliminated.)

A modification of the flux method is achieved through the addition of an electrochemical potential. Electrosynthesis, or electrolysis , takes advantages of the benefits of flux synthesis but employs a different reaction driving force.[16-19] The

addition of a constant potential or constant current to the reaction mixture changes the driving force to a potential gradient. This different driving force suggests the possibility of synthesizing materials that otherwise cannot be prepared with the flux method. Besides having the advantages of using a flux, electrosynthesis also has a number of additional unique qualities. Extremely oxidizing and reducing conditions can be created in the flux, and unusual oxidation states or mixed-valency can often or frequently be achieved in electrosynthesized materials. These materials are often produced as high quality single crystals. The parameters involved in electrolysis, such as applied potential, current, and electrode material, can be accurately controlled to assist in understanding the reaction mechanism. Finally, a typical electrosynthetic reaction is experimentally simple to perform, and reaction times are short, on the order of minutes to hours. Taken as a whole, all of these factors make electrosynthesis a unique and attractive method to synthesize oxides.

This thesis presents the synthesis and characterization of oxides containing high valent transition metals and main group elements. Chapter 2 discusses the development and electrosynthesis of oxides at various temperatures in molten hydroxides. Molten KOH and NaOH were chosen because they are effective solvents in flux synthesis.[20-22] Addition of electrochemistry to these systems provided a convenient route to single crystals of known oxides, oxides previously only prepared by high temperature and high pressure methods, as well as novel oxides. One such oxide is the new one-dimensional compound, Sr_3NiPtO_6. Chapter 3 describes the structural and magnetic characterizations of a series of analogous platinum oxides, Sr_3MPtO_6 where M=Co, Ni, Cu, Zn. These materials were structurally characterized using single crystal, powder X-ray and neutron diffraction methods, and their magnetic properties were explained by theoretical models. The structural and magnetic characterizations of the analogous iridium series, Sr_3MIrO_6 where M=Ni, Cu, Zn, are discussed in Chapter 4. Finally, based on the composition-

property relationships discussed in the two previous chapters, the design of a new model magnetic material, $Sr_3CuPt_{1-x}Ir_xO_6$, is discussed in Chapter 5.

References

(1) Davidson, I. J.; Greedan, J. E.; von Sacken, U.; Michal, C. A.; McKinnon, W. R. *J. Solid State Chem.* **1993**, *105*, 410.

(2) Vassiliou, J. K.; Hornbostel, M.; Ziebarth, R.; DiSalvo, F. J. *J. Solid State Chem.* **1989**, *81*, 208.

(3) Bednorz, J. G.; Muller, K. A. *Z. Phys. B* **1986**, *64*, 189.

(4) Rao, C. N. R.; Nagarajan, R.; Vijayaraghavan, R. *Supercond. Sci. Technol.* **1993**, *6*, 1.

(5) DiSalvo, F. J. *Science* **1990**, *247*, 649.

(6) Song, W. D.; An, C. W.; Lu, D. S.; Fan, Y. C.; Li, Z. G. *Appl. Phys. Lett.* **1993**, *63*, 3370.

(7) Niu, C.; Lieber, C. M. *Appl. Phys. Lett.* **1992**, *61*, 1712.

(8) Niu, C.; Lu, Y. Z.; Lieber, C. M. *Science* **1993**, *261*, 334.

(9) Sajjadi, A.; Boyd, I. W. *Appl. Phys, Lett.* **1993**, *63*, 3373.

(10) Muller, H.-U.; Muller, J.-P.; Ludwig, F.; Ehlers, G. *J. Alloys Compd.* **1993**, *195*, 267.

(11) MacInnes, A. N.; Power, M. B.; Barron, A. R. *Chem. Mater.* **1992**, *4*, 11.

(12) West, A. R. *Solid state chemistry and its applications*; John Wiley & Sons Ltd.: New York, 1984.

(13) Figlarz, M. *Chem. Scr.* **1988**, *28*, 3.

(14) *High-Temperature Solution Growth*; Elwell, D., Ed.; Pergamon Press: New York, 1980; Vol. Chapter 12, pp 463-483.

(15) Marquez, L. N.; Keller, S. W.; Stacy, A. M.; Fendorf, M.; Gronsky, R. *Chem. Mater.* **1993**, *5*, 761.

(16) Wold, A.; Bellavance, D. In *Preparative Methods in Solid State Chemistry*; P. Hagenmuller, Ed.; Academic Press: New York, 1972; pp 279.

(17) Kunnmann, W. In *Preparation and Properties of Solid State Materials*; Lefever, Ed.; 1971; pp 1-36.

(18) Feigelson, R. S. In *Solid State Chemisty: A Contemporary Overview*; S. L. Holt, J. B. Milstein and M. Robbins, Ed.; American Chemical Society: 1980; pp 243.

(19) Elwell, D. In *1976 Crystal Growth and Materials*; E. Kaldis and H. J. Scheel, Ed.; North-Holland Publishing Company: 1977; pp 606-637.

(20) Carlson, V. A.; Stacy, A. M. *J. Solid State Chem.* **1992**, *96*, 332.

(21) Ham, W. K.; Holland, G. F.; Stacy, A. M. *J. Am. Chem. Soc.* **1988**, *110*, 5214.

(22) Lee, J.; Holland, G. F. *J. Solid State Chem.* **1991**, *93*, 267.

Chapter 2

Electrosynthesis of Highly Oxidized Transition Metal and Main Group Oxides in Molten Hydroxides

Chapter 2

The electrosynthesis of high valent transition metal and main group oxides in molten hydroxides is discussed in this chapter. Oxides containing metals in high oxidation states have received much attention since the discovery of high temperature superconductivity by Bednorz and Muller. Their first system to exhibit superconductivity was La-Ba-Cu-O where the copper had a formal oxidation state greater than two. Since then, other high valent cuprates,[1] as well as oxides containing high valent main group metals, such as Bi and Pb, have been shown to superconduct.[2,3]

The interest in these classes of materials has not only lead to the preparation of a host of new superconductors, but it has also lead to the discovery of many non-superconducting materials with unusual properties. For example, Li_xNiO_2 has been shown to be a metamagnet, that is, it exhibits both ferromagnetic and antiferromagnetic character.[4] $Al_6Ba_{46}Cu_{24}O_{84}$, where copper is formally 2.73+, contains unprecedented clusters of copper oxide "bowls".[5] Barium bismuth oxide has been shown to undergo a number of structural transitions.[6] These are just a few examples that demonstrate the diversity in structures and properties existing in high valent oxides. Clearly, this class of materials deserves further study.

The synthesis of highly oxidized materials has mostly been accomplished through the use of solid state reactions. Stabilization of high valences has been achieved by a second annealing step under oxygen at lower temperatures (300-600 °C) or by using high oxygen pressure. Milder chemical methods can be used as well, such as oxygen intercalation using electrochemistry,[7,8] or *in situ* oxidation using agents such as peroxides or $KClO_4$. Another strategy takes advantage of the inductive effect to stabilize high oxidation states. Referring to the bonding scheme shown below where an element **A** is bonded to a metal **M** which is bonded to an oxygen:

A+--------M-----O

Scheme 2.1

If **A** is an electropositive ion, such as an alkali, an alkaline earth or a lanthanide, then it will be ionized in the lattice and donate electrons to **M**. This electron donation will increase the covalency of the **M-O** bond and stabilize a higher oxidation state of **M**. For example, it is possible to stabilize Fe(IV) or Co(IV) by applying the inductive effect with alkaline earth elements.[9,10]

Recently, hydroxides of sodium, potassium, and barium have been used as fluxes to synthesize high valent cuprates, nickelates and bismuthates.[5,11,12] The advantages of flux synthesis have been described in Chapter 1. Specifically, flux synthesis using molten hydroxides offers a number of unique advantages over other fluxes described earlier. These fluxes are highly corrosive; they can dissolve all the late first row transition metals starting with manganese, the alkaline earth oxides, many of the lanthanides, and several main group oxides, such as bismuth oxide and Group 13 oxides. Molten hydroxide is a Lux-Flood acid-base solvent system. The hydroxide anion is in equilibrium with its conjugate acid, H_2O, and its conjugate base, O^{2-}. The acidity of the flux can be controlled by adjusting the water content of the molten mixture; acidic conditions are achieved with high water content (H_2O-rich or low pH_2O) and basic conditions are O^{2-} -rich with low water content. It is not surprising that these fluxes have high oxygen activity; both peroxide and superoxide species have been detected in molten mixtures, and in the case where copper is present, trivalent copper ions can exist in solution.[13-15] Reagent grade NaOH and KOH typically contain 0.010 and 0.145 g of water per gram of salt, respectively.[16] These "wet" salts can melt as low as ~150 °C and can remain molten indefinitely provided they remain hydrated. In the dehydrated form, these melts can remain liquid at ~500-750 °C for several days without appreciable loss of material due to evaporation. Consequently, it is possible to use molten hydroxides effectively as solvents over a large temperature range, 150-750 °C. Finally, alkaline hydroxides are inexpensive and essentially nontoxic (although they are highly corrosive), making them even more attractive as melts.

Most of the synthetic work involving molten hydroxides as solvents has relied only on the flux method. Simple oxide reactants are dissolved in the hydroxide melt followed by precipitation of the product through slow cooling the reaction mixture, which changes the solubility of the solute. The driving force for reaction is a temperature gradient. A modification of the synthesis involving hydroxides melts is the addition of an electrochemical potential. Such reactions are performed isothermally and the active driving force is now the applied potential gradient.

Electrosynthesis is a well-known route to the preparation of solid state materials, as well as molecular species. Solid state electrosynthesis was first discovered in 1807 by Davy when he deposited potassium metal from a potassium solution. Modern solid state electrosynthesis, however, has only concentrated on two areas: reduced early transition metal oxides and simple refractories containing mostly early transition metals. Furthermore, much of this work was carried out at temperatures greater than 800 °C. The high temperatures were necessary because often the solvents used had high melting points or proved to be too viscous at lower temperatures. This research has been summarized in several thorough review papers. [17-20] Briefly, it is possible to prepare reduced oxides such as molybdenum bronzes, tungsten bronzes, or vanadium spinels by dissolving the corresponding oxides in fused salts such as borates and halides. The products are slightly reduced and electrically conducting. Fully-oxidized early transition metal oxides would be insulating since they do not contain electrons in the valence shells and would passivate the electrodes, thereby preventing further crystal growth. This requirement, that the product must be electrically conducting, is perhaps the greatest limitation of electrosynthesis. However, in some cases, electrolysis is the only method capable of synthesizing a specific material, e.g., $CaTi_2O_4$.[21]

Electrolysis can also be used to synthesize a host of simple and useful refractories both at high and at low temperatures. At high temperatures, the melt is often the same as that used in transition metal oxide synthesis, namely, borates and halides. To synthesize

borides, carbides, silicides, phosphides, arsenides, or sulfides, a borate, carbonate, silicate, phosphate, arsenate or sulfate, respectively, would be added to the reaction mixture. For example, the electron emitting material, LaB_6, can be prepared in single crystal form at 900 °C by electrolyzing a mixture of La_2O_3, B_2O_3, Li_2O, and LiF.[22] Li_2O and LiF are added to form a lower melting solvent and to help dissolve the oxides, respectively. At temperatures as low as 100-150 °C, thin films of semiconducting sulfides such as PbS and CdS can be prepared by electrolyzing a DMF or DMSO solution containing dissolved metal halide and sulfur.[23-25] The products, however, tend to be amorphous to very slightly crystalline. Thus, the main focus of electrosynthesis has been on cathodic reactions and the preparation of reduced materials.

Recently, electrosynthesis in molten hydroxides has been shown to be a viable method to synthesizing highly oxidized oxides. Norton was able to synthesize single crystals of the superconductor $(Ba,K)BiO_3$ at temperatures as low as 180 °C in molten KOH.[26] Electrochemical synthesis of oxides in molten hydroxides offer a number of advantages over flux synthesis in molten hydroxides. It is known that hydroxides can support metals and oxygen in various oxidation states so that the hydroxides' electrochemical-potential windows are large.[13] Thus, by applying an electrical potential it should be possible to stabilize oxidation states that otherwise would not be possible with the oxidizing power of the hydroxide melt alone. Electrosynthesis also contains experimental parameters that can be more accurately controlled than the temperature gradient in flux synthesis. Operating *isothermally*, one can very accurately and precisely change the applied voltage or current, the electrode material, e.g., whether to use wire or foil, and the applied signal, e.g., square wave or pulsed signals. Electrosynthesis also frequently leads to the formation of single crystals in shorter time, and sometimes of better quality, than flux synthesis. Crystals suitable for X-ray analysis can be obtained in as short as 30 minutes with electrosynthesis. In summary, electrochemical synthesis of

oxides in molten hydroxides not only has the benefits of flux synthesis but also offers in its own intrinsic advantages.

This chapter discusses the development of the electrosynthesis of high valent oxides in molten hydroxides. The syntheses of a number of highly oxidized late transition metal oxides are described. $KBiO_3$, a potassium ion conductor containing pentavalent bismuth, is characterized in detail. Finally, some observations and trends observed in these systems are discussed.

General Methods:

All manipulations and experiments were performed in air unless otherwise noted. Materials were used as bought: NaOH (Mallinckrodt, Reagent grade), KOH (Mallinckrodt, Reagent grade), Cs_2O (Aesar, 99%), $Ca(OH)_2$ (Fisher, Reagent grade), $SrCO_3$ (Cerac, 99.5%), $Ba(OH)_2$, anhydrous (Fisher, Reagent grade), La_2O_3 (Aesar, Reagent grade), Y_2O_3 (Aesar, 99.99%), V_2O_5 (Aesar, 99.9%), Co_3O_4 (Aesar, 99.5%), NiO (Johnson Matthey, Reagent grade), $CuCl{\cdot}xH_2O$ (Cerac, 99%), CuO (Aldrich, Reagent), $ZnCl_2$ (Cerac, 99.5%), and Bi_2O_3 (Cerac, 99.9%). Electrodes used were Pt wire (0.5 mm diameter), Zr wire (Aesar, 1.14 mm diameter, 99.2%), and Ni wire (Aesar, 1mm diameter, 99.8%).

Current versus potential scans were achieved using a Pine bipotentiostat (Model AFRDE4) equipped with a Houston Instrument 2000 XY recorder. Voltage was swept at a rate of 100-150 mV/s. For two-electrode experiments, the cathode served as both the counter electrode and the reference electrode. Electrolysis experiments were performed using the same instrument or an ECO Instrument potentiostat (Model 549). Single crystals were characterized by X-ray precession methods using a Charles Supper camera mounted on an Enraf-Nonius Diffractis 581 X-ray generator. Polycrystalline materials were identified using powder X-ray diffraction on a Rigaku RU300 diffractometer with

CuK_α radiation. Elemental compositions were determined by wavelength dispersive spectroscopy on a JEOL 733 microprobe with internal standards.

Synthesis of $KBiO_3$:[27]

Single crystals of $KBiO_3$ were grown electrochemically from a KOH flux in an alumina crucible. The reaction mixture consisted of 1 g Bi_2O_3, 2.5 g $ZnCl_2$, and 20 g KOH. The filled crucible was placed into a closed Pyrex reaction vessel equipped with flowing, water-saturated air to prevent dehydration of the flux. The atmosphere was maintained by flowing air through a gas dispersion tube immersed in room temperature water. The reaction mixture was heated at 175°C for 2 hours, allowing the molten solution to equilibrate, before a potential was applied.

Synthesis was performed by two-electrode constant-potential electrolysis. Zirconium wire was used as the cathode and platinum wire or foil as the anode. The working potential for this reaction, 1.1V, was determined to be the point at which the current increased sharply with changing potential on an i vs. V scan. (Figure 2.1) After electrolyzing overnight, the electrodes were removed and washed with water to remove any residual flux. $KBiO_3$ was deposited as red, well-faceted chunky crystals on the platinum anode and zinc metal was deposited on the zirconium cathode. Larger crystals can be grown by electrolyzing for up to 5 days.

$KBiO_3$ can be synthesized using $CuCl{\cdot}xH_2O$ as well as $ZnCl_2$. In this case, the working potential is 0.8 V and copper metal is deposited on the cathode. Attempts to make $KBiO_3$ using only KOH and Bi_2O_3 proved unsuccessful, as did attempts to make the sodium and sodium/potassium analogs of $KBiO_3$ using NaOH and the NaOH/KOH eutectic, respectively. The role of the metal deposited on the cathode is that of a sacrificial reductant, which balances the electron inventory of the redox processes. Ion exchange experiments using molten $NaNO_3$ and $AgNO_3$ to make $NaBiO_3$ and $AgBiO_3$, respectively, from $KBiO_3$, were also unsuccessful.

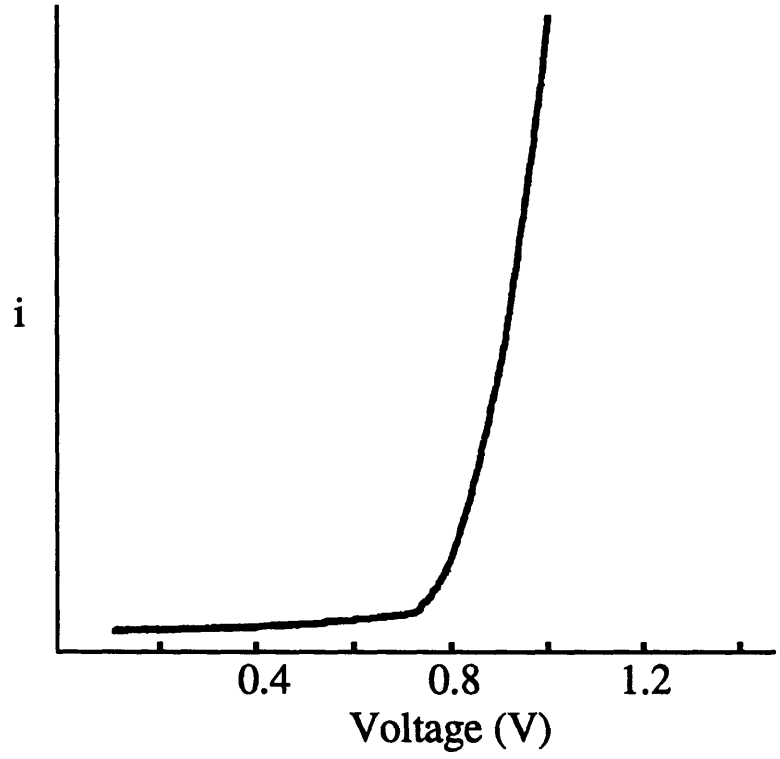

Figure 2.1. i-V scan for a solution of $CuCl_2 \cdot xH_2O$ and Bi_2O_3 in KOH at 175 °C. The electrodes were platinum wire.

The diffraction patterns of the precession photos were consistent with a body-centered cubic structure. Energy Dispersive Spectroscopy (EDS) confirmed the presence of potassium and bismuth. Wavelength Dispersive Spectroscopy (WDS) performed on 20 representative crystals gave an average crystal composition of $K_{0.98}Bi_{1.00}O_{2.99}$; the oxygen stoichiometry was determined by difference and thermogravimetric analysis. Copper and zinc impurities were not detected.

Synthesis of $NaNiO_2$:

Large (up to 3 mm), thick and black crystals of $NaNiO_2$ can be synthesized in a variety of mixtures. The best preparation was achieved using 30 g NaOH, 1 g $Ba(OH)_2$, and 0.25 g NiO. The mixture was heated to 650-700 °C and allowed to equilibriate for several hours. Nickel and zirconium wires were used as the anode and cathode, respectively. Constant potential electrolysis at approximately 1.2 V overnight yielded on the nickel wire single crystals of $NaNiO_2$ as identified by powder X-ray diffraction (JCPDS card #6-631). $NaNiO_2$ can also be prepared by replacing $Ba(OH)_2$ with Cs_2O, $SrCO_3$, Y_2O_3, or La_2O_3.

Synthesis of Na_xCoO_2:

Na_xCoO_2 can be prepared similarly to $NaNiO_2$. Approximately 32 g of NaOH, 0.6 g of $SrCO_3$, and 0.3 g of Co_3O_4 was loaded into an alumina crucible. $SrCO_3$ can be replaced by Bi_2O_3, V_2O_5 or $Ba(OH)_2$. The reaction mixture was heated to 650-700 °C and allowed to equilibriate for several hours. Nickel and zirconium wires were used as the anode and cathode, respectively. Constant potential electrolysis at approximately 1.2 V overnight yielded single crystals of Na_xCoO_2 on the nickel wire. The composition was determined by microprobe analysis, and powder X-ray diffraction identified the phase as α-$Na_{0.75}CoO_2$ (JCPDS card #32-1068).

Synthesis of $Sr_{1.75}Cu_3O_{5.13}$:

The reaction mixture consisted of approximately 13.5 g of NaOH, 19 g of KOH, 1 g of Bi_2O_3, 0.7 g of $SrCO_3$ and 0.3 of CuO. This mixture was filled into an alumina crucible, heated to 650 °C, and allowed to equilibriate for several hours. Nickel and zirconium wires were used as the anode and cathode, respectively. Electrolysis was performed using a constant potential of 1.5 V for approximately 12 hours or using a constant current of 50 mA with 25 mm of the electrodes inserted into the flux for as little as 30 minutes. The product grew on the Ni anode as black shiny needles. They were identified by powder X-ray diffraction as $Sr_{1.75}Cu_3O_{5.13}$ (JCPDS card #39-489).

Synthesis of $NaBa_2Cu_3O_5$:

The reaction mixture was similar to that used for the synthesis of $Sr_{1.75}Cu_3O_{5.13}$: 13.5 g of NaOH, 19 g of KOH, 0.7 g of Bi_2O_3, 1 g of $Ba(OH)_2$ and 0.25 g of CuO. The mixture was filled into an alumina crucible, heated to 650 °C, and allowed to equilibriate for several hours. Nickel and zirconium wires were used as the anode and cathode, respectively. Electrolysis was performed using a constant current of 50 mA for 3 days with approximately 25 mm of the electrodes inserted into the flux. The crystals grew as black chunks. Microprobe analysis and lattice parameters obtained from precession photographs matched those of $NaBa_2Cu_3O_5$, which was first synthesized by Tams.[28]

Synthesis of Sr_3NiPtO_6:

Sr_3NiPtO_6 was synthesized by constant potential, two-electrode electrolysis in molten KOH. A typical reaction mixture consisted of 0.7 g of $SrCO_3$ (Cerac, 99.5%), 0.25 g of NiO (Johnson Matthey, Reagent grade), and 32 g of KOH (Mallinckrodt, Reagent grade). This mixture was filled into an alumina crucible and heated quickly to 700 °C. The reaction mixture was allowed to equilibrate at 700 °C for four hours. After

4 hours, two platinum electrodes (0.020" diameter) were inserted into the melt and a constant potential of 0.65-0.7 V was applied. Control experiments in which no potential was applied did not yield any material. Slow cooling a mixture of $SrCO_3$, NiO, and Pt metal dissolved in molten KOH resulted in the crystallization of the known oxide, $Sr_5Ni_4O_{11}$.[12]

Electrolysis for approximately 12 hours yielded single crystals of Sr_3NiPtO_6 on the platinum anode, while the platinum cathode was almost completely consumed. The crystals of Sr_3NiPtO_6 grew as dark brown to black hexagonal prisms as big as 0.2 x 1 mm. They were easily extracted with a probe and any residual flux was removed by washing with methanol. Switching electrodes to both palladium or nickel electrodes to make the nickel-palladium or the all nickel analog, respectively, did not yield the desired products. The use of two palladium electrodes only resulted in the formation of NiO single crystals.

Synthesis of Ca_4PtO_6:

Ca_4PtO_6 was prepared similarly to Sr_3NiPtO_6 with $SrCO_3$ replaced by $Ca(OH)_2$. Approximately 0.25 g of NiO, 0.25 g $Ca(OH)_2$, and 32 g of KOH were placed into an alumina crucible. The entire mixture was heated to 700 °C and allowed to equilibriate for several hours. Electrolysis was performed with two platinum electrodes and a constant potential of 0.7 volts. After twelve hours, flat, metallic, hexagonal plates/foil was deposited on the platinum anode. Since the foil tended to shear irregularly, a quantitative elemental analysis could not be determined by microprobe; however, only calcium, platinum, and oxygen were detected. The material was not of adequate quality for single crystal characterization, and the product was identified using powder X-ray diffraction. The material's X-ray pattern matched that of JCPDS card #23-0862, Ca_4PtO_6.

Characterization of $KBiO_3$:

Physical Characterization:

The potassium ion conductivity was determined by complex impedance spectroscopy using a Solartron 1260 frequency response analyzer. Crystals were crushed in an agate mortar and pelletized. Two stainless steel plungers (1.6 mm diameter), acting as blocking electrodes, compressed the sample inside an alumina tube. The stainless steel plungers were sandwiched by two platinum disks, which in turn were held in place by a spring-loaded alumina tube. The entire sample holder was contained inside a shielded nickel tube located inside a non-inductively wound furnace. The furnace temperature was regulated using a programmable Eurotherm controller. Impedance measurements were performed at frequencies between 1 Hz and 5 MHz and temperatures ranging from 250-375°C.

Thermogravimetric analysis was carried out using a CAHN-121 TGA system. Samples were heated at a rate of 5°C/min in pure oxygen and 5% H_2/95% N_2. Polycrystalline samples were structurally characterized by powder X-ray diffraction on a Rigaku RU300 at 10 kW with Cu K_α radiation (λ = 1.5418Å).

Crystallographic studies:

A small, red, prismatic crystal of $KBiO_3$ with the approximate dimensions of 0.060 x 0.040 x 0.050 mm was used for the structure determination. Single-crystal diffraction studies of $KBiO_3$ were performed on an Enraf-Nonius CAD-4 diffractometer with graphite monochromated Mo K_α radiation (λ = 0.71069 Å). Unit cell parameters were established by least-squares analysis of 25 reflections in the range $13.0 \leq 2\theta \leq 26.0°$, a = 10.0194(6)Å, V = 1005.8(2) $Å^3$; the space group was determined to be $Im\bar{3}$ (#204). Crystallographic data are summarized in Table 2.1. Data were collected using the ω-scan method to a maximum 2θ of 60.0°. A total of 1712 reflections were collected. The intensities of three representative reflections, measured after every 60 minutes of X-ray exposure time, remained constant throughout data collection indicating crystal and

electronic stability. Data were corrected for Lorentz and polarization effects and secondary extinction. Initially, data were corrected for absorption based on the azimuthal scans; an empirical correction was also applied.[29]

All calculations were carried out on a MicroVAX 3500 with the use of TEXSAN crystallographic software.[30] The position of the bismuth and potassium, K(1), were determined by direct methods, SHELXS.[31] The remaining potassium and oxygen positions were located from Fourier maps. Refinement was performed using a full-matrix least-squares calculation. The final values of the discrepancy factors were R = 0.024 ($R = \Sigma ||F_o| - |F_c|| / \Sigma |F_o|$) and $R_w = 0.029$ ($R_w = [(\Sigma w (|F_o| - |F_c|)^2 / \Sigma w F_o^2)]^{1/2}$), where $w = 4F_o^2/\sigma^2(F_o^2)$. The goodness of fit was 1.10 and the highest peak in the final difference Fourier map was 1.79 e/Å^3. The atomic scattering factors were those of Cromer and Waber[32,33] and corrections for anomalous dispersion were from Cromer.

Results and Discussion:

The final atomic positions, thermal parameters, and occupancies are listed in Table 2.2. Anisotropic *U* values are listed in Table 2.3 and selected interatomic bond distances are shown in Table 2.4. The $KBiO_3$ structure, isostructural with that of $KSbO_3$,[34] contains pairs of BiO_6 octahedra that are edge shared to form Bi_2O_{10} clusters. These clusters share corners to form the tunnel structure shown in Figure 2.2. The potassium atoms are located in three partially occupied crystallographic sites, two along the tunnels and one at the origin. Although Goodenough[35] does not report the presence of alkali ions at the origin position of $KSbO_3$, our refinements show that electron density is clearly present at the origin. Furthermore, this electron density at the origin refined well as a potassium atom. One might consider refining the electron density at the origin as a water of hydration; however, this does not agree with the stoichiometry obtained from microprobe and thermogravimetric measurements, which gave no indication of any waters of hydration. The bismuth atom is coordinated by a slightly distorted octahedron of oxygen atoms with Bi-O bond lengths of 2.06Å, 2.11Å and 2.13Å. These distances

Table 2.1. Crystallographic Data for $KBiO_3$ at 23 °C

chemical formula	$KBiO_3$
formula weight, g/mol	296.08
crystal color, habit	red, prismatic
crystal dimension, mm	0.06 x 0.04 x 0.05
crystal system	cubic
space group	$Im\bar{3}$, (No. 204)
lattice parameters, Å	a = 10.0194(6)
volume, $Å^3$	1005.8(2)
Z	12
D_{calc}, g/cm^3	5.865
radiation, Å	$\lambda = 0.7107$
μ (Mo, Kα), cm^{-1}	534.8
secondary extinction	1.41×10^{-7}
octants	+h+k+l
R^*	0.023
R_w^{**}	0.021
GOF	1.10

* $R = \Sigma ||F_o| - |F_c|| / \Sigma |F_o|$.

** $R_w = [\Sigma w(|F_o| - |F_c|)^2 / \Sigma w F_o^2]^{1/2}$.

$w = 4F_o^2/\sigma^2(F_o^2)$.

Table 2.2. Final Positional Parameters and Their Estimated Standard Deviations

atom	Wyckoff	x	y	z	B(eq)	% site occupation	% total K
Bi1	12e	1/2	0	0.16004(6)	0.10(3)	100	
K1	16f	0.1571(5)	0.1571	0.1571	2.202(2)	60(1)	80(2)
K2	8c	1/4	1/4	1/4	2.258(7)	22(1)	14.4(8)
K3	2a	0	0	0	2.223(8)	34(2)	5.6(4)
O1	24g	0.3387(8)	0	0.2874(9)	0.7(2)	100	
O2	12d	0.363(1)	0	0	0.6(2)	100	

Table 2.3. Anisotropic U_{ij} Coefficients for $KBiO_3$

atom	Wyckoff	$u_{11}(U)$[a]	u_{22}	u_{33}	u_{12}[b]	u_{13}	u_{23}
Bi	12e	0.0031(3)	0.0019(3)	0.0007(3)	0	0	0
K(1)	16f	0.02601(2)	0.02601	0.0261	0.008(2)	0.008	0.008
K(2)	8c	0.0270(1)	0.0270	0.0270	0.033(9)	0.033	0.033
K(3)	2a	0.0270(1)					
O(1)	12d	0.012(4)					
O(2)	24g	0.004(6)					

[a] $u_{11} = u_{22} = u_{33}$ for postitions (f) and (c). [b] $u_{12} = u_{13} = u_{23}$ for positions (f) and (c). $u_{12} = u_{13} = u_{23}$ for position (e).

Table 2.4. Selected Bond Distances (Å) for $KBiO_3$

Bi-Bi	3.207(1)
Bi-K(1)	3.777(2)
Bi-K(2)	3.6553(3)
Bi-O(1)	2.136(9)
Bi-O(1)	2.053(9)
Bi-O(2)	2.108(7)
K(1)-O(2)	3.039(8)
K(1)-O(1)	2.735(7)
K(2)-O(1)	2.685(3)
K(1)-K(1)	3.156(9)
K(1)-K(2)	4.288(2)
K(1)-K(3)	2.733(8)
K(2)-K(3)	4.3385(3)

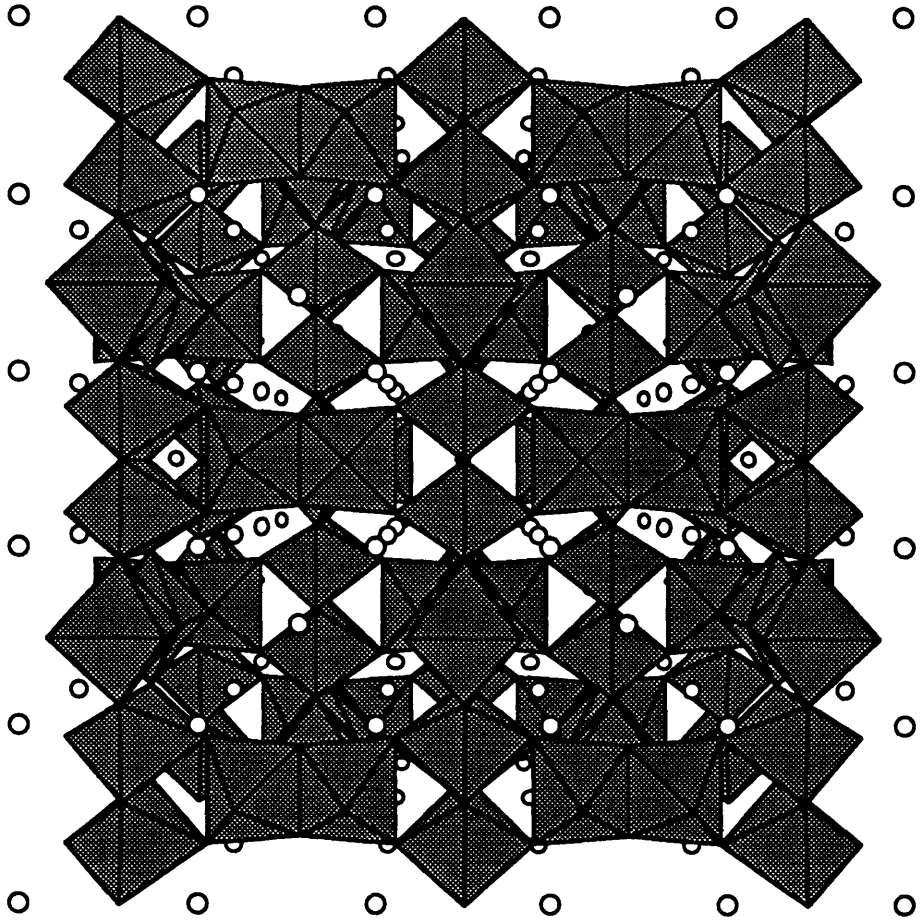

Figure 2.2. Structure of $KBiO_3$

are consistent with Bi-O bond lengths found in other bismuth (V) oxides, which range from 2.04-2.17Å.[11,36]

One might expect that a pure Bi(V) materials be colorless, rather than the reddish color that is observed. Some of the crystals prepared were opague suggesting that the material contains some Bi(IV) in addition to Bi(V). Elemental analysis by microprobe showed the sample to be stoichiometric to better than 2%. If the stoichiometry is off by 2%, either due to an excess of potassium, as in $K_{1.02}Bi(V)_{0.98}Bi(IV)_{0.02}O_3$, or due to an oxygen deficiency, as in $KBi(V)_{0.98}Bi(IV)_{0.02}O_{2.99}$, a small amount of mixed valency would result which would explain the opagueness. Goodenough observed that one of his $NaSbO_3$ samples had a 20% excess of sodium.[37] Considering that there are many more sites for the alkali metal than alkali metal content, a small excess would not create a noticeable structural effect and be difficult to detect by X-ray diffraction. Most of the crystals, however, were transparent and red. In this case, the red color has been explained by a simple band gap or a charge transfer transition, O 2p to Bi 6s.[38] The UV-Vis diffuse reflectance of $KBiO_3$ is shown in Figure 2.3. The spectrum is typical of a semiconductor with an band edge starting at approximately 14,000 cm^{-1}, or 1.74 eV.

Figure 2.4 shows the TGA data for $KBiO_3$ heated in 1 atm of O_2. The thermogravimetric data displays a sudden weight loss near 500 ° C. The total weight reduction of 5.4% corresponds to the loss of one oxygen atom from the sample and computes to an initial oxygen content of 2.99 (0.02). There is no evidence of any water of hydration, which should result in a detectable weight loss at a temperature lower than the sample decomposition temperature of 500 °C. An X-ray analysis of the residual material shows that $KBiO_3$ thermally decomposes into K_2O and Bi_2O_3. The thermal instability of this sample above 500 °C is consistent with the observation that $KBiO_3$ cannot be prepared at atmospheric pressure.[39] Only $KBiO_2$ can be prepared from K_2O and Bi_2O_3 by solid state synthesis at atmospheric pressure. High oxygen pressure stabilizes Bi(V), and consequently $KBiO_3$ can be prepared at 600 °C and several

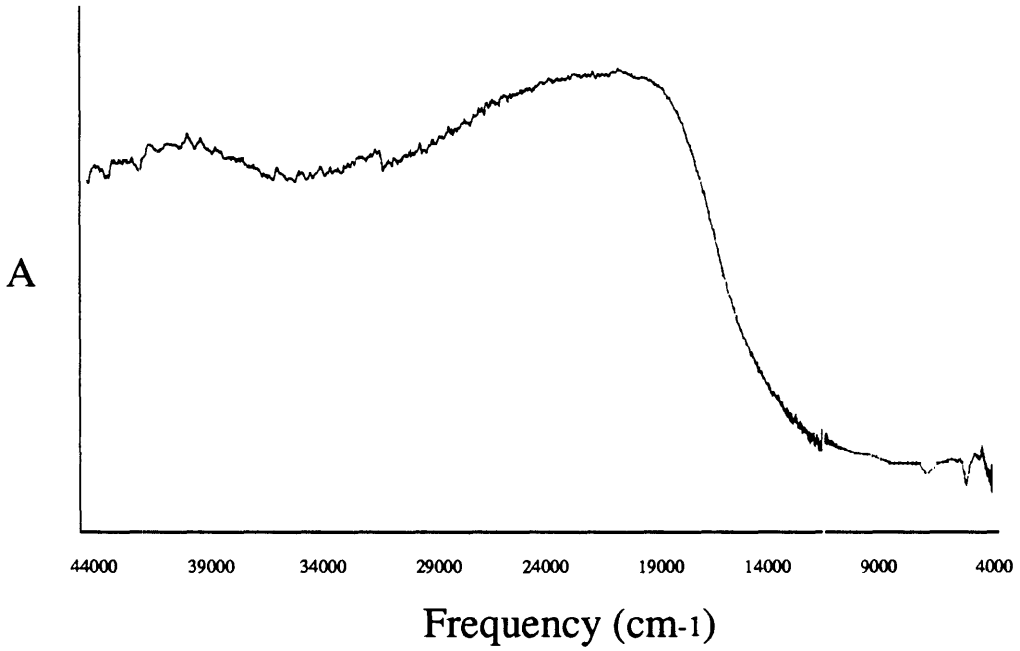

Figure 2.3. Diffuse reflectance spectrum of $KBiO_3$ showing the band edge at ~14,000 cm^{-1}.

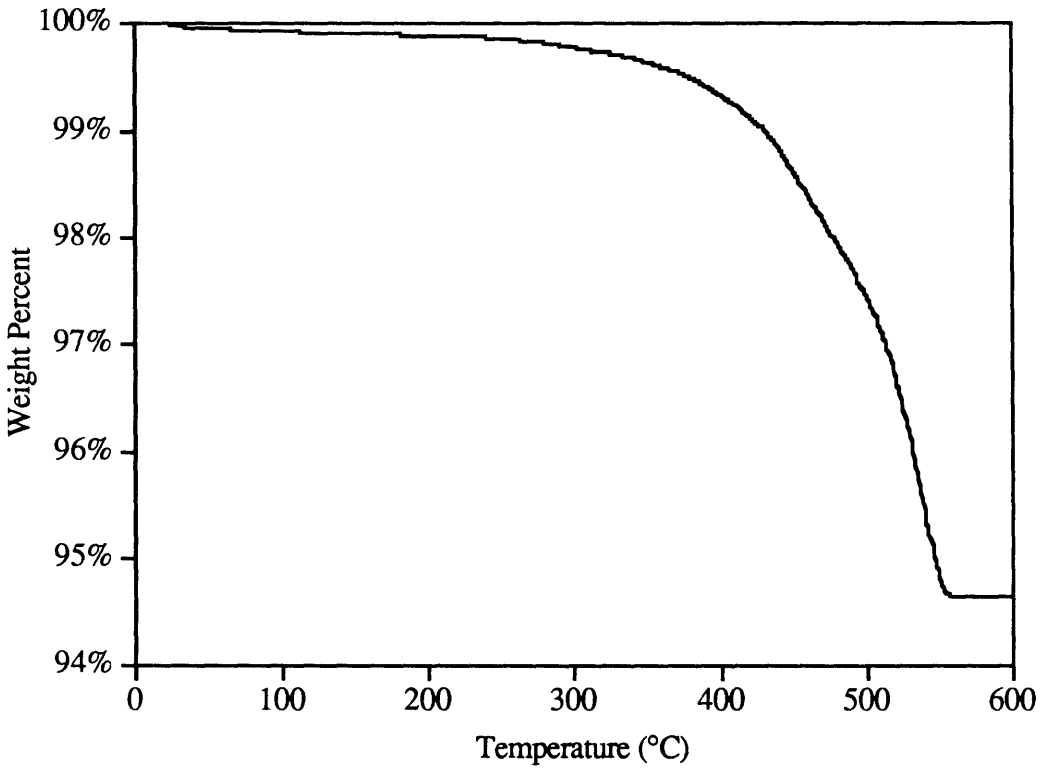

Figure 2.4. TGA of $KBiO_3$. The 5.4% weight loss at 500 °C corresponds to the loss of one oxygen atom.

thousand atmospheres of oxygen pressure. This instability also imposes an upper limit on the ionic conductivity measurements that can be carried out.

The partial occupancy of the three potassium sites suggests that this structure might exhibit good potassium ion conductivity and, consequently, also undergo alkali-metal-ion exchange. In the isostructural $KSbO_3$ material, Goodenough[37] found that it was possible to exchange the potassium for sodium to prepare $NaSbO_3$. We have attempted the ion exchange, albeit unsuccessfully. This behavior can rationalized by considering that in other tunnel structures waters of hydration are required to stabilize the framework structure when trying to exchange potassium ions with smaller alkali-metal ions.[40] Interestingly, Goodenough, who used high-pressure synthesis to prepare $KSbO_3$, was unable to prepare the $NaSbO_3$ by this method, suggesting that the sodium ions are not large enough to stabiliize the structure during synthesis. However, in the case on $KSbO_3$, ion exchange of alkali metals into the structure, once the antimony-oxygen framework has formed, was possible.

The potassium ion conductivity of $KBiO_3$ was measured as a function of temperature and is shown in Figure 2.5. The activation energy of potassium ion conduction is only 0.16 eV, which is comparable to that of sodium in β-alumina.[41] The potassium ions are located in tunnels along the [111] direction, which are made up of face-shared octahedral sites. The bottleneck for ionic conductivity is the passage through oxygen triangles which make up the octahedral faces. The oxygen triangles of the K(1) position are widened, making it easy for the potassium to hop through, while the oxygen triangles of the K(2) position are more restrictive. The conductivity of $KBiO_3$, 10^{-5} S/cm at 300 °C, is 3 orders of magnitude lower than the reported conductivity of $NaSbO_3 \cdot 1/6NaF$, 10^{-2} S/cm at 1 kHz and 300 °C.[37] A significant part of this difference may be due to the smaller size ratio of Na^+ and Sb^{5+}, compared to K^+ and Bi^{5+}, while the remainder can be explained by the lower mobility of the potassium ion compared to that of the sodium ion. The sodium ion in $NaSbO_3 \cdot 1/6NaF$ is relieved of its role of stabilizing the framework

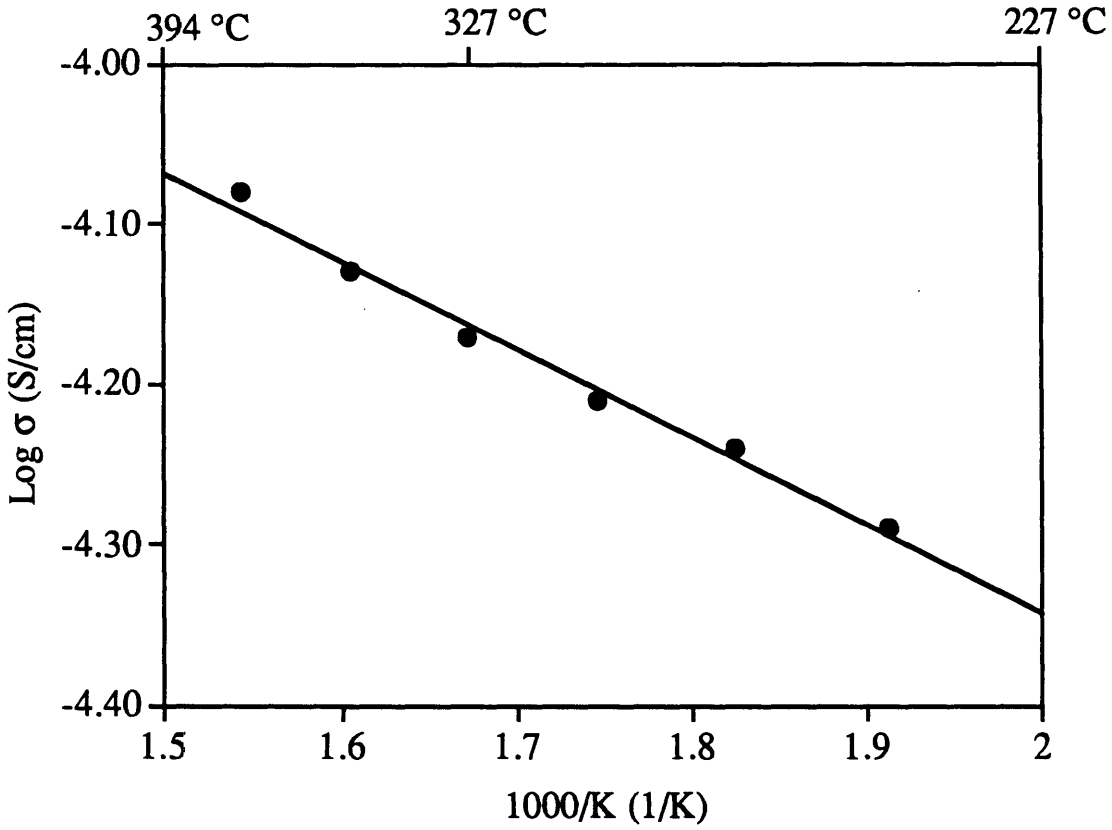

Figure 2.5. Temperature dependence of the potassium ionic conductivity of $KBiO_3$.

structure due to the presence of the additional NaF in the structure, enhancing its mobility. The potassium ion in $KBiO_3$, on the other hand, is needed to stabilize the Bi-O framework structure and, consequently, cannot be very mobile, which is consistent with the ion exchange results.

The potassium ion mobility might be enhanced if its structure-stabilizing role could be assumed by another species, such as H_2O, as is observed in the aqueous synthesis route. Water might act analogously to NaF in $NaSbO_3 \cdot 1/6NaF$, and stabilize the Bi-O framework in $KBiO_3$. Furthermore, it has been found that KF enhances the mobility of the sodium ions.[37] Introducing water or KF into $KBiO_3$, consequently, may free up the potassium ions for ion-exchange reactions with other alkali metals, as well as enhance the potassium ion mobility for improved ionic conductivity.

Results and Discussion:

Anodic electrolysis in molten hydroxides has been shown to be an effective route to high valent oxides. These materials include both late transition metal and main group oxides. Electrosynthesis in hydroxides exploits the many advantageous qualities of these salts, such as corrosiveness and high oxygen activity. However, since the reaction driving force has changed, different products are isolated than those obtained from flux synthesis in the same melt.

The addition of electrochemistry to high-temperature melts has also added several parameters and variables to the synthesis. The most significant difference is, of course, the change in reaction driving force. Experimentally, flux synthesis is simpler, requiring only a furnace that can cool the melt in a controlled manner. Electrosynthesis requires a potentiostat and design of an electrochemical cell. Most of the cells used previously in the electrosynthesis of reduced oxides and refractories have had a similar design. A vital part of the cell is a gas inlet that allows the cell to be flushed with an inert gas such as helium or argon. The flowing gas serves to eliminate the oxygen gas generated at the

anode, since oxygen can decompose the reduced product at the cathode. In our system where the desired material forms at the anode, oxygen attack is not a problem However, to keep NaOH and KOH liquid at low temperatures (150-500 °C), it is necessary to keep the atmosphere in the reaction vessel saturated with water. (Figure 2.6) At higher temperatures, the electrosynthesis experiment can be performed in air for several days without appreciable loss of flux due to evaporation. (The melting points of anhydrous KOH and NaOH are 360 °C and 318 °C, respectively.) The humid condition necessary for low-temperature synthesis is achieved by flushing the reaction cell with air that has been passed through a sparger immersed in water. The result is a wet, and consequently, basic melt. The two electrodes are simply Pt, Zr, or Ni wires clipped on miniature copper Mueller clips. These clips are mechanically crimped to copper wires that are inserted through ceramic tubing for electrical insulation before being connected to the potentiostat. Three-electrodes experiments, where one electrode served as a separate reference, were tried, but they did not give any noticeable improvements over two-electrodes experiments. The low temperature synthesis of $KBiO_3$ needed only two electrodes but required the wet atmosphere experimental setup.

The synthesis of $KBiO_3$ also demonstrates some important features of electrosynthesis in hydroxides. Anhydrous $KBiO_3$ was first prepared as a powder by Jansen at 500-600 °C and 1000-2000 atms of oxygen.[39] The high temperatures and high pressures were necessary to stabilize the high oxidation of bismuth. The fact that pentavalent bismuth can be stabilized by our electrochemical approach indicates that we can generate high oxygen activity at low temperatures and atmospheric pressure . We have not been successful in synthesizing $KBiO_3$ by the flux method suggesting the addition of an electrochemical gradient increases the oxygen activity of the flux. Also, in times as short as 1 hr, it is possible to grow single crystals suitable for X-ray analysis. The reaction can further be assisted by adding a sacrificial reductant to the solution. Adding an easily reduced sacrificial species such as $ZnCl_2$ or $CuCl_2$ can lead to reactions

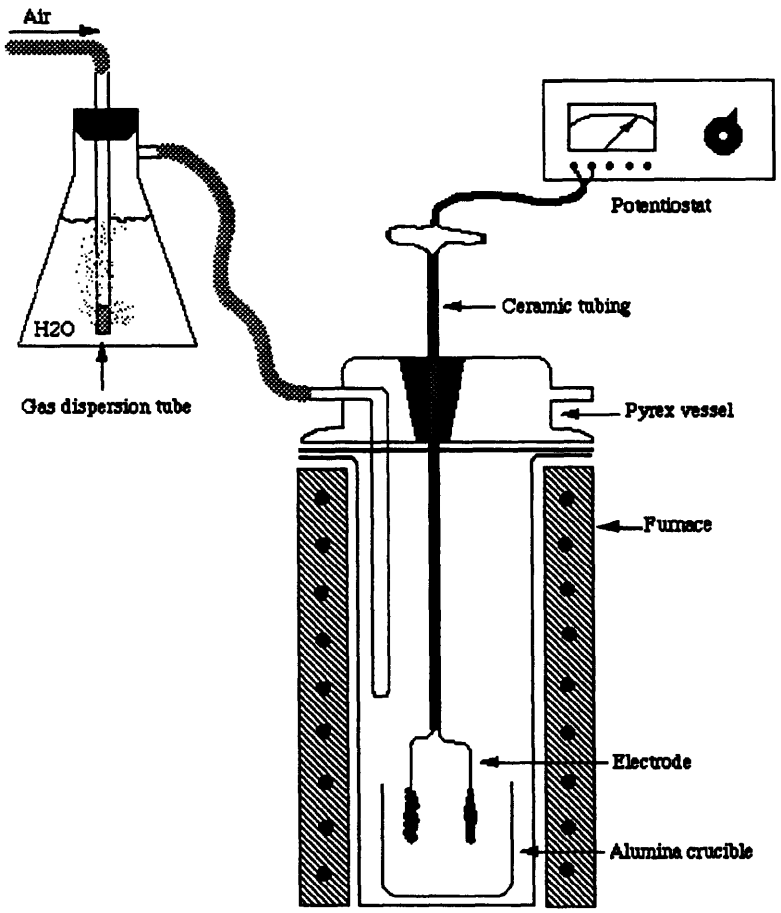

Figure 2.6. Experimental setup for low temperature electrosynthesis in molten hydroxides.

taking place at lower operating potential by providing an easy reduction reaction at the cathode. Often, adding material that is not incorporated in the final product is necessary for synthesis. In the syntheses of the cuprates, $Sr_{1.75}Cu_3O_5$ and $NaBa_2Cu_3O_6$, the presence of Bi_2O_3 is necessary. Unlike in the case of $KBiO_3$, where metallic crystals were deposited at the cathode, no bismuth or copper crystals were seen on the cathode. It is not clear what the role of the bismuth oxide is. It does seem to eliminate the reduction of copper oxide to copper metal, suggesting that perhaps bismuth metal is serving as the sacrificial reductant and is being deposited as a thin film on cathode.

The electrosynthesis of cuprates also demonstrates the importance of choosing the proper flux and experimental method. Both cuprates were prepared in the NaOH/KOH eutectic, even though potassium is not in the final products. These materials cannot be synthesized in pure NaOH or pure KOH. It appears that the solvent must contain Bi_2O_3, NaOH and KOH; otherwise, either no product can be isolated or copper metal is formed at the cathode. KOH is also known to be more oxidizing than NaOH. In cuprate and cobaltate syntheses, the binary transition metal oxides are highly soluble in both hydroxides. However, NiO is much more soluble in KOH than in NaOH. Thus, for a given system, it is important to try as many different flux combinations as possible.

Cuprate electrosynthesis is also better accomplished using constant current output than using constant voltage. For $NaBa_2Cu_3O_6$, a constant current must be applied for product formation. For $Sr_{1.75}Cu_3O_5$, using constant current greatly reduces the reaction time--from as short as 30 minutes compared to hours needed in constant potential output. In general, all of the electrosynthesis described in this thesis has had the benefit of shorter reaction times and lower synthesis temperatures compared with solid state synthesis and even flux synthesis. For example, $NaBa_2Cu_3O_6$ can be prepared from the simple oxides using solid state synthesis at 750 °C for 7 days in a silver tube. The same material can be made electrochemically at 650 °C in only 12 hours in air.

Another observed trend is the strong dependence on the electrode material. For the NaOH and the NaOH/KOH solvent systems, nickel and zirconium can serve as the anode and cathode, respectively. There is no significant corrosion of the electrodes after electrolysis. Since KOH is more oxidizing than NaOH, it eventually corrodes all the metals tried, e.g., Ni, Zr, Pd, Au, Ag, and Pt. In fact, the only materials we have been able to isolate in a pure KOH flux are those in which platinum from the electrodes was incorporated into the final product, for example, in Sr_3NiPtO_6. Experiments in which the electrodes are not inert will not give an i-V scan as in the synthesis of $KBiO_3$, but a rather erratic curve will be seen, Figure 2.7. This type of behavior has been seen in other systems where the electrodes are not inert.[18] It is interesting to note that this electrochemical route, where the electrode is consumed, is the only method we have found to make single crystals of Sr_3NiPtO_6. Experiments in which the platinum electrodes were replaced by Ni, Pd or Zr electrodes and platinum powder was added to the flux did not yield Sr_3NiPtO_6. Therefore, as with choice of hydroxides, it is important to test all possible electrode materials.

As mentioned earlier, a requirement of electrosynthesis is that the material deposited on the electrode must be conducting. However, as seen with $KBiO_3$, the material can have a significant band gap and still be sufficiently conducting to electrodeposit. Furthermore, the material can "adjust" itself to be slightly conducting. For example, stoichiometric Sr_3NiPtO_6 is predicted to be electrically insulating. The fact that we can make this material directly indicates that there is some degree of nonstoichiometry. The material can be oxygen nonstoichiometric and/or cation nonstoichiometric. This nonstoichiometry is very small, however, since we could not detect it within the sensitivity of the microprobe. This observation is consistent with the thermogravimetric analyses of the powder samples which showed that the oxygen content can vary from 5.93-6.00. Nonetheless, the material was conducting enough to deposit on the electrode.

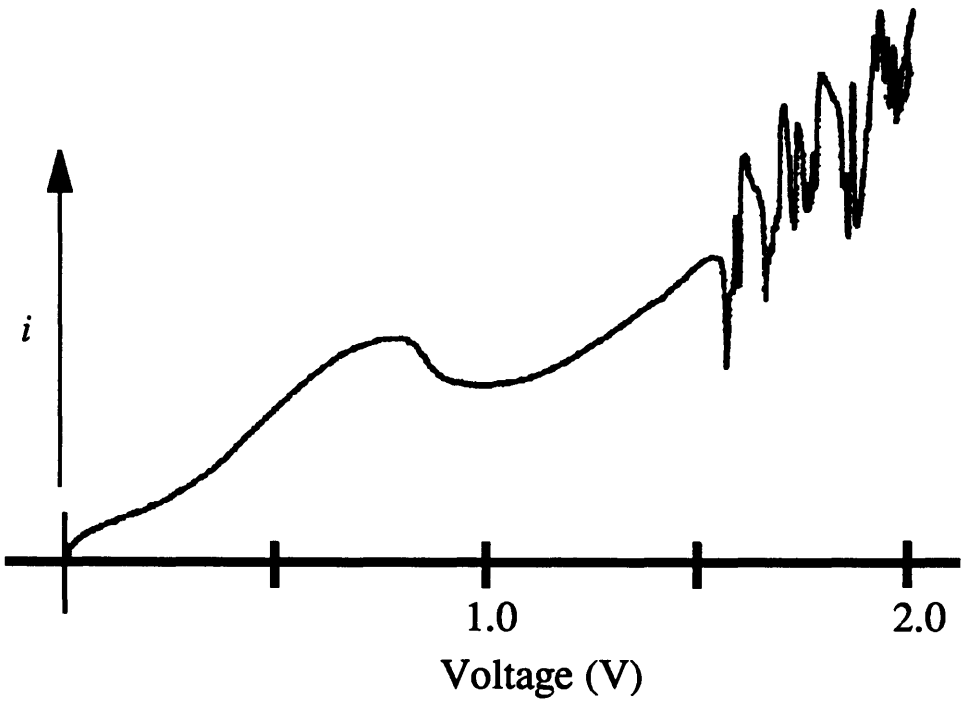

Figure 2.7. i-V scan for a mixture of $SrCO_3$ and NiO in molten KOH at 700 °C for the synthesis of Sr_3NiPtO_6. The erratic behavior is due to non-inert platinum wire electrodes.

Conclusions:

Electrosynthesis in molten hydroxides has been shown to be an effective route to high valent transition metal and main group oxides. This method exploits the advantages of hydroxide melts while employing a different reaction mechanism than the mechanism used in precipitation methods. Electrosynthesis produces materials conveniently and also yields materials that are unobtainable by other synthetic routes. Experimentally, electrosynthesis is simple, but it is vital to explore all possible parameters such as applied potential versus applied current, specific flux composition, and electrode materials. Which parameters to use for any given system is not yet predictable in advance.

References

(1) Rao, C. N. R.; Nagarajan, R.; Vijayaraghavan, R. *Supercond. Sci. Technol.* **1993**, *6*, 1.

(2) Cava, R. J.; Batlogg, B.; Krajewski, J. J.; Farrow, R.; Rupp, L. W.; White, A. E.; Short, K.; Peck, W. F.; Kometani, T. *Nature* **1988**, *332*, 814.

(3) Sleight, A. W.; Gillson, J. L.; Bierstedt, P. E. *Solid State Commun.* **1975**, *17*, 27.

(4) Davidson, I. J.; Greedan, J. E.; von Sacken, U.; Michal, C. A.; McKinnon, W. R. *J. Solid State Chem.* **1993**, *105*, 410.

(5) VerNooy, P. D.; Dixon, M. A.; Hollander, F. J.; Stacy, A. M. *Inorg. Chem.* **1990**, *29*, 2837.

(6) Reis, K. P.; Jacobson, A. J.; Kulik, J. *Chem. Mater.* **1993**, *5*, 1070.

(7) Demourgues, A.; Wattiaux, A.; Grenier, J. C.; Pouchard, M.; Soubeyroux, J. L.; Dance, J. M.; Hagenmuller, P. *J. Solid State Chem.* **1993**, *105*, 458.

(8) Grenier, J.-C.; Wattiaux, A.; Doumerc, J.-P.; Dordor, P.; Fournes, L.; Chaminade, J.-P.; Pouchard, M. *J. Solid State Chem.* **1992**, *96*, 20.

(9) Ryu, K. H.; Roh, K. S.; Lee, S. J.; Yo, C. H. *J. Solid State Chem.* **1993**, *105*, 550.

(10) Choy, J. H.; Demazeau, G.; Byeon, S. H. *Solid State Commun.* **1991**, *80*, 683.

(11) Carlson, V. A.; Stacy, A. M. *J. Solid State Chem.* **1992**, *96*, 332-343.

(12) Lee, J.; Holland, G. F. *J. Solid State Chem.* **1991**, *93*, 267.

(13) Plambeck, J. A. ; Marcel-Dekker: New York, 1976; Vol. 10, pp 283.

(14) Goret, J.; Tremillion, B. *Bull. Soc. Chim. Fr.* **1966**, 67.

(15) Elwell, A.; Tremillion, B. J. *J. Electroanal. Chem.* **1968**, *18*, 277.

(16) Claes, P.; Gilbert, J. *Molten Salt Techniques*; Plenum: New York, 1983, pp 79.

(17) Feigelson, R. S. In *Solid State Chemisty: A Contemporary Overview*; S. L. Holt, J. B. Milstein and M. Robbins, Ed.; American Chemical Society: 1980; pp 243.

(18) Elwell, D. In *1976 Crystal Growth and Materials*; E. Kaldis and H. J. Scheel, Ed.; North-Holland Publishing Company: 1977; pp 606-637.

(19) Kunnmann, W. In *Preparation and Properties of Solid State Materials*; Lefever, Ed.; 1971; pp 1-36.

(20) Wold, A.; Bellavance, D. In *Preparative Methods in Solid State Chemistry*; P. Hagenmuller, Ed.; Academic Press: New York, 1972; pp 279.

(21) Bright, N. F. H.; Rowland, J. F.; Wurm, J. G. *Can. J. Chem.* **1958**, *36*,

(22) Zubeck, I. V.; Feigelson, R. S.; Huggins, R. A.; Pettit, P. A. *J. Cryst. Growth* **1976**, *34*, 85.

(23) Baranski, A. S.; Fawcett, W. R.; McDonald, A. C. *J. Electroanal. Chem.* **1984**, *160*, 271.

(24) Baranski, A. S.; Fawcett, W. R. *J. Electrochem. Soc.* **1980**, *127*, 766.

(25) Elwell, D. *J. Cryst. Growth* **1981**, *52*, 741.

(26) Norton, M. L.; Tang, H.-Y. *Chem. Mater.* **1991**, *2*, 431.

(27) Nguyen, T. N.; Giaquinta, D. M.; Davis, W. M.; zur Loye, H.-C. *Chem. Mater.* **1993**, *5*, 1273.

(28) Tams, G.; Muller-Buschbaum, H. *Z. Anorg. Allg. Chem.* **1992**, *617*, 19.

(29) Walker, N.; Stuart, D. *Acta Crystallogr.* **1983**, *A39*, 158.

(30) Swepston, P. N. In Molecular Structure Corporation: 1985; pp .

(31) Sheldrick, G. M. In *Crystallographic Computing 3*; G. M. Sheldrick, C. Krüger and R. Goddard, Ed.; Oxford University Press: 1985; pp 175-189.

(32) Cromer, D. T.; Waber, J. T. In *International Tables for X-ray Crystallography, Table: 2.2A,* The Kynoch Press: Birmingham, England, 1974; Vol. IV.

(33) Cromer, D. T.; Waber, J. T. In *International Tables for X-ray Crystallography, Table: 2.3.1,* The Kynoch Press: Birmingham, England, 1974; Vol. IV.

(34) Spiegelberg, P. *Ark. Kem.* **1940**, *14A*, 1.

(35) Hong, H. Y.; Kafalas, J. A.; Goodenough, J. B. *J. Solid State Chem.* **1974**, *9*, 345.

(36) Hübenthal, R.; Hoppe, R. *Acta Chem. Scand.* **1991**, *45*, 805-811.

(37) Goodenough, J. B.; Hong, H. Y.-P.; Kafalas, J. A. *J. Solid State Chem.* **1976**, *9*, 203.

(38) Kodialam, S.; Korthius, V. C.; Hoffmann, R.-D.; Sleight, A. W. *Mat. Res. Bull.* **1992**, *27*, 1379.

(39) Jansen, M. *Z. Naturforsch.* **1977**, *32b*, 1340.

(40) Wang, E.; Greenblatt, M. *Chem. Mater.* **1991**, *3*, 542.

(41) Virkar, A. V.; Tennenhouse, G. J.; Gordon, R. S. *J. Am. Ceram. Soc.* **1974**, *57*, 508.

Chapter 3

Structural and Magnetic Characterization of the One-Dimensional Oxides, Sr_3MPtO_6 where M = Co, Ni, Cu, and Zn

Chapter 3

In this chapter the synthesis and characterization of a family of one-dimensional oxides, Sr_3MPtO_6 where M = Co, Ni, Cu, and Zn, is described. Sr_3NiPtO_6, the first member of this family, was prepared electrochemically in molten hydroxides, see Chapter 2. Our initial analysis revealed a one-dimensional chain structure with corresponding low-dimensional magnetic behavior. The structure was able to accommodate substitution on the trigonal prismatic M site, allowing for the systematic study of the composition-magnetic property relationship in this new one-dimensional bimetallic system.

Low-dimensional materials with extended structures have long been of interests to physicists and chemists because of their unique properties. Low-dimensional solids can be either one-dimensional or two-dimensional. One-dimensional materials are characterized by infinite chains of atoms with strong covalent/ionic or metallic bonding within the chain and weak bonding between the chains. Analogously, two-dimensional materials contain sheets or slabs of atoms or polyhedra separated by weak bonding. As a result of the strong directionality of the structures, physical properties of low-dimensional materials are also highly anisotropic. i.e., they are dependent on the crystallographic axes along which the measurements are taken.

Low-dimensional solids also tend to possess unusual properties. Transition metal di- and tri-sulfides have electrical properties ranging from insulating to metallic. NbS_2, a two-dimensional material with the TiS_2 structure, and the structurally-related Li_xNbO_2 are known to be superconducting. NbS_3 and $NbSe_3$ are one-dimensional materials which exhibit charge density waves.[1] Some materials with low dimensionality are ideal hosts for studying intercalation chemistry since they possess weak van der Waals forces. Consequently, among others, there has been much interest in low-dimensional materials as cathode materials for battery applications.

Our interest in low-dimensional materials, however, has focused on magnetic properties. Magnetic systems of low dimensionality are of particular interest not only

because of their anisotropy but also because they can exhibit novel quantum effects. For example, high temperature superconductivity in cuprates is believed to occur within the copper oxide sheets. This phenomenon is believed to be related to the observation that two-dimensional S=1/2 antiferromagnets possess large quantum fluctuations which greatly reduce their spontaneous magnetization at T=0.[2] For one-dimensional systems, Haldane has discovered the existence of an energy gap between a nonmagnetic singlet ground state and the excited states of a Heisenberg one-dimensional antiferromagnet with integer spin.[3,4] In comparison, for a non-integer spin Heisenberg antiferromagnet, one would expect a continuum of excited states from the ground state and no gap.[5] Haldane's theory has been proven experimentally[2,6,7] and is a good example of the great diversity of properties possible in low-dimensional materials.

In this chapter the synthesis and characterization of a family of one-dimensional bimetallic oxides, Sr_3MPtO_6 where M = Co, Ni, Cu, and Zn, is described. These materials were characterized structurally using X-ray and neutron powder diffraction and characterized magnetically using SQUID measurements. Sr_3NiPtO_6, the first material prepared by us, was synthesized electrochemically in molten hydroxides, see Chapter 2. The copper analog, Sr_3CuPtO_6, was first prepared by Wilkinson, et.al., during a study of the Sr-Cu-O phase diagram in platinum crucibles.[8] They reported the structure, but no other characterization was performed. The existence of these two structural analogs suggested that this structure could accommodate additional substitutions such as cobalt and zinc on the metal sites. The substitutions described in this chapter allowed us to study the composition-magnetic property relationship methodically in this one-dimensional system.

Experimental:

General Methods: All materials were used as received: $SrCO_3$ (Cerac, 99.5%), Pt metal (Aesar, 99.9%, or Engelhard), NiO (Cerac, 99.995%), CuO (Cerac, 99.999%),

Co metal (Cerac, 99.8%), and ZnO (Aldrich, 99.9%). Materials were structurally characterized by powder X-ray diffraction methods on a Rigaku RU300 diffractometer or by neutron powder diffraction collected at the NIST nuclear facility at Gaithersburg, Maryland. Single crystal analyses were initially performed on a Charles Supper Co. precession camera mounted on an Enraf-Nonius Diffractis 581 X-ray generator. Rietveld refinement of the powder diffraction data was performed using the refinement package GSAS.[9] X-ray photoelectron specta were obtained on a Surface Science Instruments Model SSX-100 spectrometer using monochromatic Al K_α radiation and operating at 10^{-8} Torr. A 1 mm spot size was used.

The oxygen content of the samples was determined by thermogravimetric analysis (TGA) using a Cahn TG121 system. Samples weighing approximately 50-100 mg were heated to 900 °C in 5% H_2/95% N_2. The initial oxygen content was back-calculated from the measured weight loss. Heating oxygen deficient samples in pure oxygen to 700 °C resulted in a weight gain associated with the complete oxidation of the compounds.

Magnetic measurements were obtained using a Quantum Design MPMS SQUID magnetometer at temperatures ranging from 2 to 300 K. All samples were fully oxidized by annealing in O_2 at 550-750 °C before being used for any magnetic measurements. For data collection, all samples were cooled in zero field to 5 K. Once the sample temperature reached 5 K, the magnetic field was turned on and data were collected. All data were corrected for the diamagnetic contribution of the calibrated Kel-F sample container. Electron paramagnetic resonance measurements were performed on powder samples at ~4 K using a Bruker EPR spectrometer.

All polycrystalline samples were prepared via solid state synthesis. Stoichiometric amounts of $SrCO_3$, Pt metal, and the appropriate first row transition metal oxide were intimately mixed under acetone using an agate mortar and pestle and pressed into pellets. The pellets were placed on platinum foil in alumina boats during heating to

prevent aluminum contamination. Heating the samples at 1150 °C for 2 weeks with intermittent grindings yielded single phase materials.

Results and Discussion:

Sr_3CuPtO_6: Sr_3CuPtO_6 was first prepared by Wilkinson, et.al. during an investigation of high-T_c cuprates.[8] They produced single crystals of Sr_3CuPtO_6 when the platinum crucible was attacked during a study of the Sr-Cu-O phase diagram. The single crystal structure could not be determined accurately due to large absorption effects. Starting with the resulting model from X-ray studies, however, they were able to determine the structure from Rietveld refinement of powder neutron data. The Sr_3CuPtO_6 structure and positional parameters are shown in Figure 3.1 and Table 3.1, respectively.

Sr_3CuPtO_6 has a one-dimensional chain structure similar to materials of the type A_4PtO_6 (A = Ba, Sr, Ca) which adopts the rhombohedral K_4CdCl_6 structure. The A_4PtO_6 structure, space group $R\bar{3}c$, consists of infinite chains of alternating face-sharing PtO_6 octahedra and AO_6 trigonal prisms.[10,11] These chains are separated by the remaining electropositive elements which maintain charge balance and are located in square antiprismatic coordination. In the case of Sr_3CuPtO_6, the strong prefence of Cu(II) to bond in square planar coordination moves the copper from the center to near a face of the trigonal prism, distorting the structure and lowering the symmetry to C2/c. The platinum still retains its octahedral coordination. No other characterization of Sr_3CuPtO_6 has been reported.

The magnetic susceptibility of Sr_3CuPtO_6, shown in Figure 3.2, displays anitferromagnetic ordering. This material has an ordering temperature of ~40 K, and the turnover in the susceptibility curve at low temperatures indicates the presence of quasi-long range order. The broadness of the magnetic transition is consistent with the low-dimensional nature of the structure, since a three-dimensional structure would be

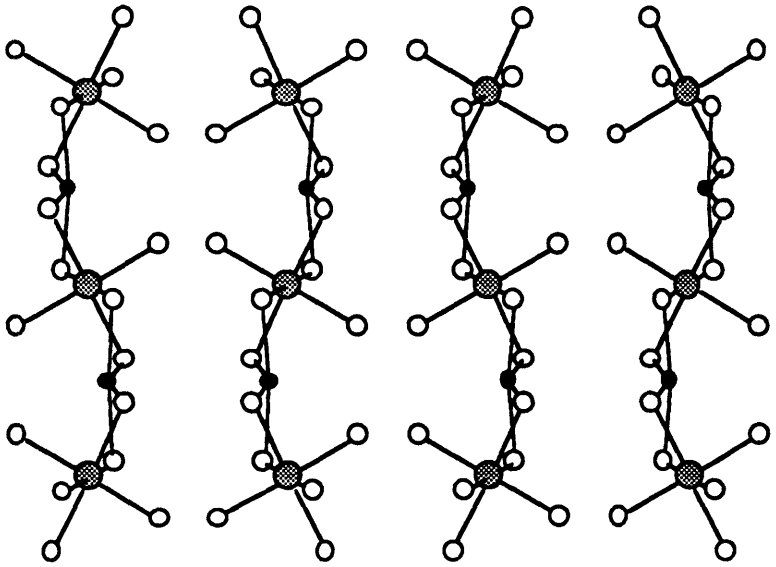

Figure 3.1. The structure of Sr_3CuPtO_6. The copper, platinum and oxygen are black, grey and white circles, respectively.

Table 3.1. Structural Parameters of Sr_3CuPtO_6,[8] C2/c (#15)

a = 9.3243(4), b = 9.7291(4), c = 6.6965(3)
β = 91.918(1)°, Z = 4

Atom	x	y	z
Pt(1)	.25	.25	0.0
Sr(1)	0.3136(2)	0.0730(2)	0.6217(3)
Sr(2)	0.0	0.1046(2)	0.25
Cu(1)	0.5	0.2020(2)	0.25
O(1)	0.2119(2)	0.3133(2)	0.7157(3)
O(2)	0.3573(2)	0.4258(2)	0.0737(3)
O(3)	0.0562(2)	0.3408(2)	0.0363(3)

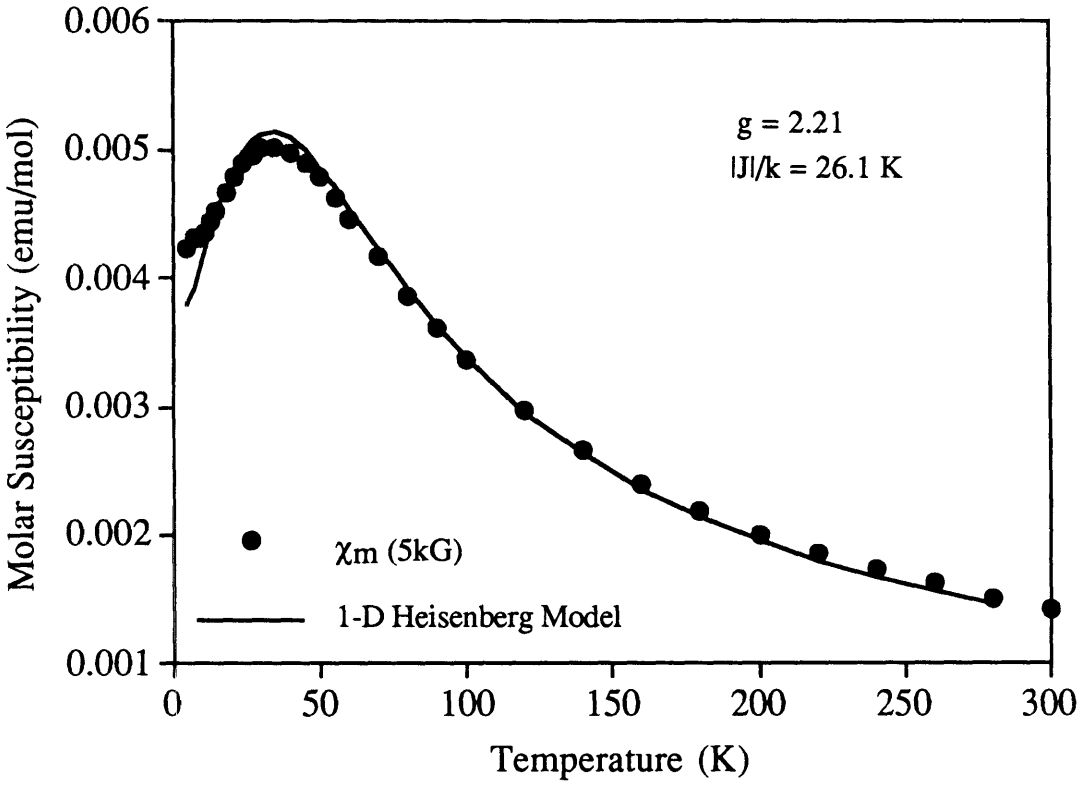

Figure 3.2. Magnetic susceptibility of Sr_3CuPtO_6 at 5 kG. The best fit to the one-dimensional S = 1/2 antiferromagnetic Heisenberg model is shown as the solid line.

expected to have a cusp-shaped transition, indicating spontaneous, long range order. A Curie-Weiss law fit of the data above 100 K gave a magnetic moment of 1.99 μ_B per mole of Sr_3CuPtO_6, typical for Cu(II) . The calculated Weiss constant is -46.6 K, indicating antiferromagnetic coupling. The magnetic moment is in reasonable agreement with the spin-only value of 1.73 μ_B expected for one unpaired electron of square planar Cu(II), d^9 and no unpaired electrons in low-spin, octahedral Pt(IV), d^6.

Since Cu(II) is typically a Heisenberg ion[12], i.e., the orbital contribution is largely quenched, the susceptibility of Sr_3CuPtO_6 was fitted to a S = 1/2 Heisenberg linear chain model.[13] The data was fitted by least-square methods using the program Igor.[14] The equation used was obtained from Hatfield:[15]

$$\chi_m = \frac{Ng^2\mu_B^2}{kT} \bullet \frac{A + BX^{-1} + CX^{-2}}{1 + DX^{-1} + EX^{-2} + FX^{-3}}$$

where X = kT/|J|, N is Avogadro's number, g is the powder-averaged g-factor, k is Boltzmann's constant, μ is the Bohr magneton, and J is the exchange constant. The coefficients used in the fit were obtained by Hatfield: A = 0.25, B = 0.14995, C = 0.30094, D = 1.9862, E = 0.68854, F = 6.0626. The best fit, also shown in Figure 3.2, gave an exchange constant of J/k = -26.1 K and a powder-averaged g-value of 2.21. The g-value obtained by electron paramagnetic resonance is 2.15. Using a g-value of 2.21, the expected magnetic moment for one unpaired electron is 1.91 μ_B, which is in good agreement to the value of 1.99 μ_B obtained from the susceptibility data fit. The successful fit of the magnetic data to the Heisenberg model not only gave the coupling strength of the magnetic centers but also suggests that the interactions are isotropic. This result is not surprising considering that the Cu(II) ion, S = 1/2, has no zero-field splitting and the g-value anisotropy is typically not large.[12]

Sr_3NiPtO_6: The synthesis of Sr_3NiPtO_6 was described in Chapter 2. Precession photographs of Sr_3NiPtO_6 crystals revealed hexagonal symmetry with no obvious twinning. Attempts to refine the single crystal structure in a hexagonal space group, however, were not successful. Refining the structure in a rhombohedral space group, $R\bar{3}c$, and in the monoclinic space group, C2/c, of the isotypic Sr_3CuPtO_6 gave qualitatively similar structures with R = 6.1% and R = 5.5%, respectively. Close examination of the X-ray diffration data, however, showed systematic absences that were inconsistent with hexagonal, rhombohedral, or monoclinic symmetry, suggesting that the as-grown crystals of Sr_3NiPtO_6 are twinned. This observation is consistent with flux grown Sr_3CuPtO_6, which also exhibits twinning.[16] Furthermore, the relatively fast reaction time of electrolysis is often known to strain the reaction product and to produce defects.[17-19] Attempts to grow Sr_3NiPtO_6 at different temperatures and/or different deposition potentials gave no noticeable improvements.

The structure of Sr_3NiPtO_6 was consequently refined by powder X-ray and neutron Rietveld analysis using the program GSAS, see Figure 3.3. The powder samples of Sr_3NiPtO_6 prepared by solid state reactions had an oxygen stoichiometry ranging from 5.9-6.0 as determined by thermogravimetric analysis. The oxygen content was a function of the cooling rate from high temperatures. Reactions in which the furnace was simply turned off from high temperatures gave the most oxygen-deficient materials; however, the samples can be fully oxidized by annealing in oxygen at 500-750 °C. Data collected for both oxygen-deficient and fully oxidized samples were used for Rietveld analysis. No structural differences were observable in the resultant structures indicating that the oxygen deficiencies must be random. The Rietveld refinement was performed both in the space group of the parent compound, A_4PtO_6 (A = Ca, Sr, Ba) $R\bar{3}c$, and in that of the structurally relatedly Sr_3CuPtO_6, C2/c. All attempts to refine the structure in the monoclinice space group diverged, while refinement using the space group and atomic

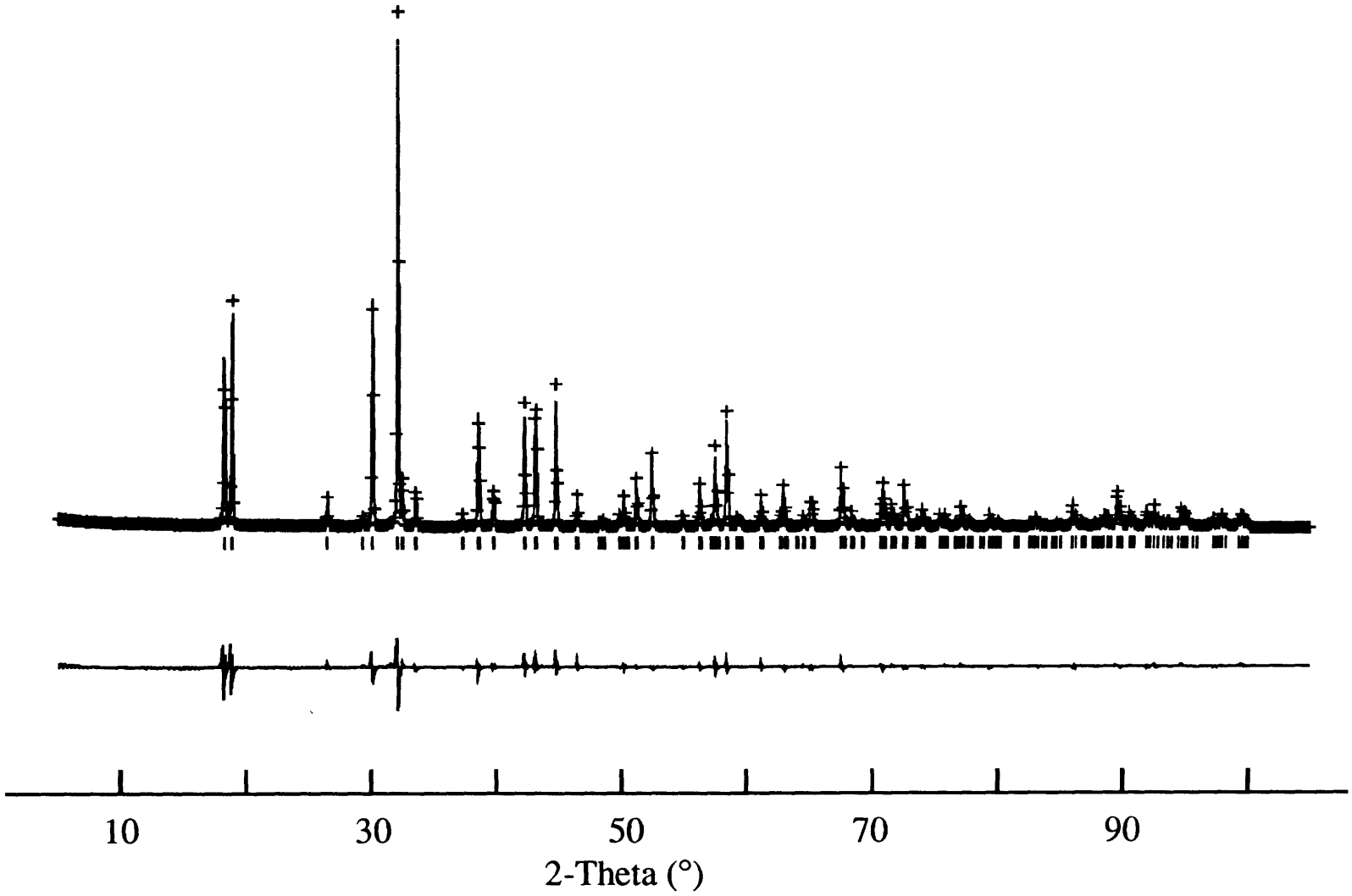

Figure 3.3. Rietveld analysis of the X-ray powder data for Sr_3NiPtO_6 at 298 K showing the observed, calculated, and difference patterns.

Table 3.2: Crystallographic Data for Sr_3NiPtO_6 at 298 K

Formula	Sr_3NiPtO_6
Formula weight	612.65
Color	Light brown powder
Space group	$R\bar{3}c$ (#167)
a, Å	9.5832(1)
c, Å	11.1964(1)
V, $Å^3$	890.51
Z	6
D_{calc}, g/cm^3	6.792
λ, Å	Cu K_α X-ray, 1.5405
2θ scan range (°)	5-105
Step interval (°2θ)	0.01
Maximum step intensity (counts)	66740
Number of unique reflections	216
Number of structural parameters†	7
Number of background parameters	6
Number of profile parameters	6
Refinement	Rietveld using GSAS[a] with pseudo-Voigt[b] peak shape function
R_{wp}[c]	0.146
R_p[d]	0.108
GOF (R_{wp}/R_e)	4.61
χ^2	21.39

† Includes atomic positional and displacement parameters and unit-cell dimensions.

[a] General Structure Analysis System, LANSCE, Los Alamos National Laboratory.

[b] J. Appl. Cryst. **15**, 615-620, 1982.

[c] $R_{wp} = [\Sigma w(I_o-I_c)^2/\Sigma wI_o^2]$

[d] $R_p = \Sigma|I_o-I_c|/\Sigma I_o$, where I_o and I_c are the observed and calculated integrated intensities, respectively, and w is the weight derived from an error propagation scheme during the least square refinement process.

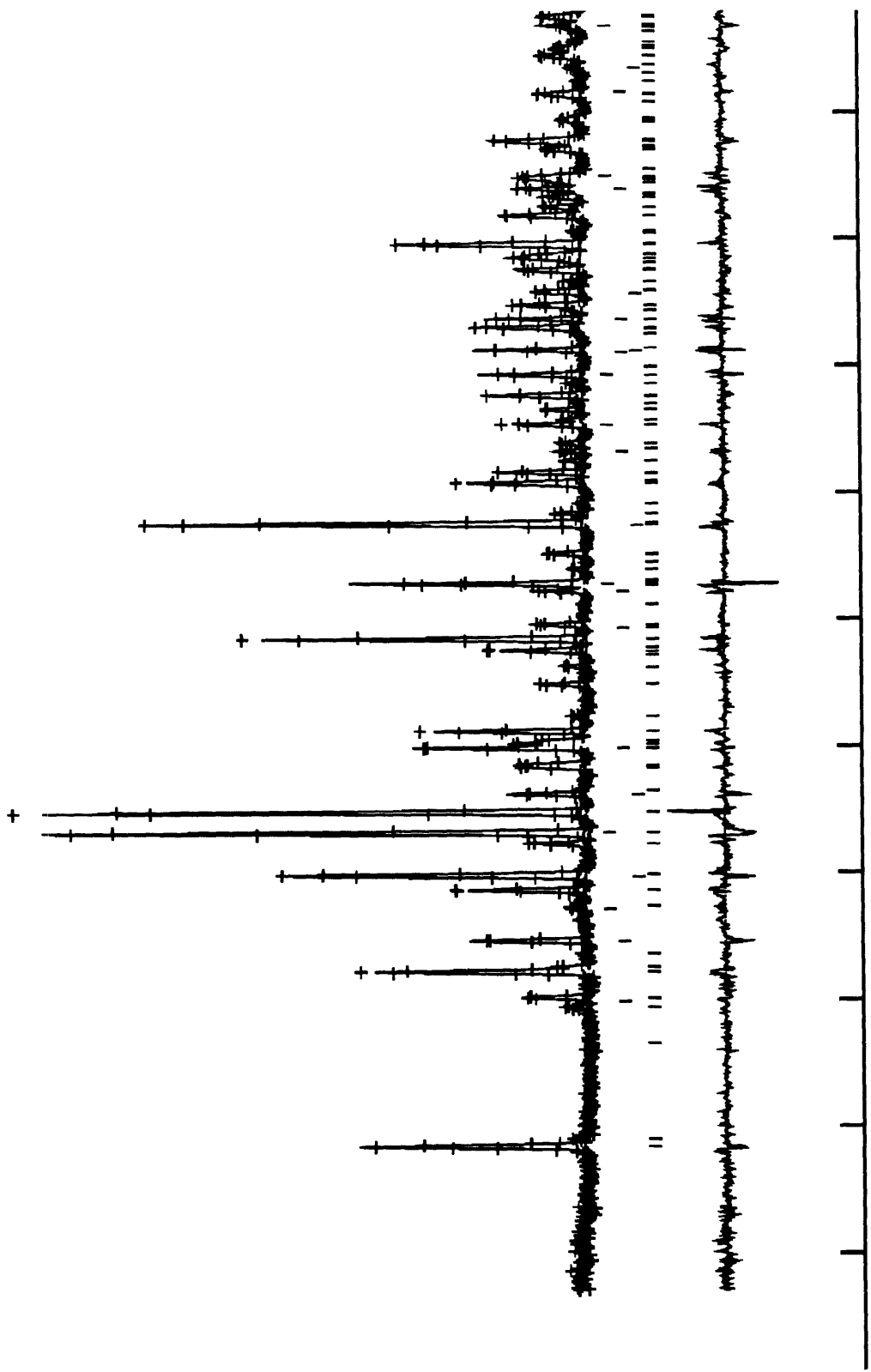

Figure 3.4. Rietveld analysis of the neutron powder data for Sr_3NiPtO_6 at 298K showing the observed, calculated, and difference patterns. From top to bottom, the tick markers are for NiO, SrO, Pt and Sr_3NiPtO_6.

Table 3.3: Crystallographic Data for Sr_3NiPtO_6 at 298K

Formula	Sr_3NiPtO_6
Formula weight	612.65
Color	Light brown powder
Space group	$R\bar{3}c$ (#167)
a, Å	9.5932(4)
c, Å	11.2202(5)
V, $Å^3$	894.253
Z	6
D_{calc}, g/cm^3	6.825
λ, Å	neutron, 1.5400
2θ scan range (°)	7-120
Step interval (°2θ)	0.05
Maximum step intensity (counts)	4,000
Number of unique reflections	156
Number of structural parameters†	7
Number of background parameters	12
Number of profile parameters	6
Refinement	Rietveld using GSAS[a] with pseudo-Voigt[b] peak shape function
R_{wp}[c]	0.094
R_p[d]	0.073
GOF (R_{wp}/R_e)	1.60
χ^2	2.59

† Includes atomic positional and displacement parameters and unit-cell dimensions.

[a] General Structure Analysis System, LANSCE, Los Alamos National Laboratory.

[b] J. Appl. Cryst. **15**, 615-620, 1982.

[c] $R_{wp} = [\Sigma w(I_o-I_c)^2/\Sigma wI_o^2]$

[d] $R_p = \Sigma|I_o-I_c|/\Sigma I_o$, where I_o and I_c are the observed and calculated integrated intensities, respectively, and w is the weight derived from an error propagation scheme during the least square refinement process.

Table 3.4: Atomic Positions of Sr_3NiPtO_6 from Refinement of X-ray Data

Atom	x	y	z
Sr	2/3	-0.0315(1)	0.5833(1)
Pt	1/3	-1/3	2/3
Ni	1/3	-1/3	0.4167(1)
O	0.3593(5)	-0.1582(5)	0.5506(35)

Table 3.5: Selected Bond Distances and Angles from Refinement of X-ray Data

Pt-O (x6)	2.037(4)
Pt-Ni (x2)	2.799(4)
Ni-O (x6)	2.170(4)
Sr-O (x2)	2.590(4)
Sr-O (x2)	2.752(5)
Sr-O (x2)	2.464(4)
Sr-O (x2)	2.683(4)
O-Pt-O (x6)	83.68(16)
O-Pt-O (x6)	96.32(16)
O-Pt-O(x3)	180.0

Table 3.6: Atomic Positions of Sr_3NiPtO_6 from Refinement of Neutron Data

Atom	x	y	z
Sr	2/3	-0.0314(2)	0.5833(1)
Pt	1/3	-1/3	2/3
Ni	1/3	-1/3	0.4167(1)
O	0.3566(3)	-0.1595(3)	0.5535(2)

Table 3.7: Selected Bond Distances and Angles from Refinement of Neutron Data

Pt-O (x6)	2.017(2)
Pt-Ni (x2)	2.805(1)
Ni-O (x6)	2.194(2)
Sr-O (x2)	2.610(2)
Sr-O (x2)	2.729(3)
Sr-O (x2)	2.486(3)
Sr-O (x2)	2.662(2)
O-Pt-O (x6)	84.60(9)
O-Pt-O (x6)	95.40(9)
O-Pt-O(x3)	180.0

positions of A_4PtO_6 quickly converged, see Table 3.2. The structure was also refined using powder neutron diffraction data. Although the neutron data had some residual starting material as impurities, refinement of the neutron data gave the same structure as that obtained from X-ray data, see Figure 3.4 and Table 3.3, confirming the powder X-ray refinement.

Sr_3NiPtO_6 has a structure closely related to the one-dimensional structure of A_4PtO_6, described earlier. In Sr_3NiPtO_6, the alkaline earth cation situated within the chains has been replaced by the nickel cation and, consequently, the platinum and nickel metal now alternate along the infinite chain. The chain structure of Sr_3NiPtO_6, shown in Figure 5 with the A_4PtO_6 structure, consists of alternating face-sharing PtO_6 octahedra and NiO_6 trigonal prisms. Figure 3.6 shows the complete structure viewed down the c-axis. Table 3.4 lists the atomic positions and their esd's as refined from X-ray diffraction data, and selected bond distances and angles are displayed in Table 3.5. For comparison, Table 3.6 lists the atomic positions and their esd's as refined from the powder neutron data, and selected bond distances and angles are displayed in Table 3.7.

Magnetic susceptibility studies of polycrystalline Sr_3NiPtO_6 in fields of 1, 5, and 40 kG indicate an onset of magnetic ordering at ~25 K as shown in Figure 3.7. The susceptibilities in different fields are all qualitatively similar. The magnetic behavior of Sr_3NiPtO_6 is characteristic of many linear chain materials.[12,20,21] At low temperatures, the susceptibility decreases and flattens indicating an order-disorder transition associated with an antiferromagnetic transition. The increase in susceptibility at 4 K is presumably due to paramagnetic impurities. The susceptibility also suggests only short range ordering in this system since the susceptibility does not "turn over" as in other antiferromagnets, for example, Sr_3CuPtO_6. Powder neutron diffraction studies of the Sr_3NiPtO_6 at 10 K gave the identical diffraction pattern as that obtained at room temperature with no magnetic peaks confirming the absence of long range order. We have attempted to fit the susceptibility data to a S = 1 one-dimensional Heisenberg

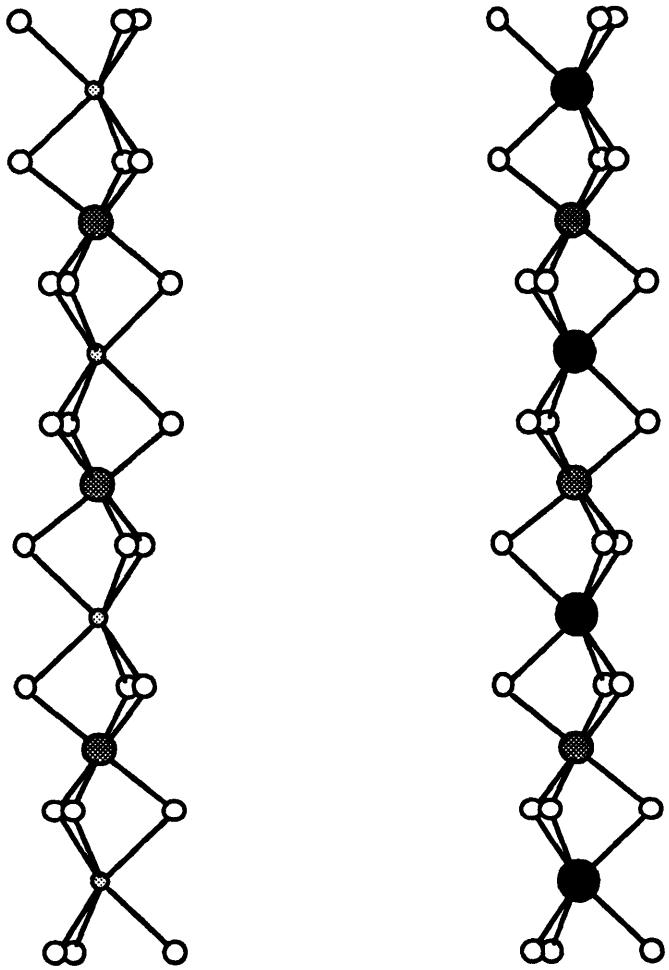

Figure 3.5. Left, one chain in Sr_3NiPtO_6 showing alternating NiO_6 trigonal prisms and PtO_6 octahedra. On the right, the nickel atom has been replaced by the (black) alkaline earth element, A, as in the parent structure A_4PtO_6 (A = Ca, Sr, Ba).

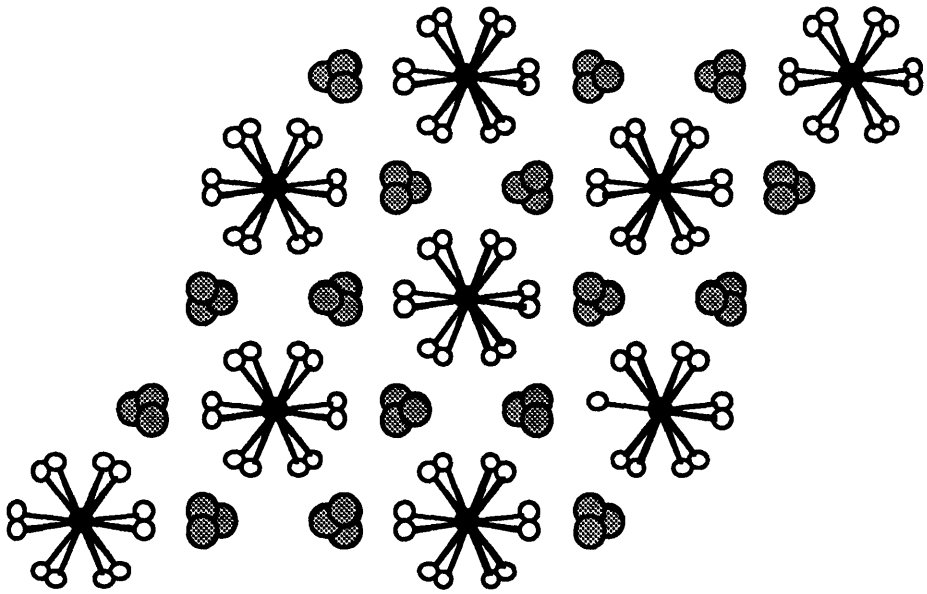

Figure 3.6. The structure of Sr_3NiPtO_6 viewed along the c-axis.

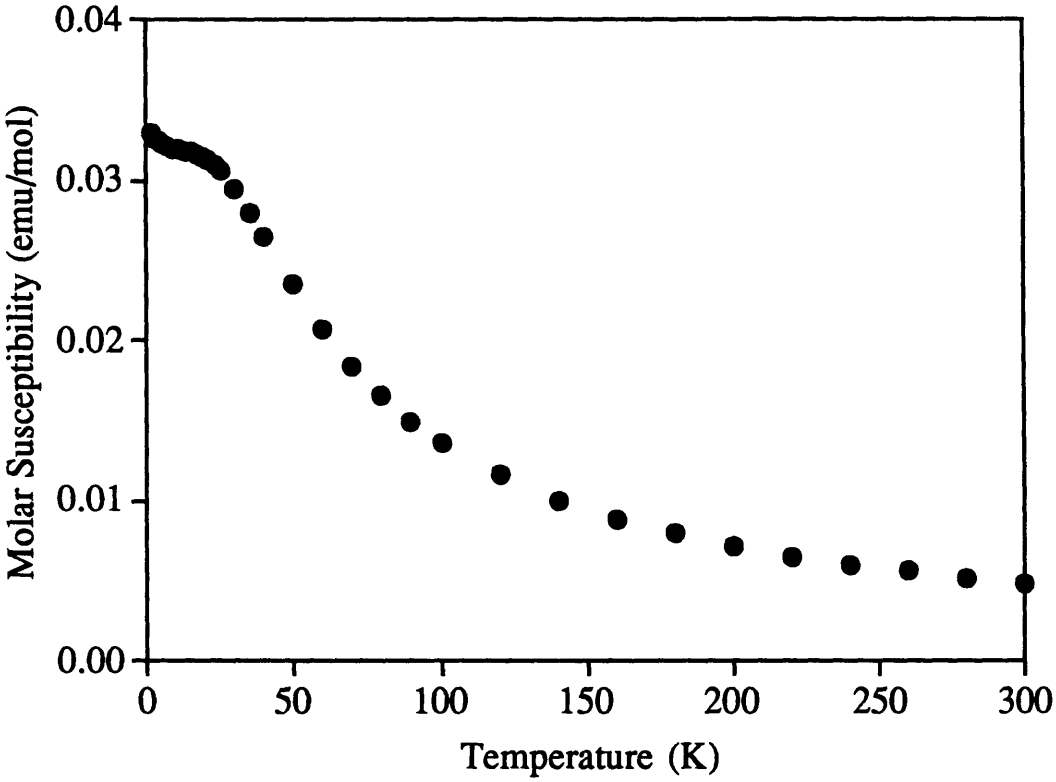

Figure 3.7. Magnetic susceptibility of Sr_3NiPtO_6 at 5 kG showing the onset of low-dimensional antiferromagnetism at ~25 K. The Curie-like tail at 4 K is presumably due to paramagnetic impurities.

antiferromagnetic model[22] with a paramagnetic correction for the impurities, however the fit was poor. A Curie-Weiss fit of the susceptibility above 50 K yielded θ = -14.1 K and 3.35 μ_B per mole of Sr_3NiPtO_6. A spin-only value of 2.83 μ_B (equivalent to two unpaired electrons) would be expected for trigonal prismatic Ni(II), d^8 and low-spin octahedral Pt(IV), d^6. Ni(II) oxides, however, typically exhibit magnetic moments near 3.2 μ_B due to spin-orbit coupling.[23]

As mentioned earlier, S = 1 one-dimensional chain systems have attracted much attention recently because they can possess an unusual quantum phenomenon known as a Haldane gap.[3,4] Sr_3NiPtO_6 is a one-dimensional system with S = 1. However, in our system, there is no evidence, such as a decrease in magnetic susceptibility at low temperatures, of a gap. The absence of a Haldane gap could be due to high single ion anisotropy of the magnetic centers in addition to low coupling exchange.[24] Also, Sr_3NiPtO_6 contains alternating Ni (II) (S = 1) and Pt(IV) (S = 0) along the chains. All reported Haldane systems, however, have contained chains with uniform magnetic centers, namely, Ni(II).[2,6,7,24,25]

Sr_3CoPtO_6: This material was structurally characterized by both powder X-ray and neutron diffraction, shown in Figures 3.8 and 3.9. The structure was refined by Rietveld analysis (Table 3.8 and 3.9) and found to be isostructural with Sr_3NiPtO_6. Table 3.10 lists the atomic positions and their esd's as refined from X-ray diffraction data, and selected bond distances and angles are displayed in Table 3.11. For comparison, Table 3.12 lists the atomic positions and their esd's as refined from the powder neutron data, and selected bond distances and angles are displayed in Table 3.13. The trigonal prismatic site is now occupied by the cobalt, while the platinum still retains its octahedral coordination.

Magnetic studies of polycrystalline Sr_3CoPtO_6 indicate Curie-like paramagnetism, as shown in Figure 3.10. A fit of the data to the Curie-Weiss law reveals

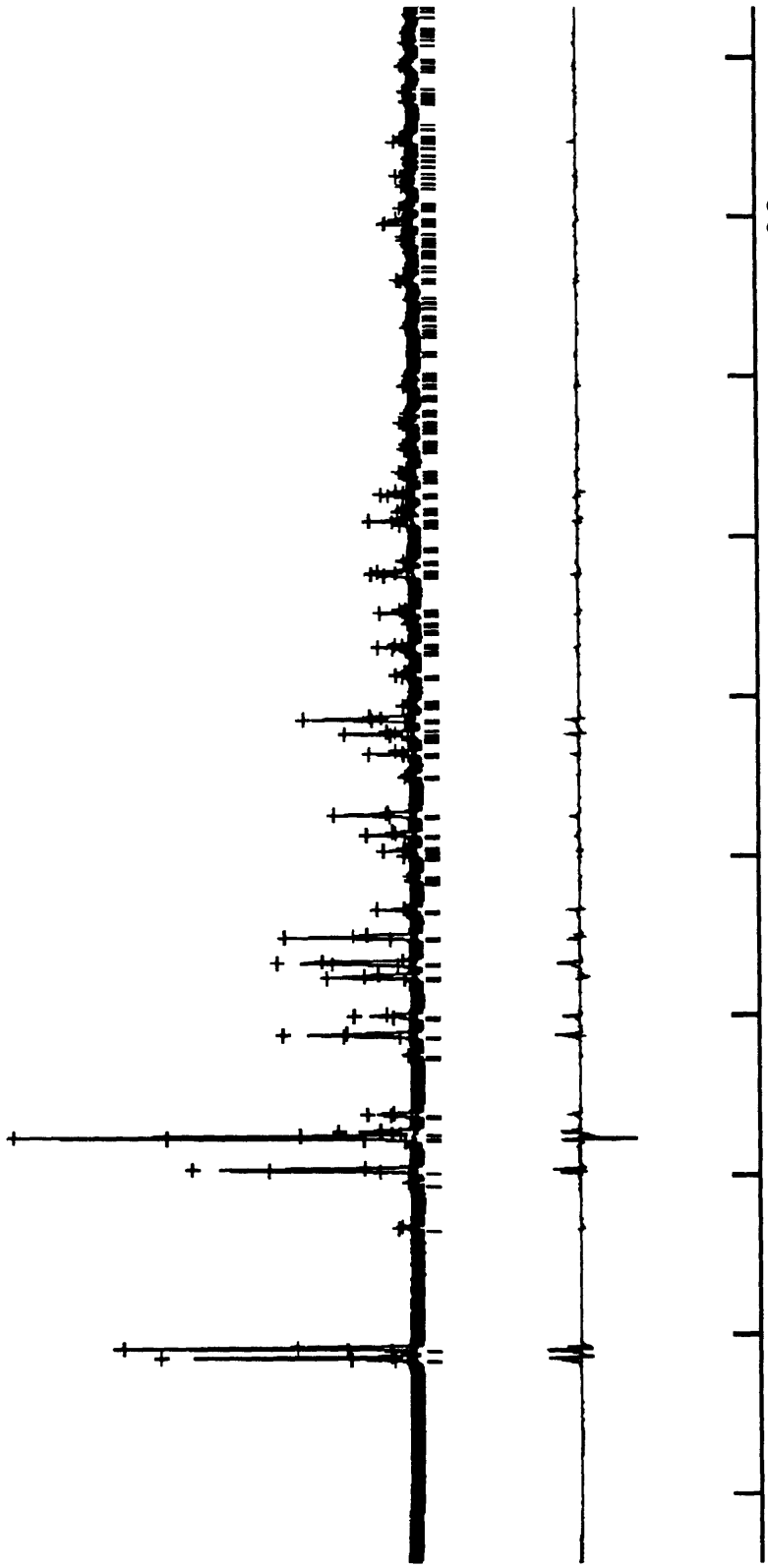

Figure 3.8. Rietveld analysis of the X-ray powder data for Sr_3CoPtO_6 at 298 K showing the observed, calculated, and difference patterns.

Table 3.8: Crystallographic Data for Sr_3CoPtO_6 at 298 K

Formula	Sr_3CoPtO_6
Formula weight	612.88
Color	Dark brown powder
Space group	$R\bar{3}c$ (#167)
a, Å	9.5959(1)
c, Å	11.2123(2)
V, $Å^3$	894.119
Z	6
D_{calc}, g/cm^3	6.828
λ, Å	Cu K_α X-ray, 1.5405
2θ scan range (°)	5-105
Step interval (°2θ)	0.01
Maximum step intensity (counts)	52,000
Number of unique reflections	236
Number of structural parameters†	7
Number of background parameters	7
Number of profile parameters	8
Refinement	Rietveld using GSAS[a] with pseudo-Voigt[b] peak shape function
R_{wp}[c]	0.173
R_p[d]	0.128
GOF (R_{wp}/R_e)	5.48
χ^2	30.07

† Includes atomic positional and displacement parameters and unit-cell dimensions.

[a] General Structure Analysis System, LANSCE, Los Alamos National Laboratory.

[b] J. Appl. Cryst. **15**, 615-620, 1982.

[c] $R_{wp} = [\Sigma w(I_o-I_c)^2/\Sigma wI_o^2]$

[d] $R_p = \Sigma|I_o-I_c|/\Sigma I_o$, where I_o and I_c are the observed and calculated integrated intensities, respectively, and w is the weight derived from an error propagation scheme during the least square refinement process.

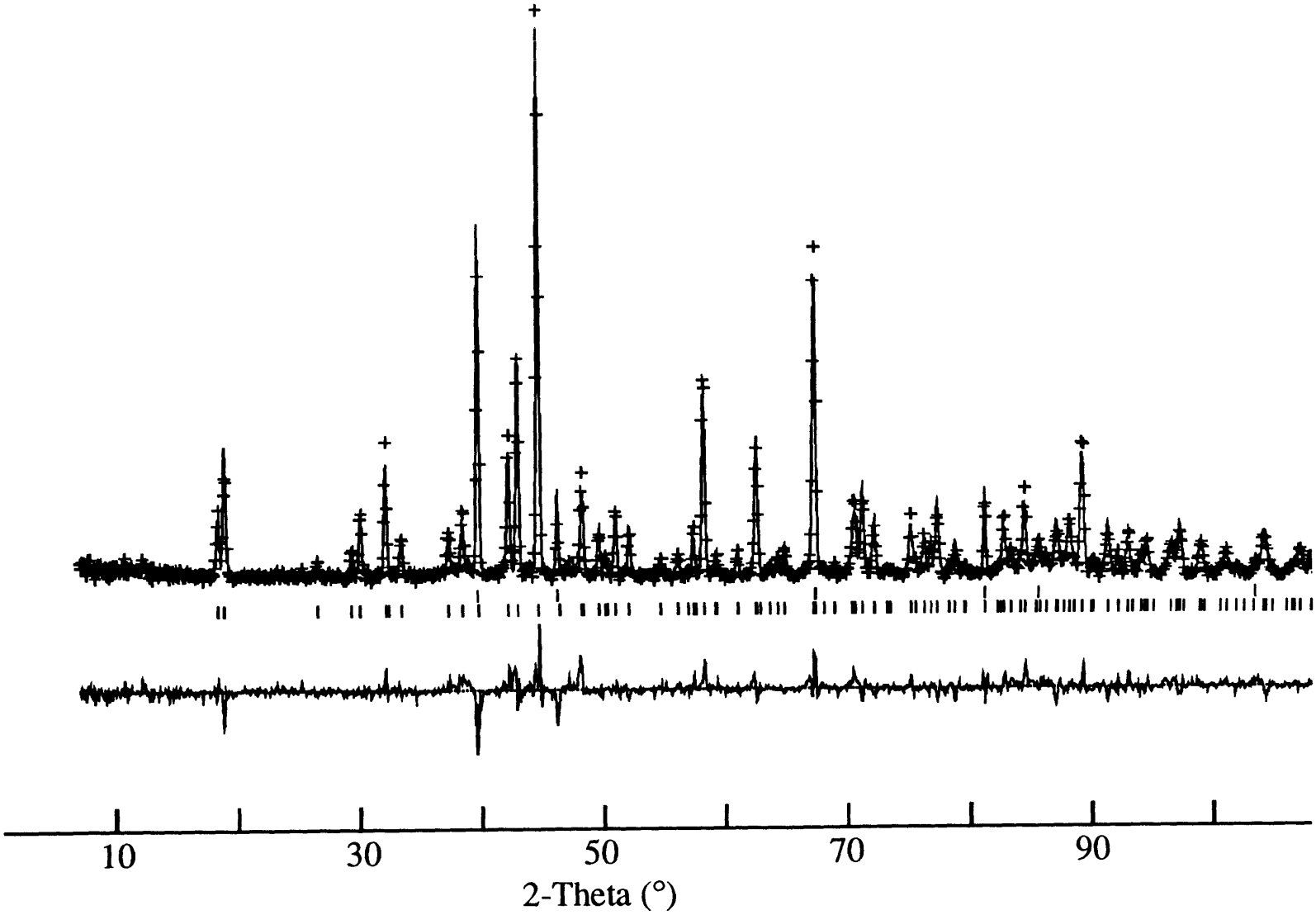

Figure 3.9. Rietveld analysis of the neutron powder data for Sr_3CoPtO_6 at 298 K showing the observed, calculated, and difference patterns. The top and bottom tick markers are for Pt and Sr_3CoPtO_6, respectively.

Table 3.9: Crystallographic Data for Sr_3CoPtO_6 at 298 K

Formula	Sr_3CoPtO_6
Formula weight	612.88
Color	Dark brown powder
Space group	$R\bar{3}c$ (#167)
a, Å	9.6152(5)
c, Å	11.2808(6)
V, $Å^3$	903.206
Z	6
D_{calc}, g/cm^3	6.759
λ, Å	neutron, 1.5400
2θ scan range (°)	7-130
Step interval (°2θ)	0.05
Maximum step intensity (counts)	3,600
Number of unique reflections	173
Number of structural parameters†	7
Number of background parameters	12
Number of profile parameters	6
Refinement	Rietveld using GSAS[a] with pseudo-Voigt[b] peak shape function
R_{wp}[c]	0.103
R_p[d]	0.083
GOF (R_{wp}/R_e)	1.51
χ^2	2.31

† Includes atomic positional and displacement parameters and unit-cell dimensions.

[a] General Structure Analysis System, LANSCE, Los Alamos National Laboratory.

[b] J. Appl. Cryst. **15**, 615-620, 1982.

[c] $R_{wp} = [\Sigma w(I_o-I_c)^2/\Sigma w I_o^2]$

[d] $R_p = \Sigma|I_o-I_c|/\Sigma I_o$, where I_o and I_c are the observed and calculated integrated intensities, respectively, and w is the weight derived from an error propagation scheme during the least square refinement process.

Table 3.10: Atomic Positions of Sr_3CoPtO_6 from Refinement of X-ray Data

Atom	x	y	z
Sr	2/3	-0.0315(1)	0.5833(1)
Pt	1/3	-1/3	2/3
Co	1/3	-1/3	0.4167(1)
O	0.3545(6)	-0.1580(5)	0.5522(4)

Table 3.11: Selected Bond Distances and Angles from Refinement of X-ray Data

Pt-O (x6)	2.044(2)
Pt-Co (x2)	2.803(4)
Co-O (x6)	2.199(2)
Sr-O (x2)	2.633(3)
Sr-O (x2)	2.712(4)
Sr-O (x2)	2.454(2)
Sr-O (x2)	2.661(3)
O-Pt-O (x6)	84.73(1)
O-Pt-O (x6)	95.27(1)
O-Pt-O(x3)	180.0

Table 3.12: Atomic Positions of Sr_3CoPtO_6 from Refinement of Neutron Data

Atom	x	y	z
Sr	2/3	-0.0312(3)	0.5833(1)
Pt	1/3	-1/3	2/3
Co	1/3	-1/3	0.4167(1)
O	0.3552(3)	-0.1586(3)	0.5550(2)

Table 3.13: Selected Bond Distances and Angles from Refinement of Neutron Data

Pt-O (x6)	2.024(2)
Pt-Co (x2)	2.820(1)
Co-O (x6)	2.225(2)
Sr-O (x2)	2.627(2)
Sr-O (x2)	2.722(3)
Sr-O (x2)	2.489(3)
Sr-O (x2)	2.652(2)
O-Pt-O (x6)	85.40(8)
O-Pt-O (x6)	94.60(8)
O-Pt-O(x3)	180.0

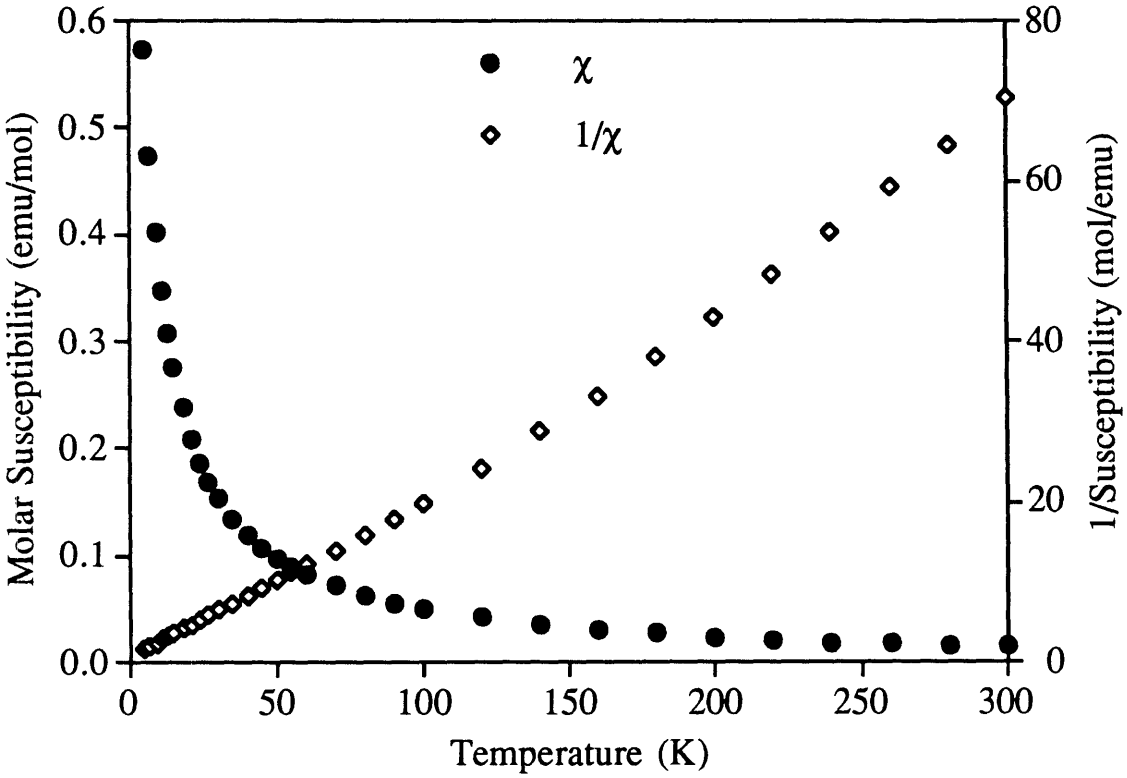

Figure 3.10. Magnetic susceptibility and inverse susceptibility of Sr_3CoPtO_6 showing Curie-like behavior.

two unusual features: a small Weiss constant, θ, of 3.12 K and an unexpected moment of 5.96 μ_B. Five unpaired electrons would be expected to give a spin-only moment of 5.92 μ_B. Clearly, this system does not contain Pt(IV) and Co(II) since this combination of oxidation states would give at most three unpaired electrons--three electrons from cobalt and zero from low-spin platinum. A combination of oxidation states containing Pt(III) is highly unlikely since Pt(III) tends to be unstable in the solid state.[26] One possibility of oxidation states that could explain the five unpaired electrons is a mixture of Co(II), high spin d^5, and Pt(II), low spin d^8. This explanation, however, is unlikely since Co(IV) tends to adopt tetrahedral coordination in the solid state, and the X-ray data do not indicate any kind of structural distortions from trigonal prismatic to tetrahedral coordination. The presence of only Pt(II) is also unlikely since these materials were synthesizized at high temperatures in air. Also, if only Pt(II) existed in the material, then the cobalt must be tetravalent to maintain charge balance. This couple of Pt (II) and Co(IV) should be unstable since, based on reduction potential arguments, the Pt(II) is expected to oxidize to Pt(IV) and the Co(IV) will reduce.[27] Thus, the only combination of oxidation states that could account for five unpaired electrons as well as maintain charge balance is one that contains Co(III) and a mixture of Pt(II)/Pt(IV). High spin, d^6 Co(III) in trigonal prismatic coordination would contribute four unpaired electrons. If platinum in the octahedral site disproportionates into Pt(II), d^8, and Pt(IV), d^6, then on average, the platinum would contribute one unpaired electron. Oxides containing mixed-valent platinum(II/IV) are known to exist and have been confirmed by X-ray photoelecron spectroscopy.[28]

Sr_3CoPtO_6 was characterized by XPS to confirm the existence of Pt(II) and Pt(IV), as well as to test for the possibility of Pt(III) in the sample. Data were collected on powdered samples pressed into indium foils to reduce charging, and all peak positions were corrected using the carbon 1S peak as an internal standard. The XPS spectrum of the platinum region in Sr_3CoPtO_6 is shown in Figure 3.11. The Pt 4f peaks show the

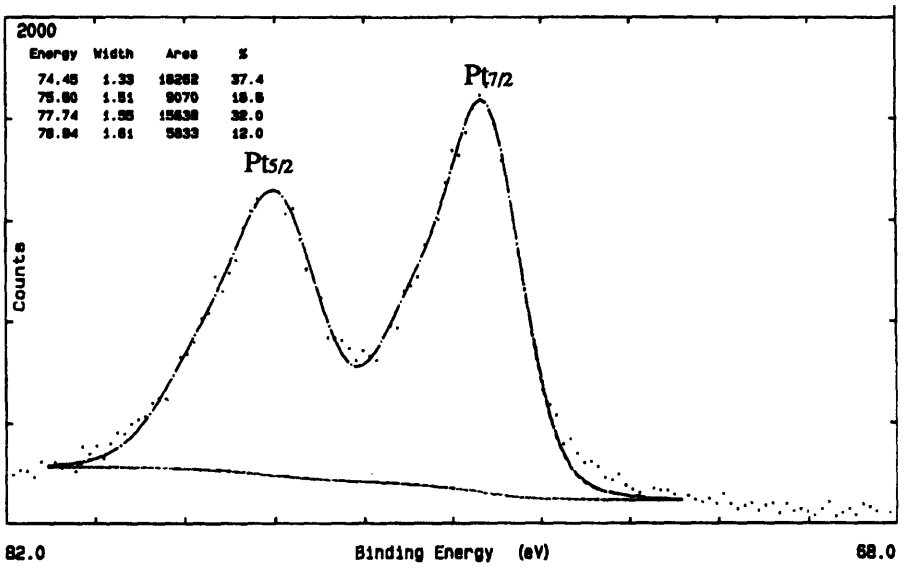

Figure 3.11. Pt region of the X-ray photoelectron spectrum of Sr_3CoPtO_6. The peak positions and half-band widths support the existence of Pt(II) and Pt(IV).

asymmetry exhibited by all platinum samples as well as an area ratio of 1.27, in good agreement with the theoretical value of 1.33. The corrected position of Pt 4f(7/2) peak is 73.9 eV, between the binding energy of Pt(II) and Pt(IV). The binding energy of Pt(II) in PtO is 73.3 eV, and Pt(IV) in PtO_2 has a binding energy of 74.2 eV.[29] Furthermore, Sr_3CoPtO_6 has a half-band width of 1.96 eV for its Pt 4f(7/2) peak. This width is appreciably greater than the usual half-band widths of 1.2-1.3 eV for platinum in oxides.[29] The broadening of the Pt 4f peaks is indicative of a mixture of Pt(II) and Pt(IV).[28] Thus, Sr_3CoPtO_6 appears to be mixed-valent by XPS, and the more descriptive chemical formula may be written as $Sr_6Co(III)_2Pt(II)Pt(IV)O_{12}$.

The other unusual characteristic of Sr_3CoPtO_6 is the small Weiss constant of 3.12 K that suggest near perfect Curie paramagnetism or no magnetic ordering. The small, positive Weiss constant usually indicates the presence of weak ferromagnetic interactions. However, as shown in Figure 3.12, a plot of χT, or the effective moment from the Curie law, versus T clearly indicates a decrease in magnetic moment, i.e., antiferromagnetic coupling, at low temperatures. This antiferromagnetism can also be observed in the heat capacity measurements, shown in Figure 3.13. The sharp peak at low temperatures has been assigned to an antiferromagnetic transition. It would appear that Sr_3CoPtO_6 is an antiferromagnet with an ordering temperature of 1.4 K.

It is worthwhile to note that while the χT plot and heat capacity measurements indicate antiferromagnetism in Sr_3CoPtO_6, the Curie law fit of the entire susceptibility data indicates ferromagnetic interactions, $\theta = 3.12$ K. Within the error of the SQUID, this low Weiss constant implies near perfect Curie paramagnetism. Furthermore, integration of the heat capacity data to yield the total spin entropy gave a value corresponding to only ~1 electron, not the 5 electrons calculated from the magnetic data. Clearly, the analysis of the magnetic properties of Sr_3CoPtO_6 is not straightforward.

As mentioned earlier, all one-dimensional magnetic systems are known to undergo long range ordering at finite temperatures. One-dimensional systems are limited

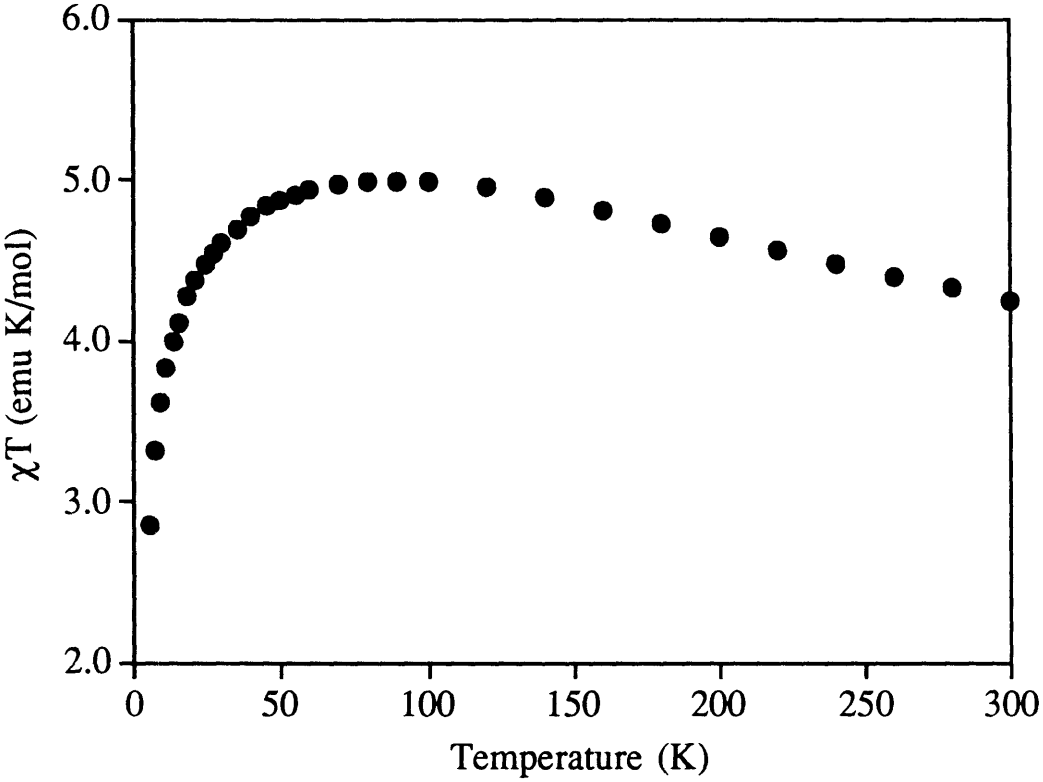

Figure 3.12. χT plot of Sr_3CoPtO_6 showing the change in effective magnetic moment as a function of temperature.

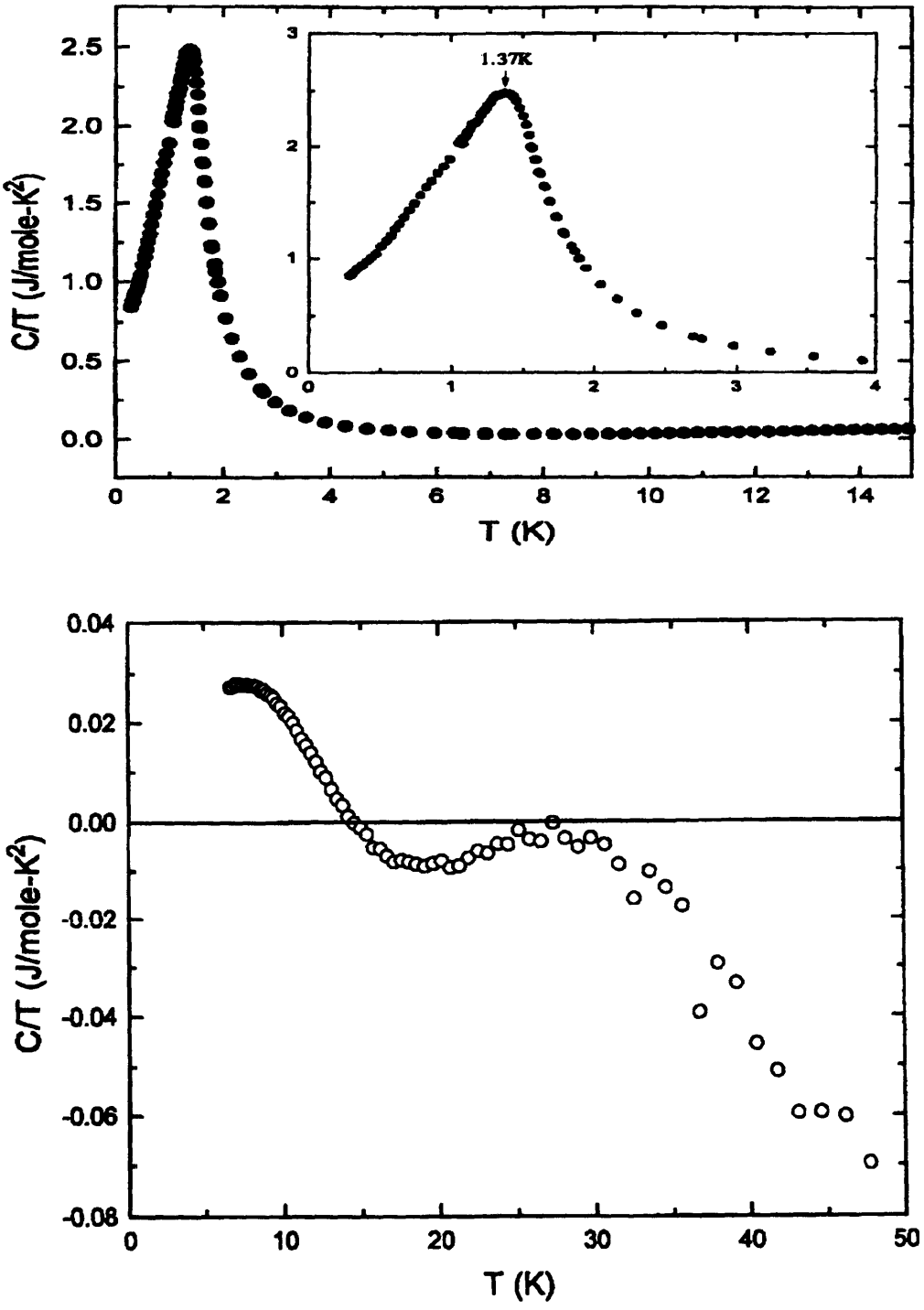

Figure 3.13. Top, heat capacity of Sr_3CoPtO_6 from 0.3-15 K showing an antiferromagnetic transition at 1.37 K. Bottom, heat capacity from 6-50 K.

to one degree of freedom to arrange their spins, and thus, all combinations of spin arrangements inevitably lead to states of net ferromagnetism or antiferromagnetism. But what happens if a one-dimensional system contains both ferromagnetic and antiferromagnetic exchange randomly distributed *within* the chains? Lee, et. al., have proposed the random spin chain model as a theoretical prediction for the magnetic behavior of a one-dimensional system containing intrachain ferromagnetic and antiferromagnetic coupling.[30] This model focuses on the basic expression of magnetic susceptibility:

$$\chi = \frac{\mu^2}{T}\left(\sum_i \langle S_i^2 \rangle + \sum_{i \neq j} \langle S_i \cdot S_j \rangle\right)$$

where the terms ($\Sigma \langle S_i^2 \rangle$) and ($\Sigma \langle S_i \cdot S_j \rangle$) are the sum-averaged interactions of the individual spins and the interactions of a spin with its neighbors, respectively. In a typical material, the second term is positive ($J > 0$) for a ferromagnet and negative ($J < 0$) for an antiferromagnet. In a random spin material, however, both types of interactions exist, as shown below:

Scheme 3.1

Averaging over the entire chain, the second term in the susceptibility expression, ($\Sigma \langle S_i \cdot S_j \rangle$), reduces to zero. The susceptibility can then be rewritten as $\chi = \mu^2 N \langle S^2 \rangle / T = C/T$, which is simply the Curie Law. Thus, the random spin model predicts that a one-dimensional material with random ferromagnetic and antiferromagnetic exchange will have a magnetic susceptibility that appears Curie-like. However, unlike a paramagnet in which the spins are *not* interacting, a material with random spin possesses a ground state in which the spins have a distinct arrangement and *are coupled*. It is not possible to observe this coupling in the susceptibility data because magnetic measurements only give

the average magnetic exchange interaction. For both a ferromagnet and an antiferromagnet, the exchange is finite and non-zero. A random spin magnet *averaged* exchange is zero, just as in a paramagnet, making them indiscernable by magnetic measurements.

However, the random spin material undergoes a phase transition to a distinct ground state, and it should be possible to detect this transformation by heat capacity measurements. The heat capacity measurements are predicted to give two transitions according to the random spin model. Referring to Scheme 3.1, the chains in a one-dimensional random spin magnet are composed of randomly arranged spins. Upon cooling in temperature, there is an ordering transition corresponding to the coupling of the spins with its neighbors to form discrete islands. This transition should occur at temperatures near the value of (1/4)J. Along the chains there will be sections of the chain or "islands" in which the spins are ferromagnetically coupled. As the spins align in each section, they act as one large spin. These islands are separated by regions of antiferromagnetically coupled spins or other islands of opposite spin direction. At lower temperatures, there is a second transition corresponding to the coupling of the ferromagnetic islands to give an averaged total singlet ground state. Thus, a random spin magnet can be described as a special type of antiferromagnet. An antiferromagnet contains antiparallel coupling between *individual spins*, but in a random spin magnet, the exchange is between *ferromagnetic islands*.

Sr_3CoPtO_6 does indeed show evidence of random spin magnetism. The presence of mixed-valent platinum may cause the spins to arrange randomly. As shown in the χT plot of Figure 3.12, the effective moment does increase (and suggests ferromagnetic interactions) before turning over to indicate antiferromagnetism. The peak in the low temperature heat capacity measurements (Figure 3.13, top) is also consistent with random spin magnetism. This peak is due to coupling of the ferromagnetic islands. At higher temperatures, ~7 K, (Figure 3.13, bottom) there is a small peak that may be assigned to

coupling of the spins to form the ferromagnetic islands. The data for the lower curve (Figure 3.13, bottom) was obtained by subtracting the heat capacity of the isostructural Sr_3ZnPtO_6 from that of Sr_3CoPtO_6. Diamagnetic Sr_3ZnPtO_6 was used as an approximate background material to eliminate phonon contributions to the specific heat. Without this diamagnetic correction, the phonon contribution would overwhelm and mask any magnetic contribution to the specific heat. The corrected heat capacity curve of Sr_3CoPtO_6, therefore, represents only the magnetic entropy contribution to the heat capacity. The position of the peak in Figure 3.13, bottom, appears at ~7 K, or 1/4 of the J-value, as predicted from the random spin model. The corrected J-value of ~28 K is close to the observed J-values of Sr_3CuPtO_6 and Sr_3NiPtO_6, 26 K and ~20 K, respectively.

Sr_3ZnPtO_6: This light yellow material was synthesized to serve as a diamagnetic background reference for the heat capacity measurements of Sr_3CoPtO_6. Sr_3ZnPtO_6 contains Zn(II), d^{10}, and low-spin octahedral Pt(IV), d^6. Consequently, it contains no unpaired electrons and is diamagnetic. The structure was refined using powder X-ray Rietveld analysis. The results are shown in Figure 3.14 and Table 3.14. Table 3.15 lists the atomic positions and their esd's as refined from X-ray diffraction data, and selected bond distances and angles are displayed in Table 3.16. The structure is the same as that for Sr_3NiPtO_6 with only slight changes in the oxygen atomic positions.

Trends in the Magnetic Data:

The focus of this chapter has been the magnetic characterization of the one-dimensional oxides, Sr_3MPtO_6, where M = Zn, Cu, Ni, and Co. The structure was able to accommodate substitution on the trigonal prismatic M site, allowing for the systematic study of the composition-magnetic property relationship. In performing substitutions on the M site using Zn, Cu, Ni, and Co, unpaired electrons can be systematically and selectably placed on this site without altering the Pt site. Sr_3ZnPtO_6 contains no unpaired

electrons on the Zn(II) site and no unpaired electrons on the Pt(IV) site. This material is diamagnetic. In substituting Zn(II) with Cu(II), d^9, one unpaired electron is added to the M site to give a S = 1/2 material. The preference of Cu(II) to have square planar coordination distorts the structure from space group $R\bar{3}c$ to C2/c. Sr_3CuPtO_6 displays one-dimensional antiferromagnetism. The magnetic behavior was understood by modelling to the antiferromagnetic Heisenberg linear chain model. Sr_3CuPtO_6 is an antiferromagnet which contains isotropic exchange between nearest neighbors. In substituting Cu(II) with Ni(II), d^8, an additional electron is placed on the trigonal prismatic M site to give a S = 1 material. Sr_3NiPtO_6 also displays low-dimensional antiferromagnetism, however, the magnetic behavior was complex and could not be fitted to a S = 1 Heisenberg model. The absence of a Haldane gap in this S = 1 system is significant. This absence of a gap may be due to high single ion anisotropy, low coupling exchange, or a non-uniform chain which contains alternating Ni(II) and Pt(IV). Finally, in substituting Ni(II) with cobalt, Co(III) is generated along with mixed-valent Pt(II)/Pt(IV). Sr_3CoPtO_6 is a S = 5/2 system which displays Curie-like paramagnetism. Its magnetic behavior can be better understood through susceptibility measurements as well as heat capacity measurements. Based on these studies, Sr_3CoPtO_6 is the first example of a material to display random spin paramagnetism, as theorized by Lee, et. al. Random spin paramagnetism is a special type of antiferromagnetism in which there is both coupling between nearest neighbors and between ferromagnetic islands, which develop along the one-dimensional chain. Heat capacity measurements confirmed both the coupling of the individual spins and the coupling of the ferromagnetic islands. Thus, in selectably altering the number of unpaired electrons on a site, the magnetic behavior can be altered, and more importantly, this systematic study led to the discovery of a new type of magnetic behavior, random spin chain magnetism.

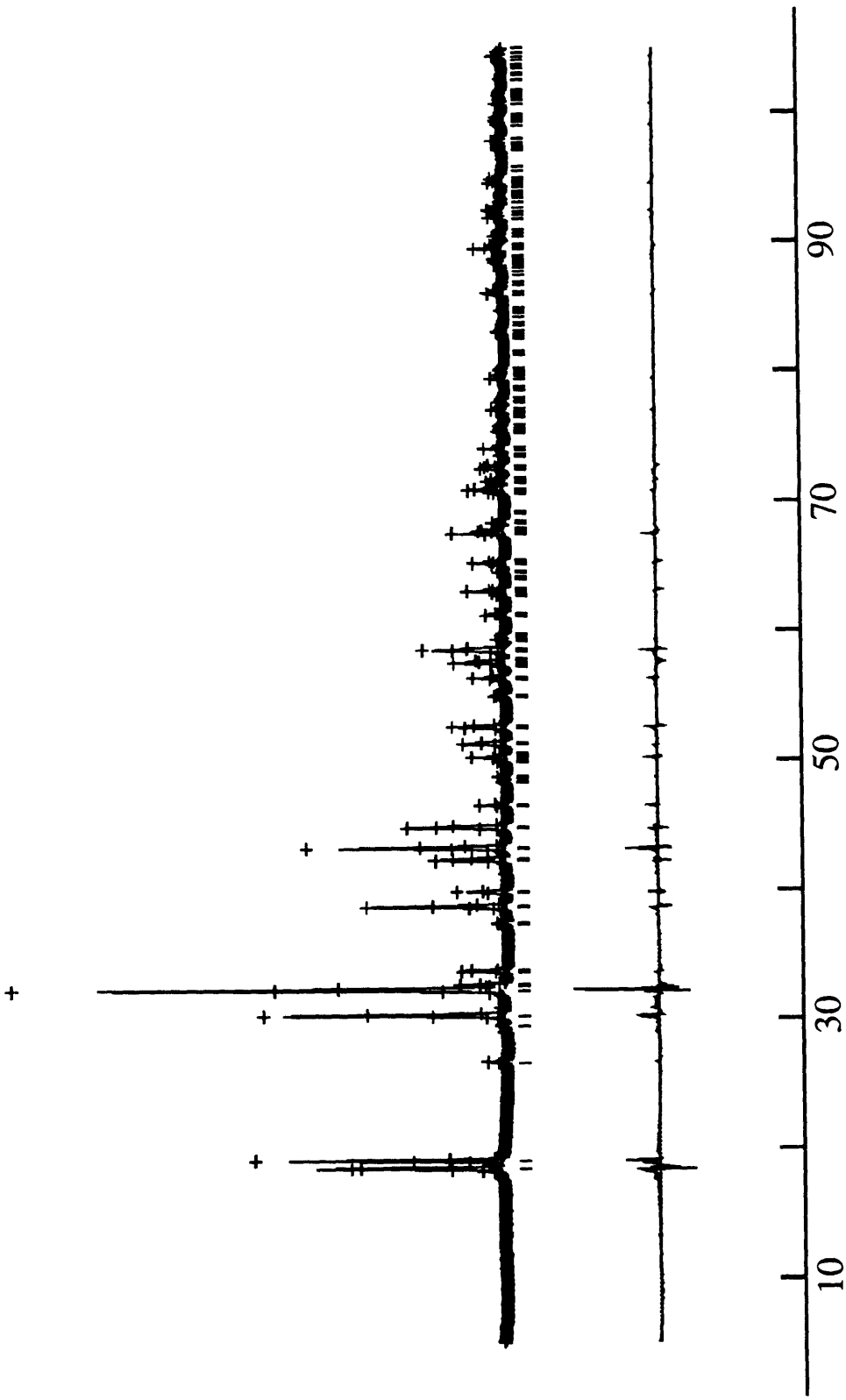

Figure 3.14. Rietveld analysis of the X-ray powder data for Sr_3ZnPtO_6 at 298 K showing the observed, calculated, and difference patterns.

Table 3.14: Crystallographic Data for Sr_3ZnPtO_6 at 298K

Formula	Sr_3ZnPtO_6
Formula weight	619.33
Color	Light yellow powder
Space group	$R\bar{3}c$ (#167)
a, Å	9.6165(2)
c, Å	11.2180(2)
V, $Å^3$	898.409
Z	6
D_{calc}, g/cm^3	6.867
λ, Å	Cu K_α X-ray, 1.5405
2θ scan range (°)	5-105
Step interval (°2θ)	0.01
Maximum step intensity (counts)	40,000
Number of unique reflections	236
Number of structural parameters†	7
Number of background parameters	6
Number of profile parameters	6
Refinement	Rietveld using GSAS[a] with pseudo-Voigt[b] peak shape function
R_{wp}[c]	0.147
R_p[d]	0.112
GOF (R_{wp}/R_e)	4.03
$\chi 2$	16.29

† Includes atomic positional and displacement parameters and unit-cell dimensions.

[a] General Structure Analysis System, LANSCE, Los Alamos National Laboratory.

[b] J. Appl. Cryst. **15**, 615-620, 1982.

[c] $R_{wp} = [\Sigma w(I_o-I_c)^2/\Sigma w I_o^2]$

[d] $R_p = \Sigma|I_o-I_c|/\Sigma I_o$, where I_o and I_c are the observed and calculated integrated intensities, respectively, and w is the weight derived from an error propagation scheme during the least square refinement process.

Table 3.15: Atomic Positions of Sr_3ZnPtO_6 from Refinement of X-ray Data

Atom	x	y	z
Sr	2/3	-0.0316(1)	0.5833(1)
Pt	1/3	-1/3	2/3
Zn	1/3	-1/3	0.4167(1)
O	0.3603(5)	-0.1559(5)	0.5547(4)

Table 3.16: Selected Bond Distances and Angles from Refinement of X-ray Data

Pt-O (x6)	2.028(4)
Pt-Zn (x2)	2.805(6)
Zn-O (x6)	2.221(4)
Sr-O (x2)	2.587(5)
Sr-O (x2)	2.762(5)
Sr-O (x2)	2.487(4)
Sr-O (x2)	2.642(4)
O-Pt-O (x6)	85.71(18)
O-Pt-O (x6)	94.29(18)
O-Pt-O(x3)	180.0

Conclusions:

A family of one-dimensional oxides Sr_3MPtO_6, where M = Co, Ni, Cu, and Zn, has been synthesized and structurally and magnetically characterized. The one-dimensional chains in these materials consists of alternating face-shared MO_6 trigonal prisms and PtO_6 octahedra. In substituting the M site with Zn to Co, it was possible to add electrons to the chains in a controlled manner. These selective substitutions made it possible to study the composition-magnetic property relationships of this family of one-dimensional oxides. It is interesting to note that while the magnetic materials were all antiferromagnets, their individual characteristics were distinct.

References

(1) Rouxel, J. *Crystal chemistry and properties of materials with quasi-one-dimensional structures*; D. Reidel Publishing Co.: Boston, 1986; Vol. 2.

(2) Gadet, V.; Verdaguer, M.; Briois, V.; Gleizes, A.; Renard, J. P.; Beauvillain, P.; Chappert, C.; Goto, T.; Le Dang, K.; Veillet, P. *Phys. Rev. B* **1991**, *44*, 705.

(3) Haldane, F. D. M. *Phys. Lett. A* **1983**, *93*, 463.

(4) Haldane, F. D. M. *Phys. Rev. Lett.* **1983**, *50*, 1153.

(5) des Cloiseaux, J.; Pearson, J. J. *Phys. Rev.* **1962**, *128*, 2131.

(6) Renard, J. P.; Verdaguer, M.; Regnault, L. P.; Erkelens, W. A. C.; Rossat-Mignod, J.; Ribas, J.; Stirling, W. G.; Vettier, C. *J. Appl. Phys.* **1988**, *63*, 3538.

(7) Darriet, J.; Regnault, L. P. *Solid State Comm.* **1993**, *86*, 409.

(8) Wilkinson, A. P.; Cheetham, A. K.; Kunnman, W.; Kvick, A. *Eur. J. Solid State Inorg. Chem.* **1991**, *28*, 453.

(9) Larson, A. C.; vonDreele, R. B. In Los Alamos National Laboratory: Los Alamos, NM, 1990; pp .

(10) Randall, J. J.; Katz, L. *Acta Cryst.* **1959**, *12*, 519.

(11) Wilkinson, A. P.; Cheetham, A. K. *Acta Cryst.* **1989**, *C45*, 1672.

(12) Carlin, R. L. *Magnetochemistry*; Springer-Verlag: Berlin, 1986.

(13) Bonner, J. C.; Fisher, M. E. *Phys. Rev.* **1964**, *135*, 640.

(14) WaveMetrics, I. In Lake Oswego, OR, 1991; pp .

(15) Hatfield, W. E. *J. Appl. Phys.* **1981**, *52*, 1985.

(16) Hodeau, J. L.; Tu, H. Y.; Bordet, P.; Fournier, T.; Strobel, P.; Marezio, M.; Chandrashekhar, G. V. *Acta Cryst.* **1992**, *B48*, 1.

(17) Bostanov, V. *J. Crystal Growth* **1977**, *42*, 194.

(18) Zubeck, I. V.; Feigelson, R. S.; Huggins, R. A.; Pettit, P. A. *J. Crystal Growth* **1976**, *34*, 85.

(19) Elwell, D.; DeMattei, R. C.; Zubeck, I. V.; Feigelson, R. S.; Huggins, R. A. *J. Crystal Growth* **1976**, *33*, 232.

(20) de Jongh, L. J.; Miedema, A. R. *Adv. Phys.* **1974**, *23*, 1.

(21) Carlin, R. L. *J. Chem. Educ.* **1991**, *68*, 361.

(22) Greaney, M. A.; Ramanujachary, K. V.; Teweldemedhin, Z.; Greenblatt, M. *J. Solid State Chem.* **1993**, *107*, 554.

(23) Figgis, B. N. *Introduction to Ligand Fields*; Interscience Publishers: New York, 1966.

(24) Renard, J. P.; Clement, S.; Verdaguer, M. *Proc. Indian Acad. Sci. (Chem. Sci.)* **1987**, *98*, 131.

(25) Ajiro, Y.; Goto, T.; Kikuchi, H.; Sakakibara, T.; Inami, T. *Phys. Rev. Lett.* **1989**, *63*, 1424.

(26) Schwartz, K. B., and Prewitt, C.T. *J. Phys. Chem. Solids* **1984**, *45*, 1-21.

(27) Shriver, D.F., Atkins, P.W., and Langford, C.H. *Inorganic Chemistry*; W.H. Freeman and Company: New York, 1990.

(28) Gallagher, P. K., Johnson, D.W. Jr., Vogel, E.M., Wertheim, G.K., and Schnettler, F.J. *J. Solid State Chem* **1977**, *21*, 277-282.

(29) Kim, K. S., Winograd, N., and Davis, R.E. *JACS* **1971**, *93*, 6296-6297.

(30) Furusaki, A.; Sigrist, M.; Lee, P. A.; Tanaka, K.; Nagaosa, N. *to be published.*

Chapter 4

Structural and Magnetic Characterization of the One-Dimensional Oxides, Sr_3MIrO_6 where M = Ni, Cu, and Zn

Chapter 4

The synthesis and magnetic characterization of the family of one-dimensional oxides Sr_3MIrO_6, where M = Ni, Cu, and Zn, is discussed in this chapter. Low dimensional materials with extended structures have long been of interests to chemists and physicists because they can possess unique magnetic and electronic properties. These properties arise from the high anisotropy present in these materials as a result of the strong directionality of the structures. Magnetic systems of low dimensionality are of particular interest because they can exhibit novel effects, such as the Haldane gap and random spin paramagnetism, that cannot be found in systems of higher dimensionality .

The magnetic materials discussed in this chapter are structural analogs of the platinum oxides described in the previous chapter. Exchanging diamagnetic platinum (IV), low spin octahedral, with low spin octahedral iridium (IV), d^5, places an element having one unpaired electron into the octahedral site. Instead of having alternating magnetic and diamagnetic centers as in the platinum oxides, the iridium compounds will have an octahedral site with one unpaired electron alternating with trigonal prismatic sites containing zero, one, or two unpaired electrons. Consequently, an investigation that systematically alters the number of unpaired electrons on the trigonal prismatic site of this family of bimetallic one-dimensional oxides containing iridium will provide insights into the effects that one added unpaired electron has on the magnetic properties of this system. The magnetic properties of the iridium-containing analogs are expected to be different and more complex than those of the platinum-containing systems because of the added interactions between the electrons on the trigonal prismatic M site and the single unpaired electron of the iridium.

Experimental:

General methods of synthesis and characterization are the same as that in Chapter 3. All materials were used as received: $SrCO_3$ (Cerac, 99.5%), Ir metal (Aesar, 99.9%,

or Engelhard), NiO (Cerac, 99.995%), CuO (Cerac, 99.999%), Co metal (Cerac, 99.8%), and ZnO (Aldrich, 99.9%). Materials were structurally characterized by powder X-ray diffraction methods on a Rigaku RU300 diffractometer or by neutron powder diffraction collected at the NIST nuclear facility at Gaithersburg, Maryland. Rietveld refinement of the powder diffraction data was performed using the refinement package GSAS.

Magnetic measurements were obtained using a Quantum Design MPMS SQUID magnetometer at temperatures ranging from 2 to 300 K. All samples were fully oxidized by annealing in O_2 at 550-750 °C before being used for any magnetic measurements. For data collection, all samples were cooled in zero field to 5 K. Once the sample temperature reached 5 K, the magnetic field was turned on and data were collected. All data were corrected for the diamagnetic contribution of the calibrated Kel-F sample container. High field magnetic studies were performed at the Francis Bitter National Magnet Laboratory.

Electrical conductivity measurements were performed on sintered pellets using a Janis Research Co., Inc. conductivity apparatus equipped with a Keithley Model 236 electrometer and a Lakeshore 333 temperature controller. Gold wires were attached to the samples with conducting silver paint. Currents used were typically between 1 μA and 1 nA.

All polycrystalline samples were prepared via solid state synthesis. Stoichiometric amounts of $SrCO_3$, Ir metal, and the appropriate first row transition metal oxide were intimately mixed under acetone using an agate mortar and pestle and pressed into pellets. The pellets were placed on platinum foil in alumina boats during heating to prevent aluminum contamination. Heating the samples at 1150 °C for 2 weeks with intermittent grindings yielded single phase materials.

Results and Discussion:

Sr_3ZnIrO_6: The structure was refined by Rietveld analysis of the powder X-ray diffraction data and found to be isostructural with Sr_3NiPtO_6, see Figure 4.1 and Table 4.1. Table 4.2 lists the atomic positions and their esd's as refined from X-ray diffraction data, and selected bond distances and angles are displayed in Table 4.3.

Sr_3ZnIrO_6 can be considered as an analog of Sr_3CuPtO_6 discussed in Chapter 3 but with the spin located in the octahedral site rather than the distorted trigonal prismatic site. In Sr_3CuPtO_6, there is one unpaired electron in the Cu(II) square planar site and no unpaired electron in the octahedral site occupied by the Pt(IV). Sr_3ZnIrO_6, on the other hand, contains no unpaired electron in the Zn(II), d^{10}, trigonal prismatic site, and the unpaired electron is now located in the octahedral site occupied by the Ir(IV), d^5.

One might expect that the magnetic properties of Sr_3ZnIrO_6 and Sr_3CuPtO_6 would be similar since they both have chains containing alternating spin one-half and spin zero. However, the site symmetry of the unpaired electron in Sr_3ZnIrO_6 is different from that in Sr_3CuPtO_6. Sr_3ZnIrO_6 has an unpaired electron on the Ir octahedral site, and Sr_3CuPtO_6 has the unpaired electron on the Cu square planar site. This difference in site symmetry is expected to lead to slightly different magnetic behavior. Indeed, magnetic studies of Sr_3ZnIrO_6 at 5 kG reveal an antiferromagnetic transition at ~20 K, shown in Figure 2, having a slightly different cusp shape than what was observed for Sr_3CuPtO_6. As with Sr_3CuPtO_6, it was attempted to fit the data to a linear chain Heisenberg model, but the fit was poor. The fit, also shown in Figure 4.2, predicted a broader transition and a lower susceptibility than what is actually observed.

A good fit, however, was obtained by modelling the data with the alternating chain Heisenberg model.[1-3] This model implies that the magnetic exchange between a magnetic ion and its nearest magnetic neighbor on one side is different than the magnetic exchange with its nearest neighbor on the other side. In other words, there are two

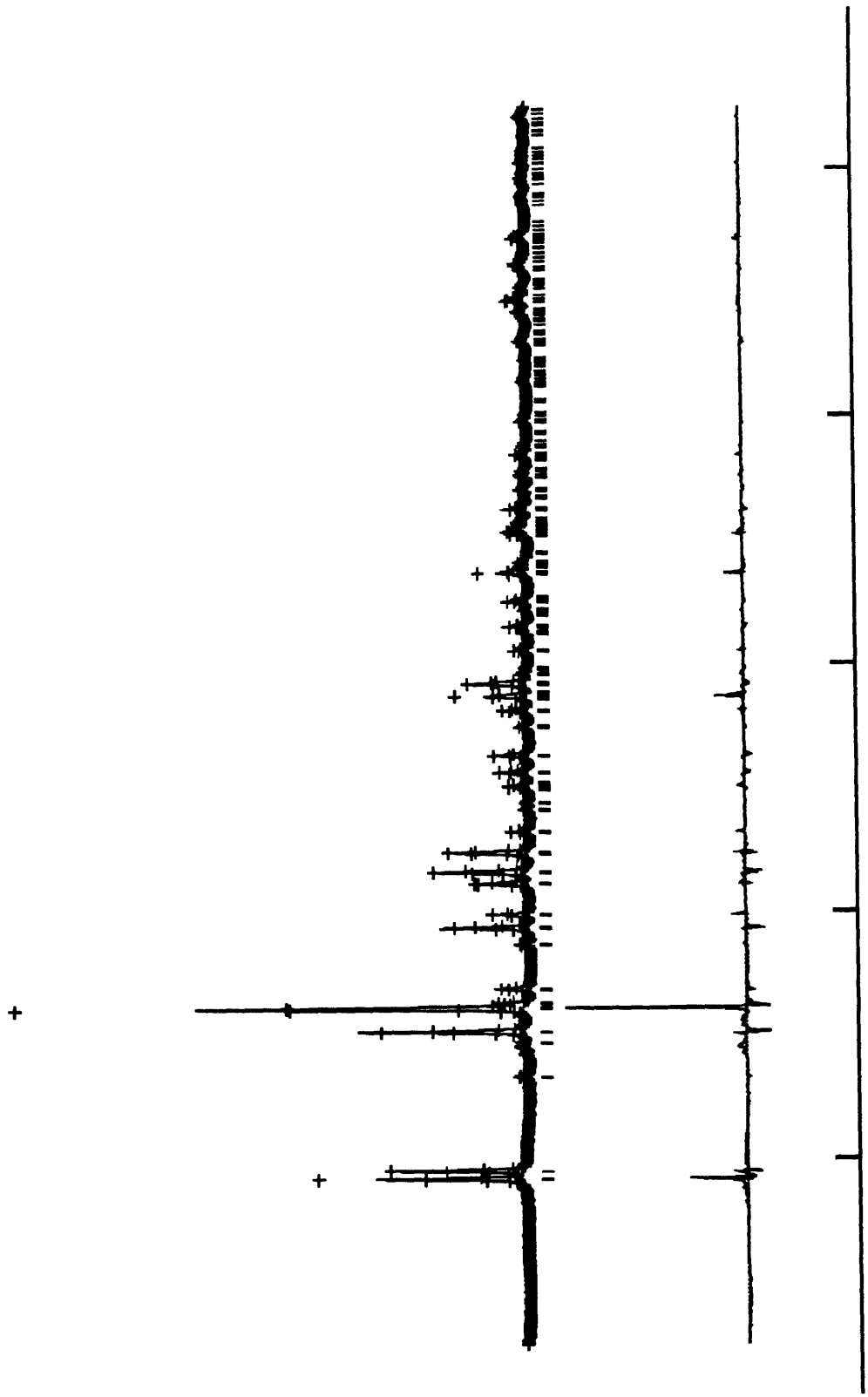

Figure 4.1. Rietveld analysis of the X-ray powder data for Sr_3ZnIrO_6 at 298 K showing the observed, calculated, and difference patterns.

Table 4.1: Crystallographic Data for Sr_3ZnIrO_6 at 298 K

Formula	Sr_3ZnIrO_6
Formula weight	616.47
Color	Black powder
Space group	$R\bar{3}c$ (#167)
a, Å	9.6327(4)
c, Å	11.2022(5)
V, Å^3	900.179
Z	6
D_{calc}, g/cm^3	6.822
λ, Å	Cu K_α, X-ray, 1.5405
2θ scan range (°)	5-105
Step interval (°2θ)	0.01
Maximum step intensity (counts)	40,000
Number of unique reflections	240
Number of structural parameters†	7
Number of background parameters	7
Number of profile parameters	5
Refinement	Rietveld using GSAS[a] with pseudo-Voigt[b] peak shape function
R_{wp}[c]	0.160
R_p[d]	0.126
GOF (R_{wp}/R_e)	4.4
χ^2	19.56

† Includes atomic positional and displacement parameters and unit-cell dimensions.

[a] General Structure Analysis System, LANSCE, Los Alamos National Laboratory.

[b] J. Appl. Cryst. **15**, 615-620, 1982.

[c] $R_{wp} = [\Sigma w(I_o-I_c)^2/\Sigma wI_o^2]$

[d] $R_p = \Sigma|I_o-I_c|/\Sigma I_o$, where I_o and I_c are the observed and calculated integrated intensities, respectively, and w is the weight derived from an error propagation scheme during the least square refinement process.

Table 4.2: Atomic Positions of Sr_3ZnIrO_6 from Refinement of X-ray Data

Atom	x	y	z
Sr	2/3	-0.0298(1)	0.5833(1)
Ir	1/3	-1/3	2/3
Zn	1/3	-1/3	0.4167(1)
O	0.3606(7)	-0.1626(6)	0.5525(4)

Table 4.3: Selected Bond Distances and Angles from Refinement of X-ray Data

Ir-O (x6)	1.994(5)
Ir-Zn (x2)	2.801(1)
Zn-O (x6)	2.158(5)
Sr-O (x2)	2.584(6)
Sr-O (x2)	2.797(6)
Sr-O (x2)	2.511(5)
Sr-O (x2)	2.704(5)
O-Ir-O (x6)	83.31(22)
O-Ir-O (x6)	96.70(22)
O-Ir-O(x3)	179.96(1)

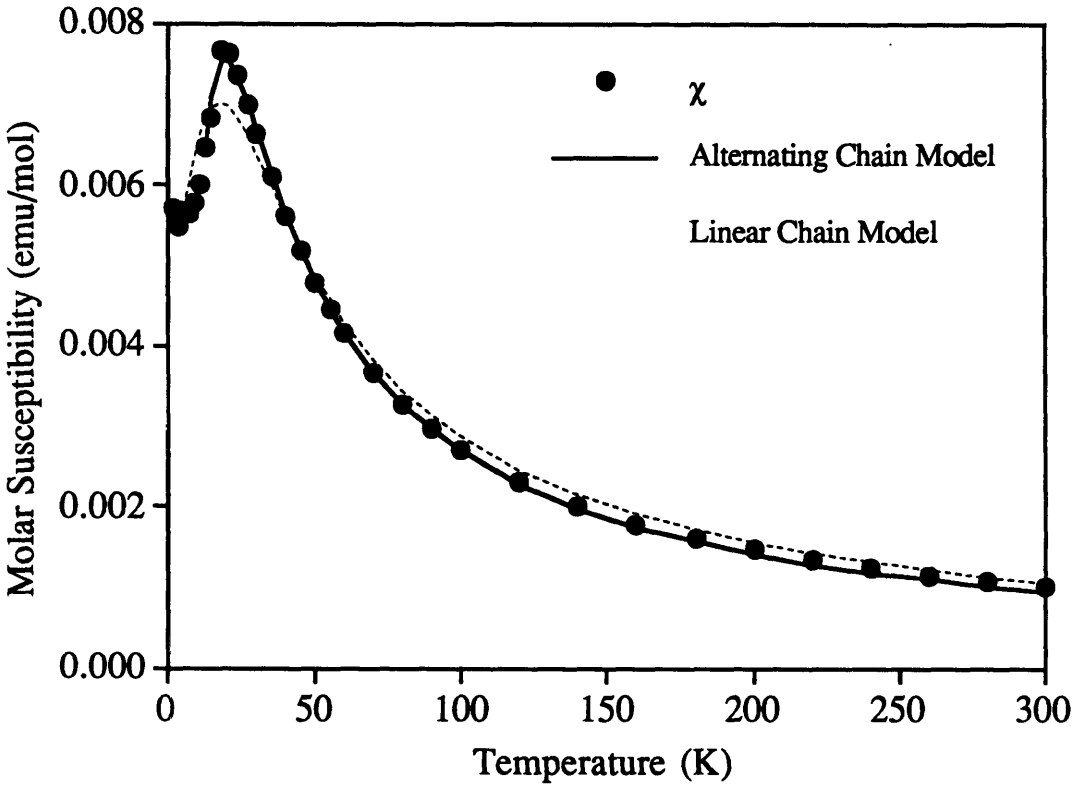

Figure 4.2. Magnetic susceptibility of Sr_3ZnIrO_6 at 5 kG and best fits to the Heisenberg linear chain model and the alternating chain model.

exchange constants, and they alternate along the chain. The linear chain Heisenberg model has the following Hamiltonian:

$$H = -2J \sum_{i=1}^{n} [\hat{S}_i^{x,y,z} \bullet \hat{S}_{i+1}^{x,y,z}]$$

The linear chain model is an isotropic model which states that the exchange between spins are all equivalent. In the alternating chain model, a second exchange constant is generated by introducing a new variable called the alternation parameter, α, where $0 \leq \alpha \leq 1$. Thus, the Hamiltonian becomes:

$$H = -2J \sum_{i=1}^{n/2} [\hat{S}_{2i} \bullet \hat{S}_{2i-1} + \alpha \hat{S}_{2i} \bullet \hat{S}_{2i+1}]$$

and the couplings along the chain can be viewed as:

$$\underset{M}{} \overset{J}{\text{-------}} \underset{M}{} \overset{\alpha J}{\text{----------}} \underset{M}{} \overset{J}{\text{-------}} \underset{M}{} \overset{\alpha J}{\text{----------}} \underset{M}{} \overset{J}{\text{-------}} \underset{M}{}$$

Scheme 4.1

When $\alpha = 1$, the model reduces to the linear chain model, and when $\alpha = 0$, the chain can be viewed as a series on dimers. The equation used to fit the data shown in Table 4.4 was obtained from Hatfield.[4,5] A least-square best fit gave J/k = -15.6 K, g = 1.79, and α = 0.11. The small α value indicates that Sr_3ZnIrO_6 behaves magnetically more like a dimer than a linear chain. Since the model suggests that there are inequivalent magnetic exchanges, the distances between magnetic ions should also reflect this difference, i.e., the bond lengths should also alternate. We do not see any evidence of alternating bond distances in our room temperature X-ray diffraction studies, and, in fact, the refined structure has only one zinc and one iridium site which forces the bond lengths to be the same. However, this fact does not eliminate the alternating chain model as a description for the magnetic behavior Sr_3ZnIrO_6 at ~20 K. Other materials with uniform distances between magnetic ions at room temperatures have been shown by dielectric

Table 4.4. Equation for fitting to the alternating chain Heisenberg model.[4]

$$\chi_m = \frac{N g^2 \mu_B^2}{kT} \bullet \frac{A + Bx + Cx^2}{1 + Dx + Ex^2 + Fx^3}, x = |J|/kT$$

χ_m = molar susceptibility, N = Avogadro's number, g = powder-averaged g-value, μ_B = Bohr magneton, k = Boltzman's constant, and J = exchange constant,

For $0 \leq \alpha \leq 0.4$:

$A = 0.25$

$B = -0.12587 + 0.22752\alpha$

$C = 0.019111 - 0.13307\alpha + 0.50967\alpha^2 - 1.3167\alpha^3 + 1.0081\alpha^4$

$D = 0.10772 + 1.4192\alpha$

$E = -0.0028521 - 0.42346\alpha + 2.1953\alpha^2 - 0.82412\alpha^3$

$F = 0.37754 - 0.067022\alpha + 5.9805\alpha^2 - 21.678\alpha^3 + 15.838\alpha^4$

For $0.4 < \alpha \leq 1.0$

$A = 0.25$

$B = -0.13695 + 0.26387\alpha$

$C = 0.017025 - 0.12668\alpha + 0.49113\alpha^2 - 1.1977\alpha^3 + 0.87257\alpha^4$

$D = 0.070509 + 1.3042\alpha$

$E = -0.0035767 - 0.40837\alpha + 3.4862\alpha^2 - 0.73888\alpha^3$

$F = 0.36184 - 0.065528\alpha + 6.65875\alpha^2 - 20.945\alpha^3 + 15.425\alpha^4$

** The equation and sets of parameters are valid only for $kT/|J| \geq 0.5$ and $J \leq 0$.

measurements to undergo phase transitions at lower temperatures.[4,5] These materials dimerize at lower temperatures and the resulting phase transitions appear as anomalous peaks in capacitance measurements. Also, our X-ray diffraction data may not be sensitive enough to detect possible oxygen position changes, and more sensitive methods such as low temperature neutron diffraction may be necessary to detect any structural deviations.

Sr_3CuIrO_6: Both Sr_3CuIrO_6 and Ca_3CuIrO_6 have been structurally characterized by single crystal diffraction.[6,7] Small single crystals of Sr_3CuIrO_6 and Ca_3CuIrO_6 were obtained by slow cooling the mixture of starting materials and by slow cooling in a CaF_2/KF flux, respectively. Sr_3CuIrO_6 can also be prepared by a solid state reaction of the simple oxides and iridium metal. Ca_3CuIrO_6, however, cannot be synthesized in such a manner. These materials are isostructural with Sr_3CuPtO_6, containing alternating, edge-shared copper oxygen square planes and iridium oxygen octahedra. By substituting Pt(IV) with Ir(IV), however, an unpaired electron is introduced into the octahedral site to produce a chain with spin 1/2 on two distinct sites.

The magnetic susceptibility data of Sr_3CuIrO_6 reveal a large sharp increase at ~40 K indicative of ferromagnetic ordering, Figure 4.3. Ferromagnetic ordering is also supported by the χT plot shown in the same figure. The effective moment is levelled before the transition and rises sharply upon reaching the ordering temperature. The moment then decreases at ~15 K, because of magnetic saturation. Magnetic ordering can also be seen in the electrical conductivity measurements performed on a sintered pellet of Sr_3CuIrO_6, Figure 4.4. At high temperatures, the non-interacting electrons are delocalized, and the conductivity is essentially constant, decreasing only slightly upon cooling. Upon reaching the ordering temperature, however, the conductivity decreases by approximately a factor of 4, indicating magnetic ordering and localization of the electrons.

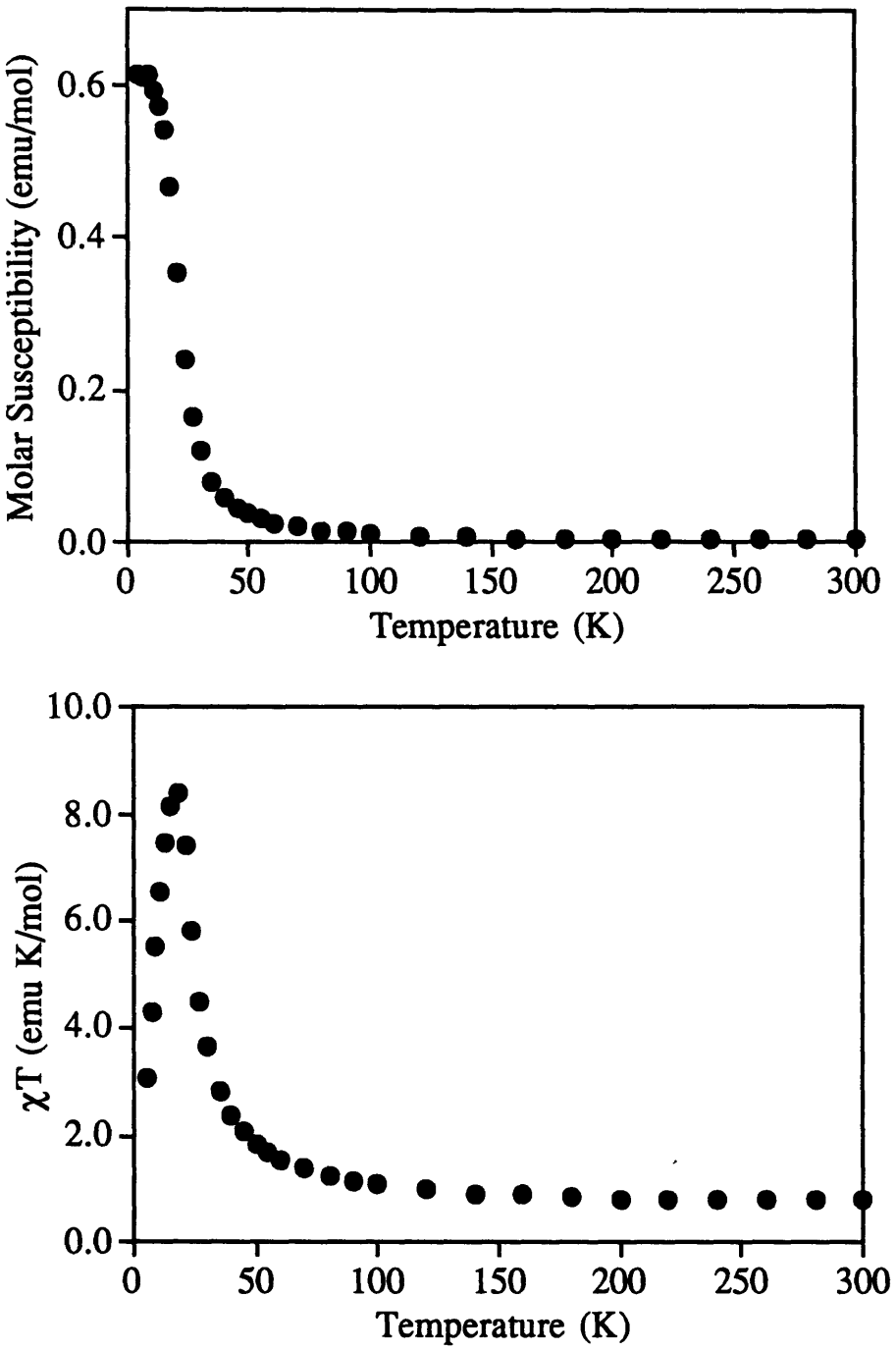

Figure 4.3. Top, magnetic susceptibility and, bottom, effective magnetic moment of Sr_3CuIrO_6 at 5 kG. The χT curve indicates that the sudden increase in susceptibility at ~50 K is a ferromagnetic transition.

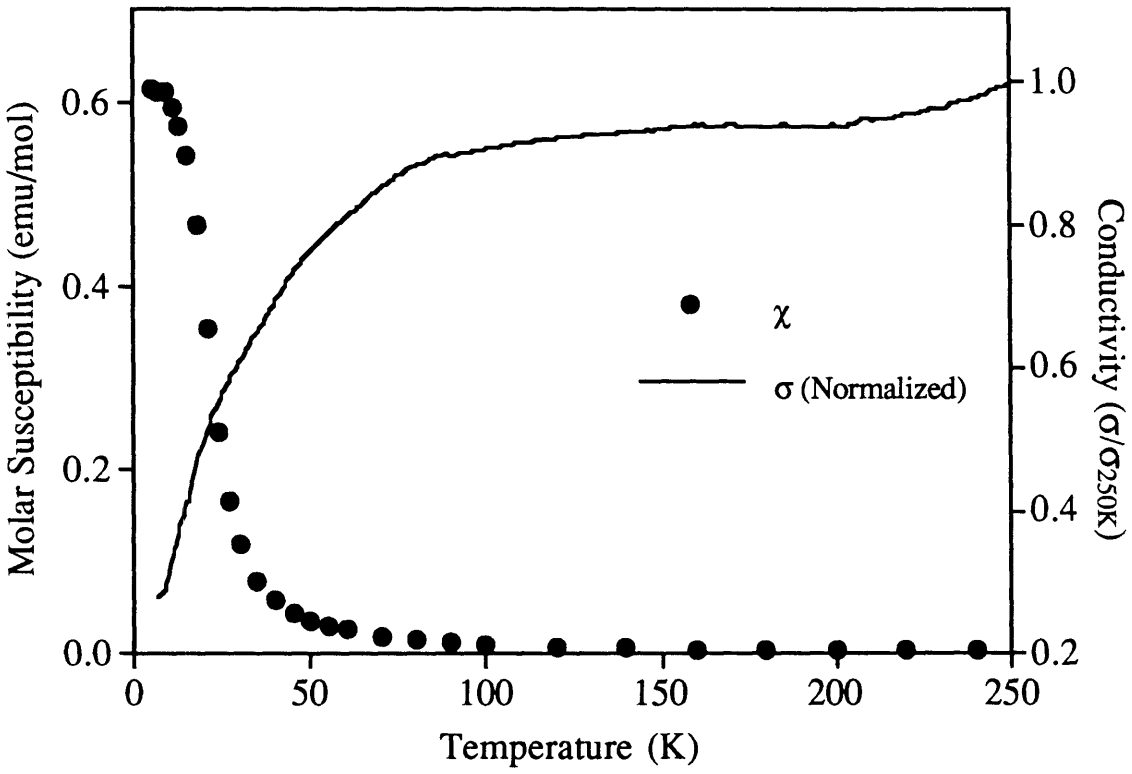

Figure 4.4. Electrical conductivity of Sr_3CuIrO_6 as a function of temperature. The sample becomes less conducting at the ferromagnetic-ordering temperature, ~50 K.

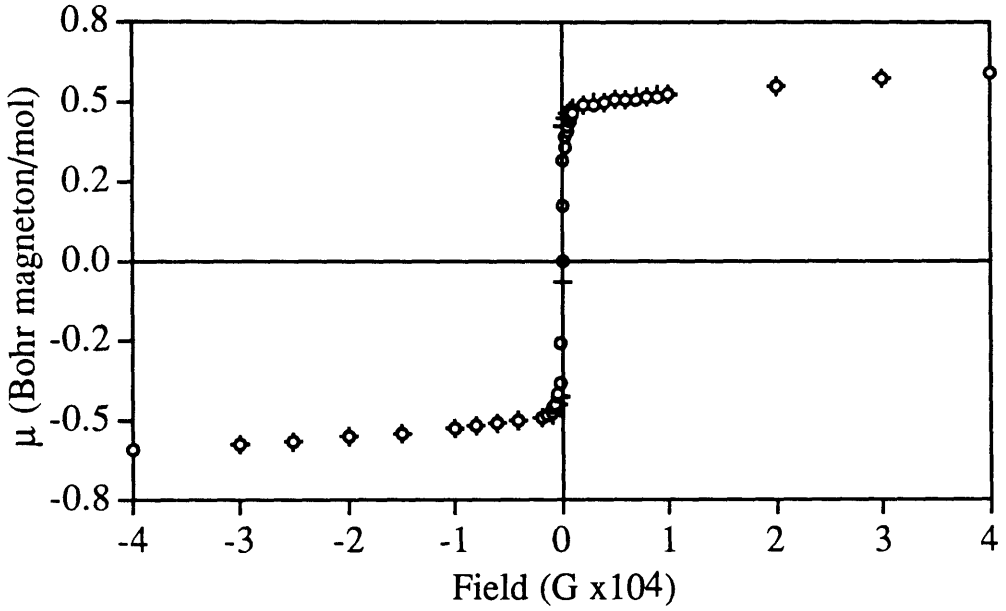

Figure 4.5A. Field dependence of Sr_3CuIrO_6 at 5 K. Sr_3CuIrO_6 is a soft ferromagnet with a saturation magnetization of ~ 0.7 μ_B.

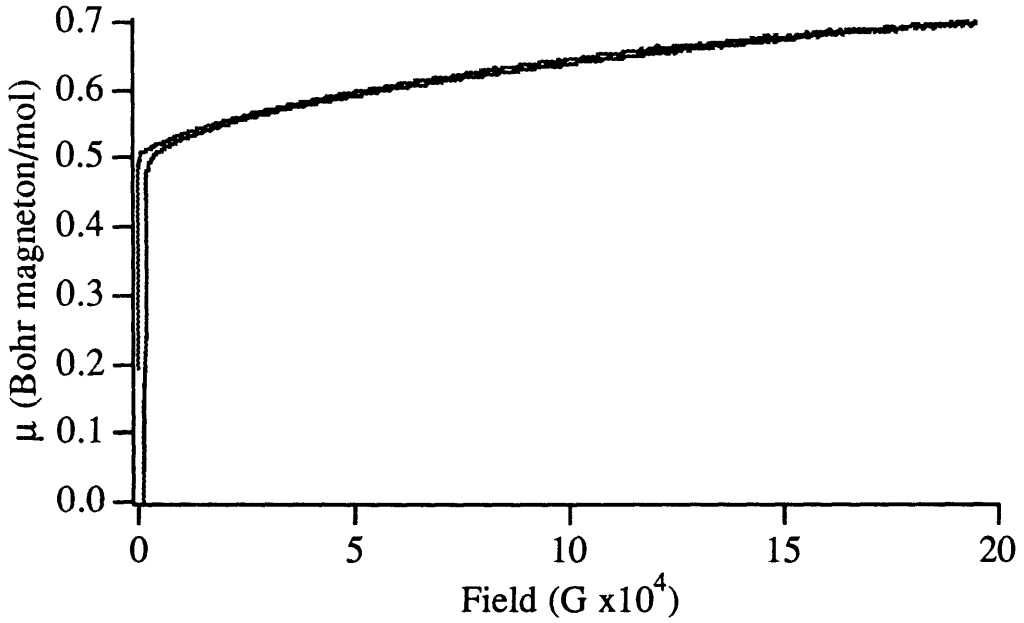

Figure 4.5B. High field dependence of Sr_3CuIrO_6 at 4.5 K.

To understand the magnetism of this material better, magnetic field dependence studies were performed. Figure 4.5A shows the field dependence of Sr_3CuIrO_6 at 5 K for positive and negative field up to 4 Tesla. The magnetization loop is typical of ferromagnets, and the lack of significant hysteresis suggests that Sr_3CuIrO_6 is a very soft ferromagnet, one that is easily magnetized and demagnetized. The experimentally calculated saturation magnetization is 0.61 Bohr magneton per mole. One would expect a saturation magnetization of 2 μ_B for a system containing two unpaired electrons. Often an experimental saturation magnetization that is lower than expected can be explained by invoking ferrimagnetism or canted antiferromagnetization, schematically shown in Figure 4.6. In the case of ferrimagnetism, there are two sets of opposing, parallel spins with unequal magnitudes. The net result is a set of parallel spins with reduced magnitudes. The ferrimagnetic model, however, is unlikely in the case of Sr_3CuIrO_6 since both copper and iridium have one unpaired electron each. In the case of a canted antiferromagnet, the spins are of equal magnitude, but they are not perfectly opposed as they would be in an ideal antiferromagnet. The net result is again a set of parallel spins with smaller magnitudes. This model, however, implies spin anisotropy, since the magnetic moments are not parallel.

Another model that can rationalize the experimental saturation magnetization is simple ferromagnetism that is not clearly manifested in the magnetic results. The observed saturation magnetization is 0.61 μ_B, or approximately one-third the expected saturation magnetization of 2 μ_B. Since the magnetic moment was measured on powder samples, the observed magnetization is the true magnetization averaged over the three crystallographic axes. Since the grains of material are randomly distributed, if two spin axes were statistically "locked in" space and unable to move and align with the applied field, then only one-third of the total magnetization would be observed. To verify this spin arrangement, it was attempted to align the spins physically by applying a very large external field, up to 20 Tesla. As shown in Figure 4.5B, up to 20 Tesla the saturation

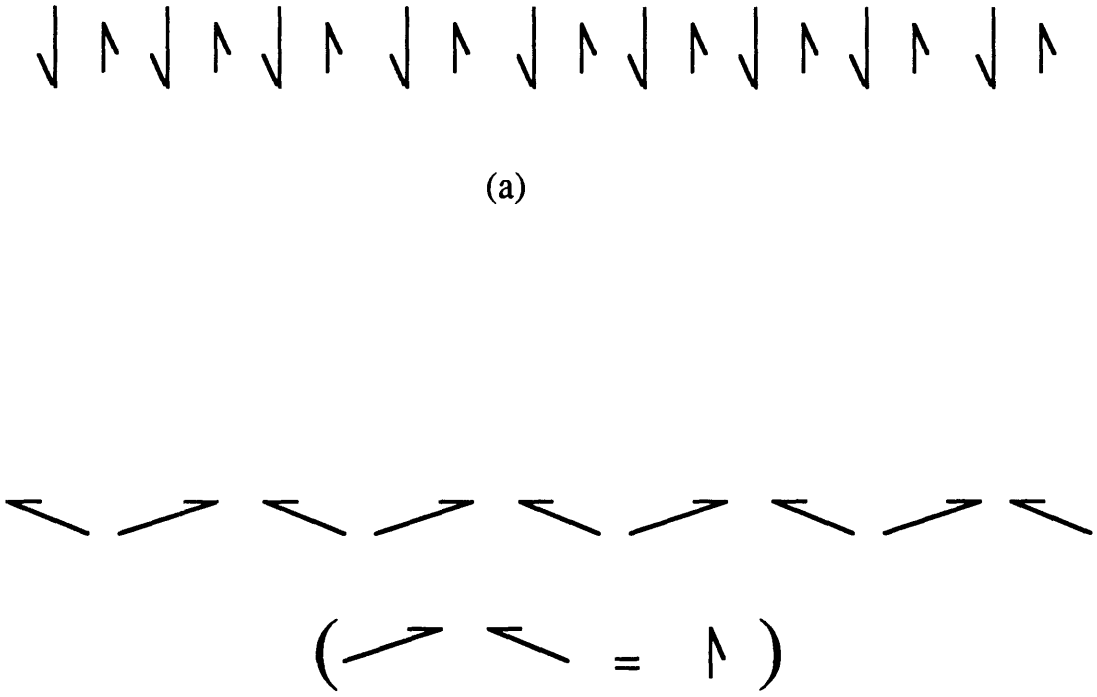

Figure 4.6. (a) Spin arrangement for a one-dimensional ferrimagnet. (b) Spin arrangement for a one-dimensional canted antiferromagnet.

magnetization does not change appreciably from the low field results. To confirm this ferromagnetic magnetic model, single crystal anisotropic magnetic measurements are needed. If this model is correct, a saturation magnetization of 2 μ_B will be observed in one crystallographic direction and and no moment will be observed in the two perpendicular directions. Single crystal growth is in progress.

Sr_3NiIrO_6: Sr_3NiIrO_6 displays the most complex magnetic behavior of all the platinum and iridium oxides in this series of one-dimensional compounds. The structure was determined by Rietveld analysis of the powder neutron diffraction data (Figure 4.7 and Table 4.5) and found to be isostructural with the platinum analog, Sr_3NiPtO_6. Table 4.6 lists the atomic positions and their esd's, and selected bond distances and angles are displayed in Table 4.7. The chains in Sr_3NiIrO_6 contain alternating Ni(II) with two unpaired electrons and Ir(IV) with one unpaired electron. As expected, the magnetic behavior of this material is perhaps the most unusual of all the analogs.

The magnetic susceptibilities of Sr_3NiIrO_6 at 3, 10 and 40 kG are shown in Figure 4.8. There is a large increase in the susceptibility starting at ~120 K, reaching a maximum susceptibility at $T_{max} \approx 21$ K. At temperatures below T_{max}, there is a precipitous drop in the magnetization to a constant singlet ground state. The susceptibility curves are characteristic of an antiferromagnetic transition, and the decrease in susceptibilities at higher fields is indicative of spin saturation, also consistent with antiferromagnetism. Typically, however, the powder susceptibility of an antiferromagnet will converge to a value of two-thirds χ_{max}, the maximum susceptibility, after the ordering temperature.[8] The magnetic properties of Sr_3NiIrO_6 might be explained by a structural transition such as dimerization of the magnetic nuclei within the chains. To test this possibility, low temperature neutron studies were performed at 10 and 30 K, in the singlet state region and the ordering region, respectively. The results are shown in Figures 4.9 and 4.10 and Tables 4.8 and 4.9. With the exception of the expected contractions in unit cell at lower temperatures, no new magnetic diffraction peaks

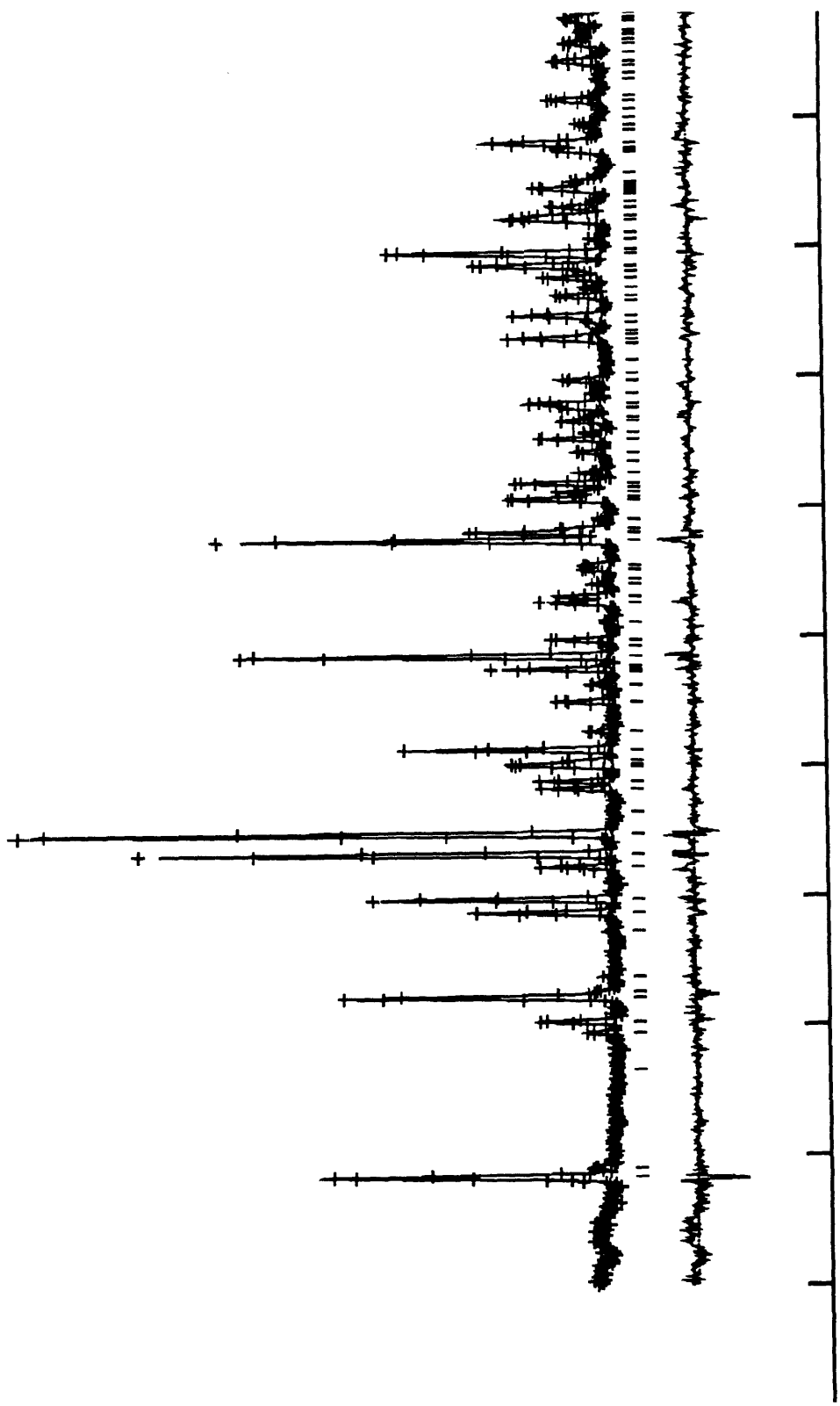

Figure 4.7. Rietveld analysis of the neutron powder data for Sr_3NiIrO_6 at 298 K showing the observed, calculated, and difference patterns.

Table 4.5: Crystallographic Data for Sr_3NiIrO_6 at 298K

Formula	Sr_3NiIrO_6
Formula weight	609.78
Color	Black powder
Space group	$R\bar{3}c$ (#167)
a, Å	9.6042(3)
c, Å	11.1587(4)
V, $Å^3$	891.383
Z	6
D_{calc}, g/cm^3	6.815
λ, Å	neutron, 1.5390
2θ scan range (°)	10-120
Step interval (°2θ)	0.05
Maximum step intensity (counts)	2,500
Number of unique reflections	154
Number of structural parameters†	7
Number of background parameters	8
Number of profile parameters	6
Refinement	Rietveld using GSAS[a] with pseudo-Voigt[b] peak shape function
R_{wp}[c]	0.065
R_p[d]	0.053
GOF (R_{wp}/R_e)	1.18
χ^2	1.41

† Includes atomic positional and displacement parameters and unit-cell dimensions.

[a] General Structure Analysis System, LANSCE, Los Alamos National Laboratory.

[b] J. Appl. Cryst. **15**, 615-620, 1982.

[c] $R_{wp} = [\Sigma w(I_o-I_c)^2/\Sigma wI_o^2]$

[d] $R_p = \Sigma|I_o-I_c|/\Sigma I_o$, where I_o and I_c are the observed and calculated integrated intensities, respectively, and w is the weight derived from an error propagation scheme during the least square refinement process.

Table 4.6: Atomic Positions of Sr_3NiIrO_6 from Refinement of Neutron Data

Atom	x	y	z
Sr	2/3	-0.0303(2)	0.5833(1)
Ir	1/3	-1/3	2/3
Ni	1/3	-1/3	0.4167(1)
O	0.3559(2)	-0.1604(2)	0.5531(1)

Table 4.7: Selected Bond Distances and Angles from Refinement of Neutron Data

Ir-O (x6)	2.013(1)
Ir-Ni (x2)	2.790(9)
Ni-O (x6)	2.182(1)
Sr-O (x2)	2.618(2)
Sr-O (x2)	2.737(5)
Sr-O (x2)	2.473(2)
Sr-O (x2)	2.682(1)
O-Ir-O (x6)	84.56(6)
O-Ir-O (x6)	95.44(6)
O-Ir-O(x3)	180.0

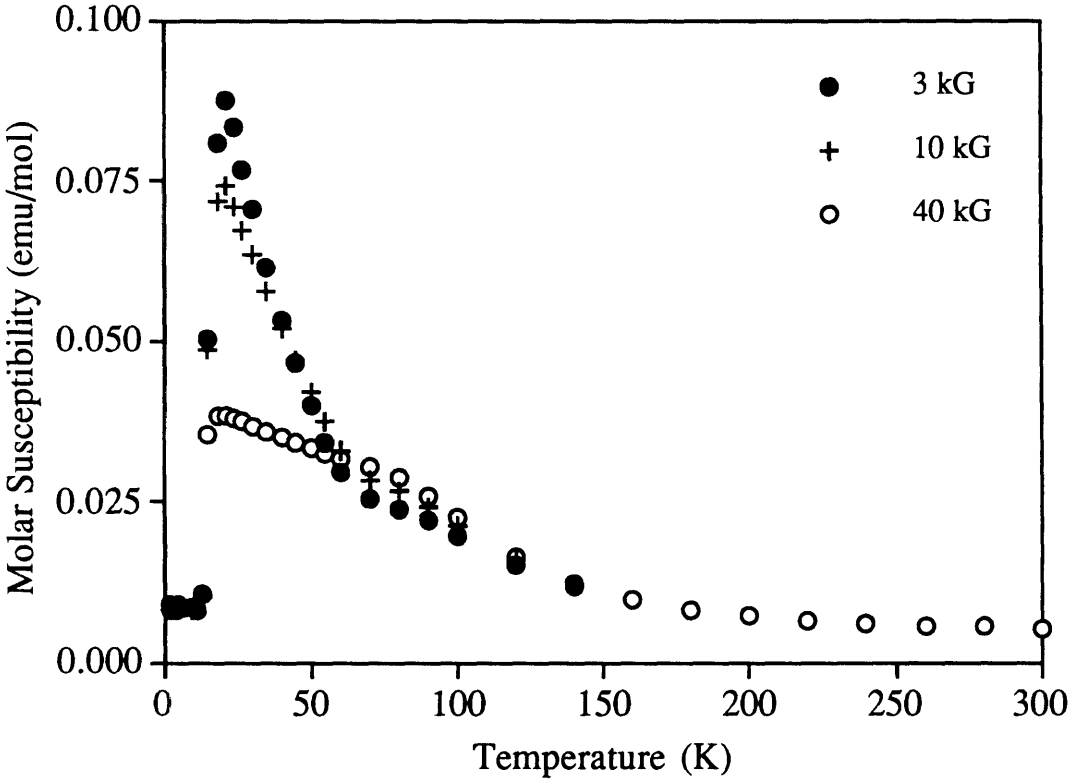

Figure 4.8. Magnetic susceptibilities of Sr_3NiIrO_6 at 3, 10 and 40 kG.

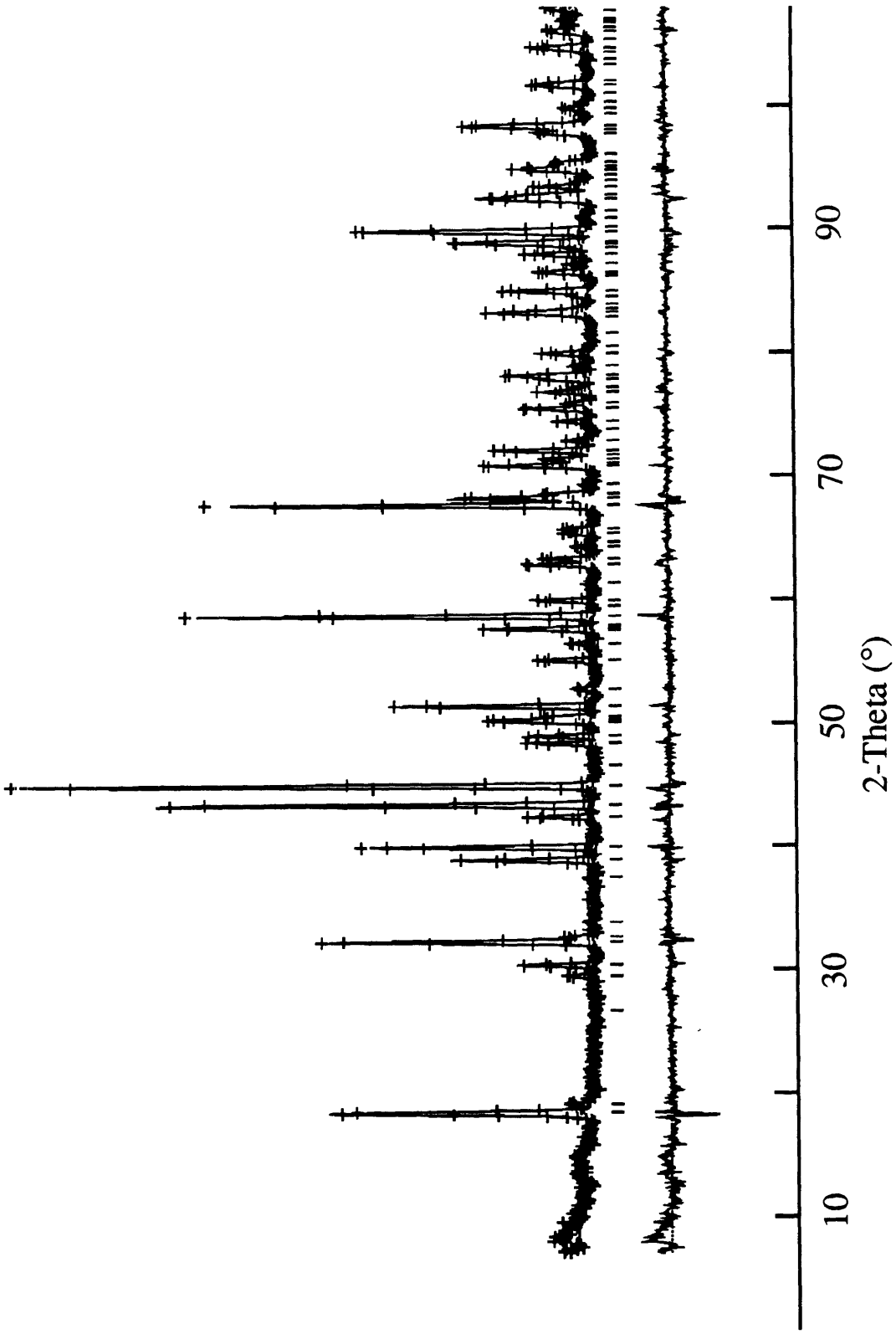

Figure 4.9. Rietveld analysis of the neutron powder data for Sr_3NiIrO_6 at 10 K showing the observed, calculated, and difference patterns.

Table 4.8: Crystallographic Data for Sr_3NiIrO_6 at 10K

Formula	Sr_3NiIrO_6
Formula weight	609.78
Color	Black powder
Space group	$R\bar{3}c$ (#167)
a, Å	9.5793(3)
c, Å	11.1330(3)
V, $Å^3$	884.731
Z	6
D_{calc}, g/cm^3	6.866
λ, Å	neutron, 1.5390
2θ scan range (°)	7-120
Step interval (°2θ)	0.05
Maximum step intensity (counts)	2,600
Number of unique reflections	154
Number of structural parameters†	7
Number of background parameters	8
Number of profile parameters	6
Refinement	Rietveld using GSAS[a] with pseudo-Voigt[b] peak shape function
R_{wp}[c]	0.069
R_p[d]	0.057
GOF (R_{wp}/R_e)	1.25
χ^2	1.59

† Includes atomic positional and displacement parameters and unit-cell dimensions.

[a] General Structure Analysis System, LANSCE, Los Alamos National Laboratory.

[b] J. Appl. Cryst. **15**, 615-620, 1982.

[c] $R_{wp} = [\Sigma w(I_o-I_c)^2/\Sigma w I_o^2]$

[d] $R_p = \Sigma|I_o-I_c|/\Sigma I_o$, where I_o and I_c are the observed and calculated integrated intensities, respectively, and w is the weight derived from an error propagation scheme during the least square refinement process.

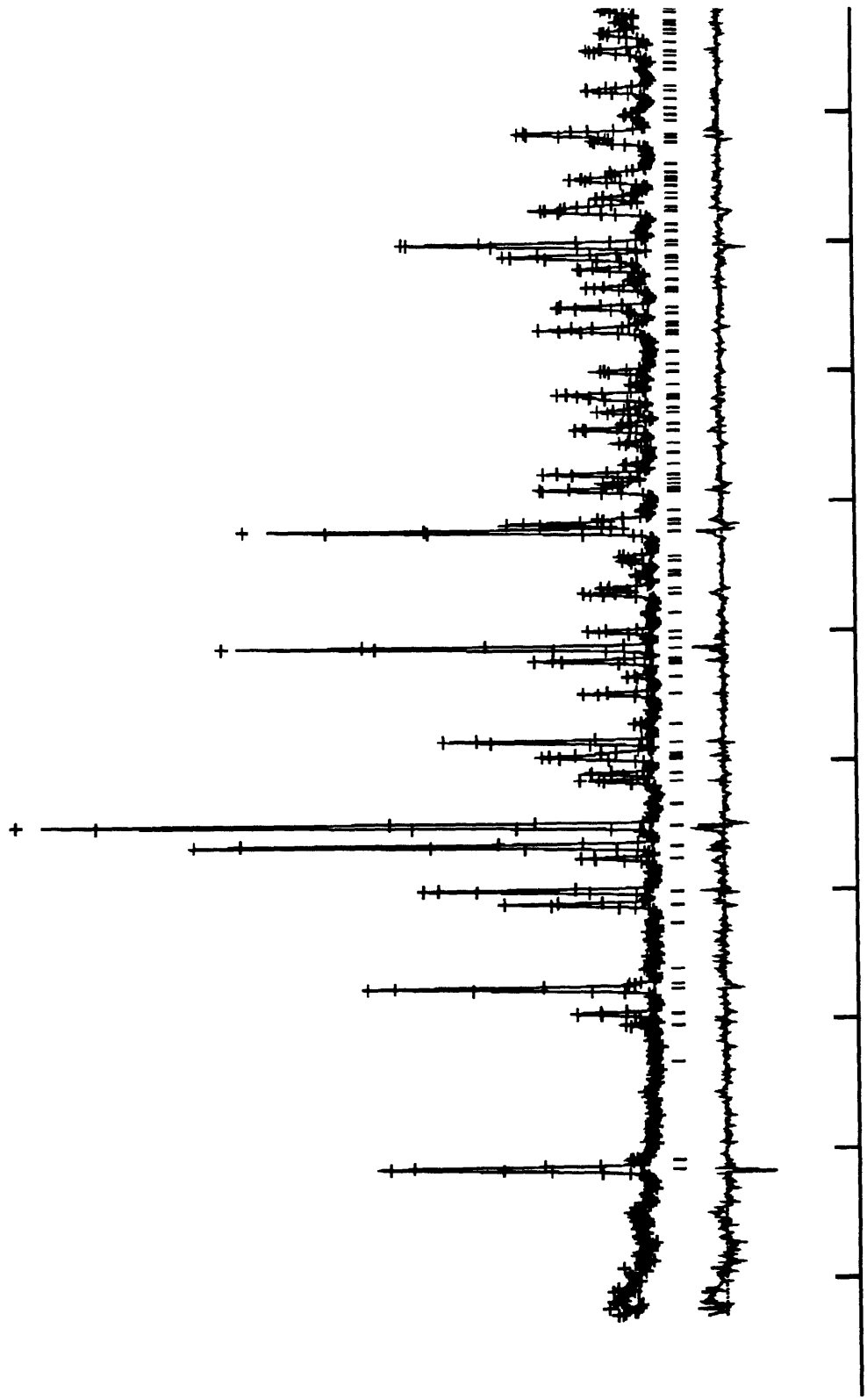

Figure 4.10. Rietveld analysis of the neutron powder data for Sr_3NiIrO_6 at 30 K showing the observed, calculated, and difference patterns.

Table 4.9: Crystallographic Data for Sr_3NiIrO_6 at 30 K

Formula	Sr_3NiIrO_6
Formula weight	609.78
Color	Black powder
Space group	$R\bar{3}c$ (#167)
a, Å	9.5794(3)
c, Å	11.1337(3)
V, Å^3	884.707
Z	6
D_{calc}, g/cm^3	6.865
λ, Å	neutron, 1.5390
2θ scan range (°)	7-120
Step interval (°2θ)	0.05
Maximum step intensity (counts)	2,600
Number of unique reflections	153
Number of structural parameters†	7
Number of background parameters	8
Number of profile parameters	6
Refinement	Rietveld using GSAS[a] with pseudo-Voigt[b] peak shape function
R_{wp}[c]	0.068
R_p[d]	0.057
GOF (R_{wp}/R_e)	1.23
χ^2	1.53

† Includes atomic positional and displacement parameters and unit-cell dimensions.

[a] General Structure Analysis System, LANSCE, Los Alamos National Laboratory.

[b] J. Appl. Cryst. **15**, 615-620, 1982.

[c] $R_{wp} = [\Sigma w(I_o-I_c)^2/\Sigma wI_o^2]$

[d] $R_p = \Sigma|I_o-I_c|/\Sigma I_o$, where I_o and I_c are the observed and calculated integrated intensities, respectively, and w is the weight derived from an error propagation scheme during the least square refinement process.

Table 4.10: Atomic Positions of Sr_3NiIrO_6 from Refinement of Neutron Data at 10 K

Atom	x	y	z
Sr	2/3	-0.0308(2)	0.5833(1)
Ir	1/3	-1/3	2/3
Ni	1/3	-1/3	0.4167(1)
O	0.3565(2)	-0.1599(2)	0.5529(1)

Table 4.11: Selected Bond Distances and Angles from Refinement of Neutron Data at 10 K

Ir-O (x6)	2.011(1)
Ir-Ni (x2)	2.783(8)
Ni-O (x6)	2.177(1)
Sr-O (x2)	2.607(1)
Sr-O (x2)	2.730(2)
Sr-O (x2)	2.469(2)
Sr-O (x2)	2.656(1)
O-Ir-O (x6)	84.55(6)
O-Ir-O (x6)	95.45(6)
O-Ir-O(x3)	180.0

Table 4.12: Atomic Positions of Sr_3NiIrO_6 from Refinement of Neutron Data at 30 K

Atom	x	y	z
Sr	2/3	-0.0306(2)	0.5833(1)
Ir	1/3	-1/3	2/3
Ni	1/3	-1/3	0.4167(1)
O	0.3563(2)	-0.1599(2)	0.5528(1)

Table 4.13: Selected Bond Distances and Angles from Refinement of Neutron Data at 30 K

Ir-O (x6)	2.012(1)
Ir-Ni (x2)	2.783(8)
Ni-O (x6)	2.177(1)
Sr-O (x2)	2.608(1)
Sr-O (x2)	2.730(2)
Sr-O (x2)	2.465(2)
Sr-O (x2)	2.657(1)
O-Ir-O (x6)	84.55(6)
O-Ir-O (x6)	95.45(6)
O-Ir-O(x3)	180.0

or structural changes were observed in the low temperature studies. The atomic positions and their esd's are listed in Table 4.10 and 4.11, and selected bond distances and angles are displayed in Table 4.12 and 4.13. Based on the neutron results, no structural transition has occurred at low temperatures. The magnetic transition might also be due to an electronic transition such as a metal-insulator transition. Electrical conductivity measurements were performed on a sintered pellet to test this hypothesis. Cooling from room temperature to approximately 100 K, the resistance increased to a magnitude of giga-ohms, the highest resistance measureable with the conductivity apparatus. No further measurements could be done reliably. Nevertheless, the sample was cooled to ~5 K to see if an electronic transition had occurred. The resistance at 5 K was still in the giga-ohm regime, eliminating the possibility of a metal-insulator transition.

As with the other materials discussed, it is useful to plot the effective moment, χT, as a function of temperature to see how the spins are pairing. As shown in the Figure 4.11, there are two peaks in the effective moment at ~90 K and ~35 K followed by a sharp decrease in moment which then converges to zero. The two peaks indicate ferromagnetic interactions, while the decrease in moment indicates antiferromagnetic coupling. A possible explanation that describes the magnetic results is ferromagnetic exchange within the chains and antiferromagnetic exchange between the chains. At 90 K, the spins of Ni and Ir are aligning ferromagnetically within the chains resulting in an increased magnetic moment. The larger increase in the magnetic moment at 35 K is due to more Ni and Ir centers coupling along the chains. At low temperatures, these chains, which contain intra-chain ferromagnetic exchange, couple antiferromagnetically to give a zero effective moment. This phenomenon is depicted pictorially in Figure 4.11.

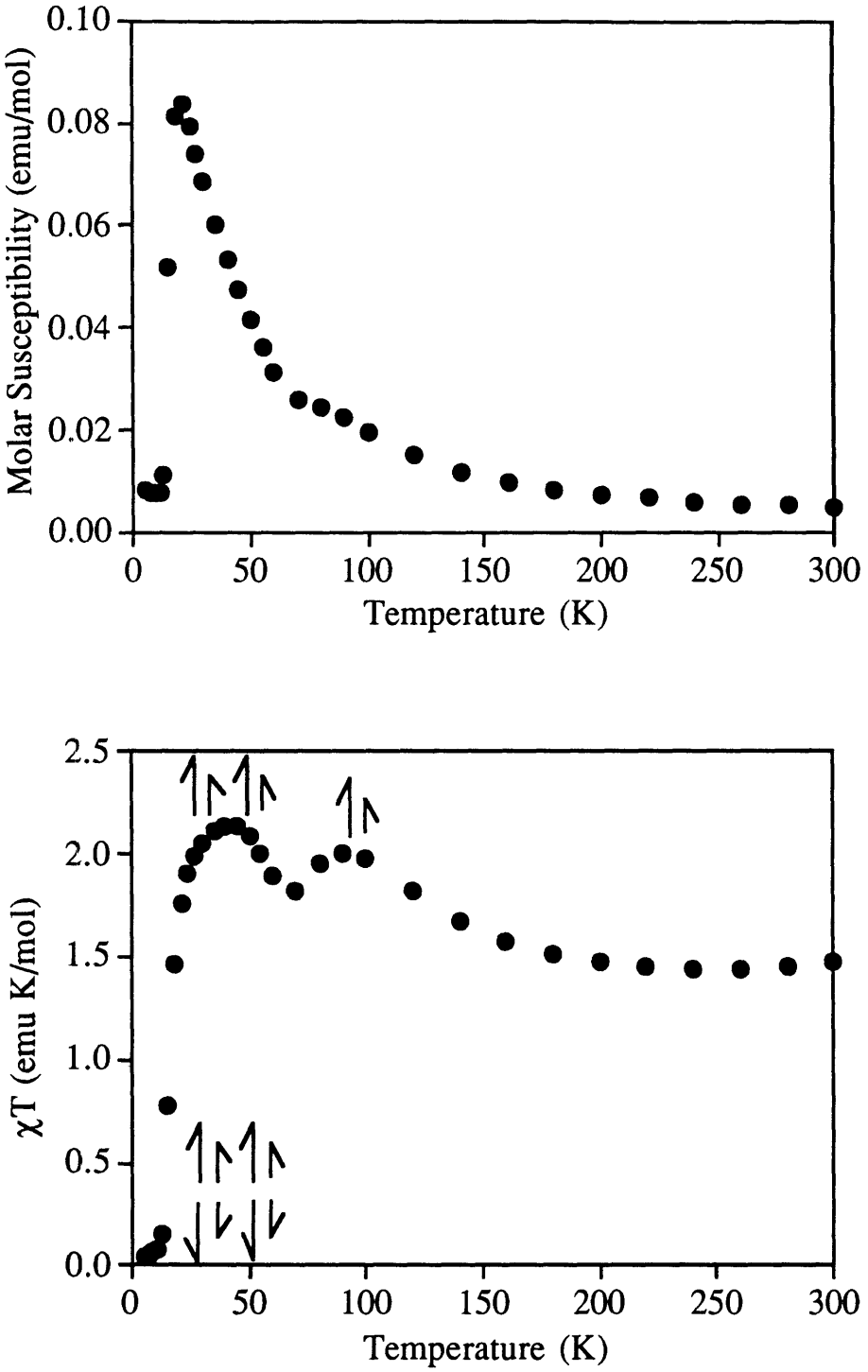

Figure 4.11. Top, magnetic susceptibility and, bottom, effective magnetic moment of Sr_3NiIrO_6 at 5kG.

Trends in the Magnetic Data:

The focus of this chapter has been the magnetic characterization of the one-dimensional oxides, Sr_3MIrO_6, where M = Zn, Cu, and Ni. Similar to the platinum-containing oxides described in Chapter 3, the ability of the structure to accommodate substitution on the trigonal prismatic M site allowed for the systematic study of the composition-magnetic property relationship in this series of materials. In the case of the iridium-containing oxides, however, the diamagnetic octahedral Pt(IV) site has been replaced by Ir(IV) which contains one unpaired electron.

As with the platinum-containing oxides, the magnetic behavior of the iridium-containing oxides became more complex as the number of unpaired electrons on the M site were increased from zero to one to two. Sr_3ZnIrO_6 displays antiferromagnetism, but the exact nature of this magnetic behavior is not fully understood. Sr_3ZnIrO_6 is a S = 1/2 system like Sr_3CuPtO_6, but since the site symmetry of the transition metal containing the unpaired electron is different, the magnetic behavior of the two compounds is not identical. The replacement of diamagnetic Zn(II) with Cu(II), which contains one unpaired electron, to form Sr_3CuIrO_6, creates a material that contains chains with two distinct S = 1/2 sites. These two sites order ferromagnetically, according to magnetic and electronic measurements. It is worthing pointing out that in these series of iridium-containing and platinum-containing oxides, Sr_3CuIrO_6 is the only material that contains only ferromagnetic coupling. This is of interest, especially since ferromagnetic order is rare in cuprates. In replacing Cu(II) with Ni(II) to give Sr_3NiIrO_6, a chain with alternating S = 1 and S = 1/2 centers is obtained. The magnetic behavior of this material is complex. From a plot of the effective moment, however, this material appears to couple ferromagnetically within the chains before undergoing interchain antiferromagnetic coupling to give a singlet ground state. It is interesting to compare the magnetic properties of Sr_3NiIrO_6 with that of Sr_3CoPtO_6 since both materials contain the largest number of unpaired electrons in their respective families; Sr_3NiIrO_6 is S = 3/2 and

Sr_3CoPtO_6 is S = 5/2. Both materials possess complex magnetic properties which contain ferromagnetic and antiferromagnetic interactions. Sr_3NiIrO_6 displays intrachain ferromagnetism and interchain antiferromagnetism, while Sr_3CoPtO_6 displays intrachain ferromagnetic and antiferromagnetic ordering. It seems that as a magnetic system becomes more classical, i.e., contains more unpaired electrons, the coexistence ferromagnetic and antiferromagnetic exchanges become favorable.

As with the platinum-containing oxides, the iridium-containing oxides' magnetic behavior can be altered by systematic substitutions. Furthermore, the addition of one unpaired electron to an otherwise diamagnetic site can have a significant effect on the magnetic properties of a material.

Conclusions:

The magnetic properties of three one-dimensional oxides, Sr_3ZnIrO_6, Sr_3CuIrO_6, and Sr_3NiIrO_6, were discussed in this chapter. These materials are the iridium analogs of the platinum oxides discussed in Chapter 3. The iridium-containing oxides offers a means of studying the effects on the magnetic properties in replacing a diamagnetic transition metal with one that contains an unpaired electron. As expected, this exchange results in magnetic behavior of increasing complexity. Sr_3ZnIrO_6 does not behave as an isotropic Heisenberg antiferromagnet like Sr_3CuPtO_6 even though they both have a spin 1/2 site alternating with a diamagnetic site. The specific site symmetry of the magnetic centers clearly has an important effect on the magnetic property. Sr_3CuIrO_6, in contrast to the antiferromagnetic Sr_3CuPtO_6, is a ferromagnet with a saturation magnetization that is not yet fully understood. Finally, the spin 3/2 system, Sr_3NiIrO_6, displays complex magnetism indicative of both intrachain ferromagnetism and interchain antiferromagnetism.

References

(1) Duffy, W. J.; Barr, K. P. *Phys. Rev.* **1968**, *165*, 647.

(2) Diederix, K. M.; Blote, H. W. J.; Groen, J. P.; Klaassen, T. O.; Poulis, N. J. *Phys. Rev. B* **1979**, *19*, 420.

(3) Bonner, J. C.; Friedberg, S. A.; Kobayashi, H.; Meier, D. L.; Blote, H. W. *Phys. Rev. B* **1983**, *27*, 248.

(4) Hall, J. W.; Marsh, W. E.; Weller, R. R.; Hatfield, W. E. *Inorg. Chem.* **1981**, *20*, 1033.

(5) Hatfield, W. E. *J. Appl. Phys.* **1981**, *52*, 1985.

(6) Neubacher, M.; Muller-Buschbaum, H. *Z. Anorg. Allg. Chem.* **1992**, *607*, 124.

(7) Tomaszewska, A.; Muller-Buschbaum, H. *Z. Anorg. Allg. Chem.* **1993**, *619*, 534.

(8) Carlin, R. L. *Magnetochemistry*; Springer-Verlag: Berlin, 1986.

Chapter 5

Designing A One-Dimensional Random Spin System:

Characterization of the Solid Solution $Sr_3CuPt_{1-x}Ir_xO_6$ ($0 \leq x \leq 1$)

Chapter 5

One of the ultimate goals of solid state chemistry is the rational design of materials with predictable properties. The work described in Chapters 3 and 4 has provided us with a database (Table 5.1) of magnetic properties as a function of composition in a well-defined system. With these known property-composition relationships, it should be possible to tailor the magnetic properties by creating specific solid solutions that exhibit specific, predictable magnetic behavior.

Table 5.1. Summary of the Magnetic Behavior of the $Sr_3MM'O_6$ System, M = Zn, Cu, Ni, Co; M' = Pt, Ir

$Sr_3MM'O_6$	Spin of M	Spin of M'	Magnetic Behavior
Sr_3ZnPtO_6	S = 0	S = 0	Diamagnetic
Sr_3CuPtO_6	S = 1/2	S = 0	Antiferromagnetism
Sr_3NiPtO_6	S = 1	S = 0	Antiferromagnetism
Sr_3CoPtO_6	S = 2	$\overline{S}$ = 1/2	Random spin paramagnetism
Sr_3ZnIrO_6	S = 0	S = 1/2	Antiferromagnetism
Sr_3CuIrO_6	S = 1/2	S = 1/2	Ferromagnetism
Sr_3NiIrO_6	S = 1	S = 1/2	Complex ferromagnetism and antiferromagnetism

This chapter discusses our efforts to prepare a one-dimensional compound exhibiting random spin paramagnetism. The material Sr_3CoPtO_6, as discussed in Chapter 3, is the first material ever to exhibit random spin paramagnetism. The discovery of the magnetic properties of this material lead to the development by Lee, et. al of the random quantum spin-1/2 chain model, which explains the magnetic and heat capacity behavior of a one-dimensional material containing random ferromagnetic *and* antiferromagnetic coupling within the chains. Basically, a random quantum spin magnet is similar to an

antiferromagnet, however, the antiparallel exchange is now between ferromagnetic islands clustered along the chains. The theoretical inverse susceptibility behavior of materials with varying ratios of ferromagnetic and antiferromagnetic coupling within the chains is shown in Figure 5.1. P is the probability distribution of having a certain interaction. The limit $p = 0$ corresponds to a uniform antiferromagnet, and $p = 1$ corresponds to a uniform Heisenberg ferromagnet. A material containing chains with intermediate probability of ferromagnetic and antiferromagnetic interactions, i.e., $0 < p < 1$, is predicted to exhibit two distinct regions in the magnetic susceptibility. At high temperatures, the spins act independently and the magnetic susceptibility is Curie-like. At lower temperatures, there is a transition during which the spins gradually become correlated. As the temperature is decreased and more spins align, the correlation lengths increase to form ferromagnetic "islands" which act as domains of one large spin. For example, in a case of a nearly ferromagnetic chain with a few antiferromagnetic interactions, i.e., $p \approx 1$, the islands are separated from one another by antiferromagnetic interactions which lock the adjacent neighbors into a singlet dimer and decouple the ferromagnetic islands from each other. At low temperatures, these islands are able to overcome the antiferromagnetic barriers and couple to give an averaged total singlet ground state. Similar to the susceptibility behavior, the heat capacity behavior is predicted to contain two features. At low temperature, there is a transition due to the initial coupling among the spins; the transition temperature is a measure of the exchange constant, the J-value. Upon lowering the temperature further, there is a second transition due to the coupling of the ferromagnetic islands, similar to what is observed in the magnetic susceptibility measurements. Thus, the random quantum spin-1/2 chain model provides two means, susceptibility and heat capacity measurements, by which to identify a random spin paramagnet.

Since the random spin material must contain both ferromagnetic and antiferromagnetic interactions, the strategy for synthesizing a model compound was to

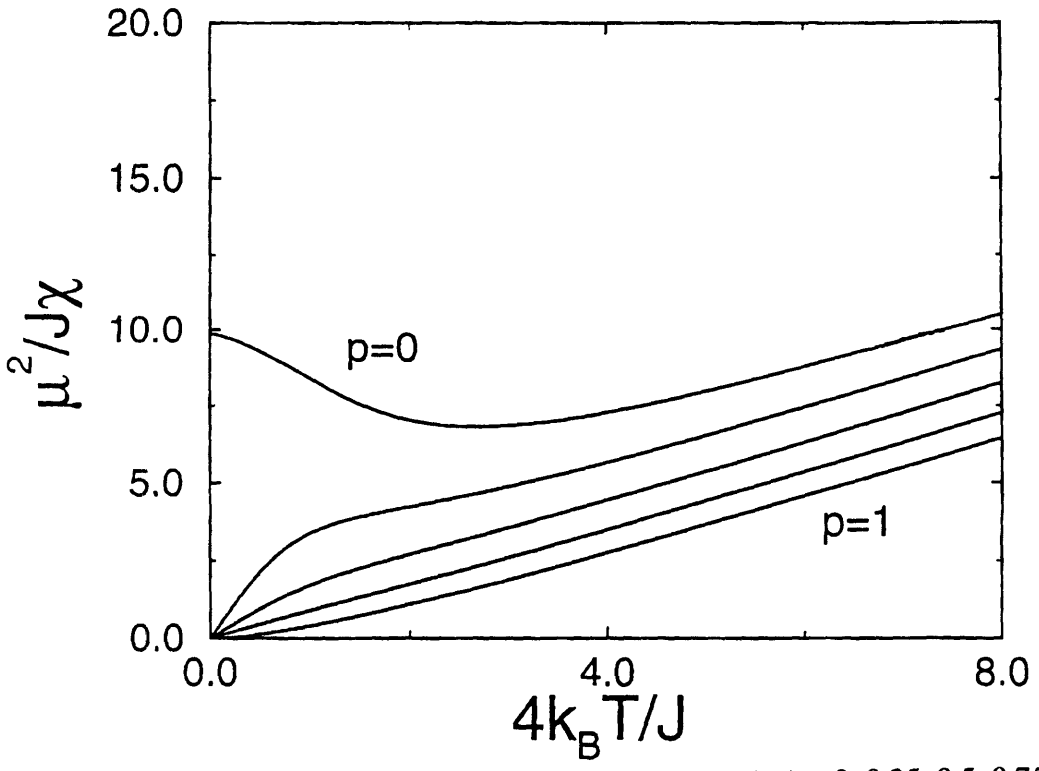

Figure 5.1. Theoretical inverse susceptibility for p (or 1-x) = 0, 0.25, 0.5, 0.75, and 1 for the quantum spin chain, as predicted by Lee, et. al.

prepare a solid solution of a ferromagnet and an antiferromagnet. From the studies described in the previous chapters, it was known that two closely-related materials match these criteria, namely, the antiferromagnet, Sr_3CuPtO_6, and the ferromagnet, Sr_3CuIrO_6. By reacting these two end members in a range of stoichiometries to produce the solid solution $Sr_3CuPt_{1-x}Ir_xO_6$, we were able to prepare controllably materials which contain two types of interactions and a range of average exchange values. $Sr_3CuPt_{1-x}Ir_xO_6$ also represents a better model compound for random spin paramagnetism than Sr_3CoPtO_6. The cobalt-containing oxide has a spin of 5/2 and, therefore, its magnetic behavior approaches that of a classical system. $Sr_3CuPt_{1-x}Ir_xO_6$, on the other hand, has a spin of 1/2 to 1 which makes it a better example of a quantum system, the type of system explained by Lee's model.

Results and Discussion:

The solid solution $Sr_3CuPt_xIr_{1-x}O_6$ ($0 < x < 1$) was prepared by solid state synthesis and characterized both structurally and magnetically. Powder X-ray diffraction studies of members of this solid solution revealed diffraction patterns identical to those of the two end compounds. Figure 5.2 shows the inverse susceptibilities for several compositions of this solid solution. The inverse susceptibility behavior of $Sr_3CuPt_{1-x}Ir_xO_6$ agrees very well with the theoretical predictios of Lee's model. In substituting Ir into the uniformly antiferromagnetic compound Sr_3CuPtO_6, we can controllably introduce ferromagnetic interactions into the chains. For example, $Sr_3CuPt_{0.75}Ir_{0.25}O_6$, which possesses only a small amount of iridium, contains small ferromagnetic islands separated by antiferromagnetic interactions, while $Sr_3CuPt_{0.25}Ir_{0.75}O_6$, which possesses a greater amount of iridium, contains large ferromagnetic islands separated by antiferromagnetic interactions. The magnetic behavior of this system follows a systematic trend as a function of Pt/Ir ratio, which

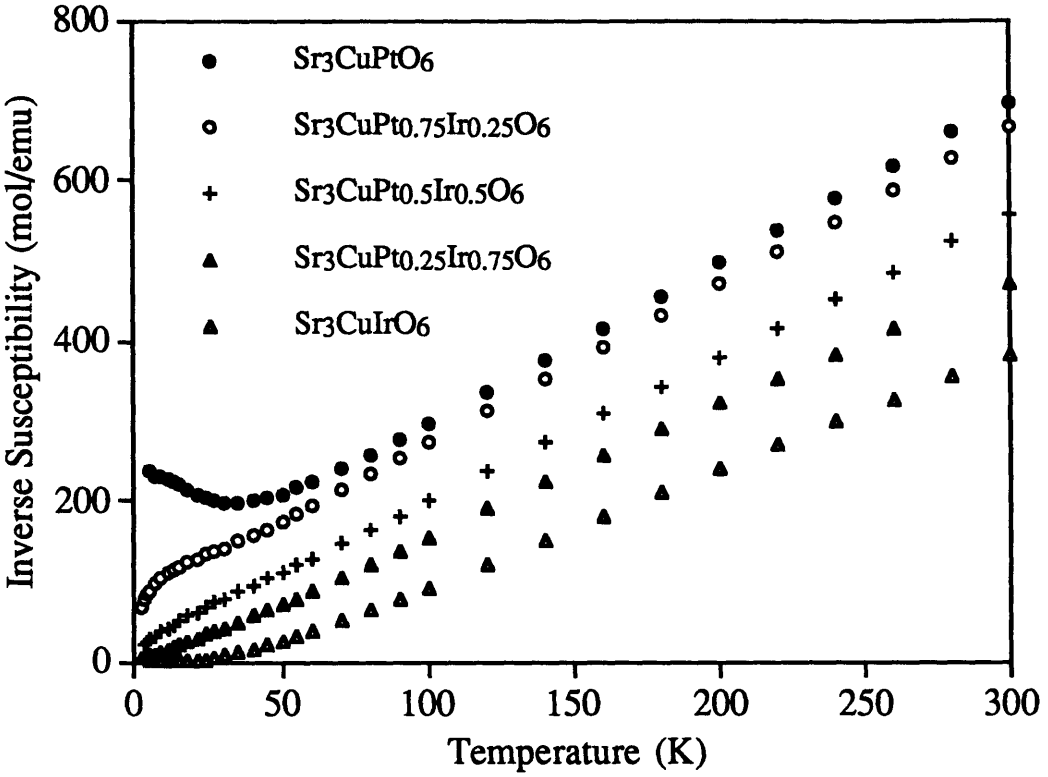

Figure 5.2. Inverse susceptibilities for several compositions in the $Sr_3CuPt_xIr_{1-x}O_6$ solid solution showing the well-behaved trend of Weiss constant as a function of Pt/Ir ratio.

makes it possible to control accurately the high temperature Weiss constant from an antiferromagnetic value of θ = -46.6 K (Sr_3CuPtO_6) to a ferromagnetic value of θ = +36.2 K (Sr_3CuIrO_6). (Figure 5.3)

The system of greatest interest, however, is $Sr_3CuPt_{0.5}Ir_{0.5}O_6$, which contains randomly distributed Pt and Ir sites, i.e., random magnetic interactions, and which has equal ferromagnetic and antiferromagnetic contributions. The inverse susceptibility of $Sr_3CuPt_{0.5}Ir_{0.5}O_6$ follows the predicted behavior of a random quantum spin chain. At high temperatures, the susceptibility has a linear χ versus 1/T dependence and is Curie-like. In this regime, where there is no coupling among unpaired electrons, the spins act independently. A fit of the high-temperature data gave a Weiss constant of θ = -12.7 K and a spin-only moment of μ_B = 2.11, a value that falls between the moment of one unpaired electron (1.73 μ_B) and two unpaired electrons (2.83 μ_B). At lower temperatures, there is a transition to spin-spin interactions indicated by the broad curve in the inverse susceptibility. This transition marks the alignment of spins to form ferromagnetic islands. It is a broad transition because the ferromagnetic islands have a range of sizes, i.e., there exist different size correlation lengths in the material. The correlation lengths depend on how often and how randomly the islands are interrupted by antiferromagnetic segments. Islands of different lengths require different temperatures to order, resulting in a broad transition. Figure 5.4 shows the effective moment of $Sr_3CuPt_{0.5}Ir_{0.5}O_6$ as a function of temperature. As expected for a random spin magnet, the moment decreases at low temperatures, indicating antiferromagnetic ordering. The heat capactity of $Sr_3CuPt_{0.5}Ir_{0.5}O_6$ from 4 to 50 K is shown in Figure 5.5. $Sr_3CuPt_{0.5}Ir_{0.5}O_6$ exhibits heat capacity behavior similar to that of Sr_3CoPtO_6, but at lower temperatures, ~20 K, the heat capactity of $Sr_3CuPt_{0.5}Ir_{0.5}O_6$ increases, suggesting a rise in entropy, which may signal the expected ordering transition that corresponds to the coupling of ferromagnetic islands. Consequently, both the susceptibility and the heat

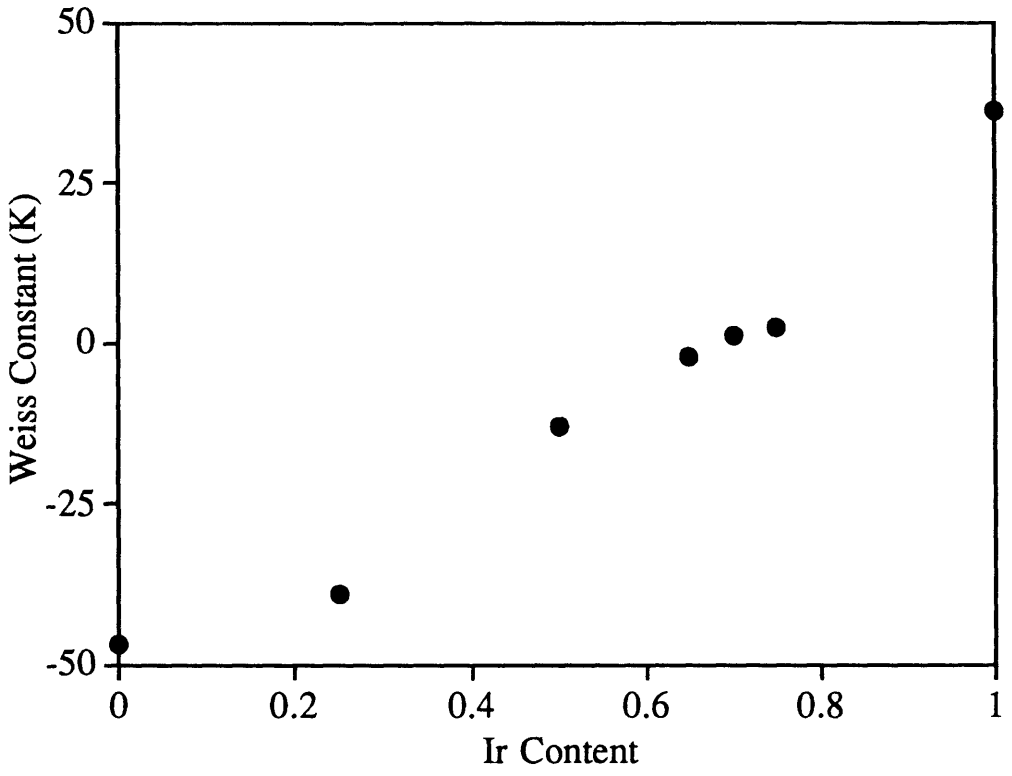

Figure 5.3. Weiss constant as a function of Ir content in the $Sr_3CuPt_xIr_{1-x}O_6$ solid solution.

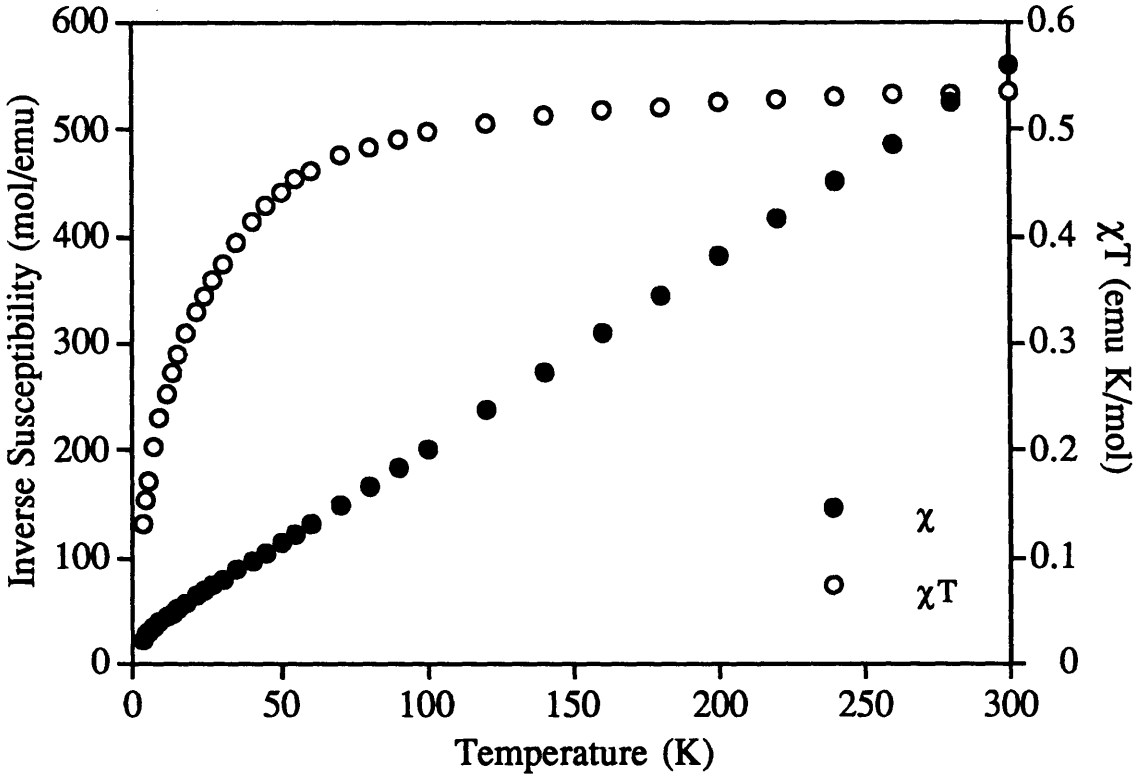

Figure 5.4. χ and χT plots for $Sr_3CuPt_{0.5}Ir_{0.5}O_6$. The downward turn in the effective moment indicates antiferromagnetic coupling.

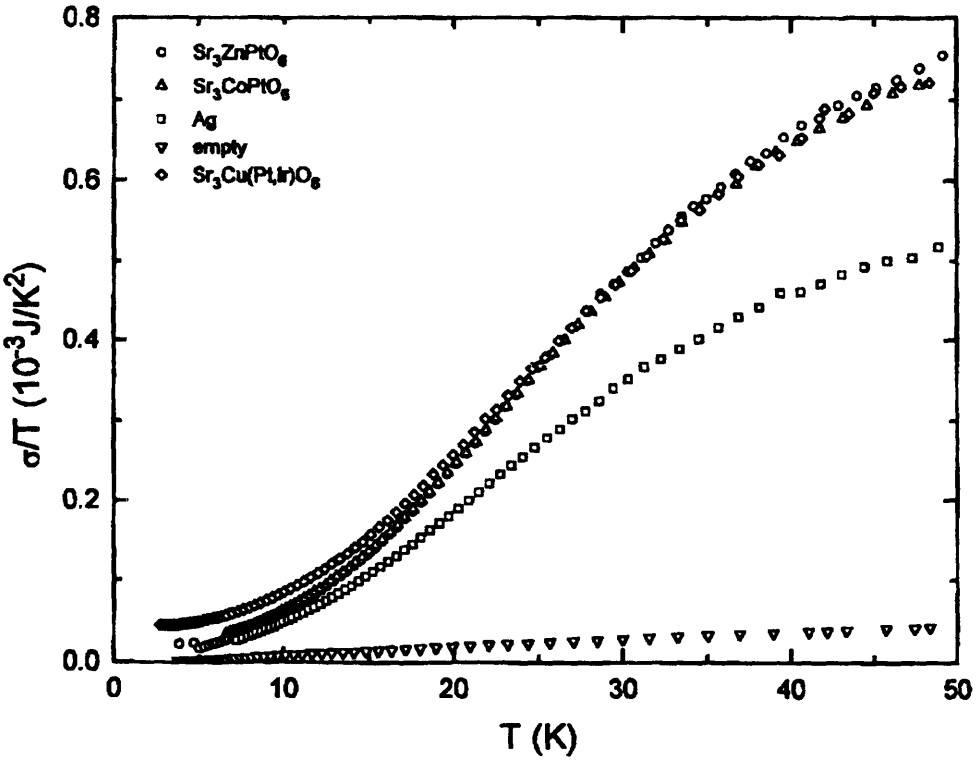

Figure 5.5. Heat capacity of $Sr_3CuPt_{0.5}Ir_{0.5}O_6$ showing similar behavior to Sr_3CoPtO_6.

capacity data indicate that this material exhibits random spin paramagnetism. The attempt to produce a random spin paramagnet by design was successful.

Conclusions:

The rational design of a new random spin paramagnet has been achieved by creating the solid solution $Sr_3CuPt_xIr_{1-x}O_6$. One composition in particular, $Sr_3CuPt_{0.5}Ir_{0.5}O_6$, shows the expected magnetic and heat capacity characteristics of random spin paramagnetism. Low temperature heat capacity measurements are in progress to establish the temperature at which the antiferromagnetic coupling of ferromagnetic islands takes place.